A Correction to the Modelled Jet Energy Resolution of the ATLAS Detector

by

Brock Moir

B.Sc., University of Alberta, 2009

A Thesis Submitted in Partial Fulfillment of the

Requirements for the Degree of

Master of Science

in the Department of Physics and Astronomy

A Correction to the Modelled Jet Energy Resolution of the ATLAS Detector

by

Brock Moir

B.Sc., University of Alberta, 2009

Supervisory Committee

Dr. R. Keeler, Supervisor

(Department of Physics and Astronomy)

Dr. A. Ritz, Departmental Member

(Department of Physics and Astronomy)

Dr. R. McPherson, Departmental Member

(Department of Physics and Astronomy)

Supervisory Committee

Dr. R. Keeler, Supervisor
(Department of Physics and Astronomy)

Dr. A. Ritz, Departmental Member
(Department of Physics and Astronomy)

Dr. R. McPherson, Departmental Member
(Department of Physics and Astronomy)

ABSTRACT

Using a measure of the jet energy resolution that relies on momentum balance in direct photon events, a correction to the modelled detector resolution is developed. The correction is produced by iteratively unfolding the model from the measured data. Jets in the model are then smeared using this correction, and the result is compared to the data using a χ^2 test. This method is shown to be effective at improving the agreement between the data and the model, even when the model initially shows poor agreement to the data.

Contents

List of Tables

List of Figures

ACKNOWLEDGEMENTS

Foremost, I would like to thank my supervisor Dr. Richard Keeler for pushing me through to the end, and assisting immensely in reviewing and editing this document. Thank you to my committee members Dr. Rob McPherson, Dr. Adam Ritz, and Dr. Ken Ragan for taking the time to read this document, and agreeing to examine me.

This thesis would not have been possible without the work done by the ATLAS collaboration, and the LHC accelerator run by CERN. Nor would it have been possible without the path paved by Dr. Lorriane Courneyea.

A special thanks Tony and Alison for countless Settlers breaks and perhaps too many Dark Matters.

DEDICATION

I dedicate this work to my daughter Iyla Mae Moir, my life will forever be enriched by your presence.

Chapter 1

Introduction

The Large Hadron Collider (LHC) at the European Organization for Nuclear Research (CERN) is one of mankind's largest scientific experiments. The energy at which the LHC collides protons allows for the exploration of a new energy frontier and the rate at which these collisions occur enables physicists to make precision measurements of the prevailing theory of subatomic physics, the Standard Model. Physicists working for the various LHC collaborations are stretching the boundaries of our knowledge, and testing likely candidates for theories that extend beyond the Standard Model.

For the ATLAS collaboration, and any particle physics experiment, making precision measurements requires having accurate simulations of the collisions that occur within it. These simulations are produced using Monte Carlo methods, and are known as Monte Carlo (MC) simulations. Not only must the MC sample statistically represent the Standard Model but the geometry and response of the detector to the particles must be accurately reproduced, such that measurement and model may be treated on an equal basis in an analysis. Accuracy follows from having a solid theoretical understanding of the physics involved. The theoretical model in use is known as the Standard Model. Accurately simulating the detector is not something that

is straight forward. There are many reasons why the detector can be insufficiently modelled, especially in a detector as complicated and with as many components as the ATLAS detector.

Due to the intense computational nature of producing MC events for the ATLAS detector, it is not always practical to correct the model directly should there be an error and then redo the simulation. Instead, it is often more practical for a correction to be applied after the simulation is complete. This body of work aims at developing a technique to make one such correction that focuses on the simulated detector response to the jet energy.

The objective of this thesis is to produce a correction to the simulated jet energy in order to improve the agreement between the experimental data and the MC simulation. There are a number of reasons why the MC jet energy resolution is not always an accurate representation of the data. Insufficient accuracy in the detector modelling or changes in the physical detector's operating condition would produce a deviation but there could be other reasons. The correction that is produced in this body of work is produced by unfolding the MC from the data, a method that was used by Dr. Lorraine Courneyea in her PhD thesis [1]. The method of unfolding is unique to this body of work, as well as the closure test used to check the validity of this method.

A significant amount of background information is required in order to properly present and understand this technique's successes and failures. The next couple of chapters are designed to provide the reader with sufficient background to understand the physics of proton proton collisions. Chapter two focuses on the theoretical foundations for this work. It includes: a brief discussion on the Standard Model; an explanation of the types of collisions that are important to this work; a description of the variable that is used to define the jet energy response; and how this variable is

compared in the data and MC using the technique of unfolding. Chapter three is a discussion of how the high energy particles in this analysis (jets and photons) interact with matter and how these interactions are used to measure these particles.

Following these chapters outlining the physics involved, chapters four and five are included to give the reader an overview of the experimental techniques employed by the LHC and the ATLAS collaborations. First, chapter four provides an overview of the experimental parameters of the LHC and ATLAS. Chapter five then goes into detail about the computational methods that are used to handle the large data sets that are produced by measuring the proton proton collisions with the ATLAS detector.

The research carried out for this thesis is explained and summarized in the chapters six and seven. The method by which this research has been carried out is explained in chapter six. This starts with a description of the event selection. The chapter goes into detail on the production of the MC correction and how this correction is tested, including the choice of the kinematic regions that are chosen to separate this correction into. Chapter seven presents the results of this research. Here one will find an analysis on the effectiveness of this method.

Chapter 8 summarizes the conclusions drawn from this work. Appendices are included to provide supporting information for some of the concepts and techniques used in this thesis as well as additional plots that have been included for completeness.

Chapter 2

Theory

This chapter reviews the theoretical tools that are used in this analysis. It begins with a discussion of the Standard Model of particle physics, a theory of the interactions occurring in particle collisions. Related to the Standard Model is the physics of the proton-proton collisions happening within the LHC detectors. Later in this chapter, the creation of direct photon events is discussed, as well as their application to estimating the jet energy response. The final sections explain how to smear and unfold the observed data in order to estimate the underlying physical results.

2.1 The Standard Model

The Standard Model (SM) of particle physics is the current prevailing theory describing the fundamental subatomic particles and their interactions. This theory predicted the existence of the W and Z bosons, gluons, and the top and the charm quarks all before they were measured. More recently the predicted Higgs Boson has also been discovered independently by the ATLAS and CMS collaborations[2, 3].

Particles in the Standard Model are postulated to be invariant under Lorentz transformations. Invariant representations of the Lorentz group can transform as a

scalar, a spinor, or a vector; in terms of spin statistics, respectively these are spinless particles (a spin zero boson), half integer spin fermions, or integer spin bosons. All of the fundamental particles are fermions, and all of the force carriers are bosons[4].

In order for fields to be locally invariant under certain symmetry groups, they interact with gauge bosons. Each gauge boson represents an independent element of the algebra that describes the relevant symmetry group. The electro-weak gauge bosons (the $W^{\pm}$, Z, and photon) come from the four elements of the su(2)xu(1) algebra. The eight gluons from the strong interaction correspond to the eight linearly independent elements that transform under the adjoint representation of the su(3) algebra. The group of fermions that transform as a three dimensional vector in the SU(3) representation are the quarks. Fermions that do not transform under this representation are the leptons[5]. A depiction of the generations and flavours of the standard model, as well as the forces is given in Figure 2.1.

The above would be a complete description if all of the gauge bosons were massless, but not all of them are. In order to account for the mass of the W and the Z, the Higgs mechanism is used. The SU(2)xU(1) symmetry is broken spontaneously by introducing a potential that is not symmetric under SU(2)xU(1). Giving mass to the $W^{\pm}$ and Z has a trade off; it requires the existence of a new scalar field, the Higgs boson. The Higgs field also interacts with the fermions in such a way as to introduce a mass term in the Standard Model lagrangian.

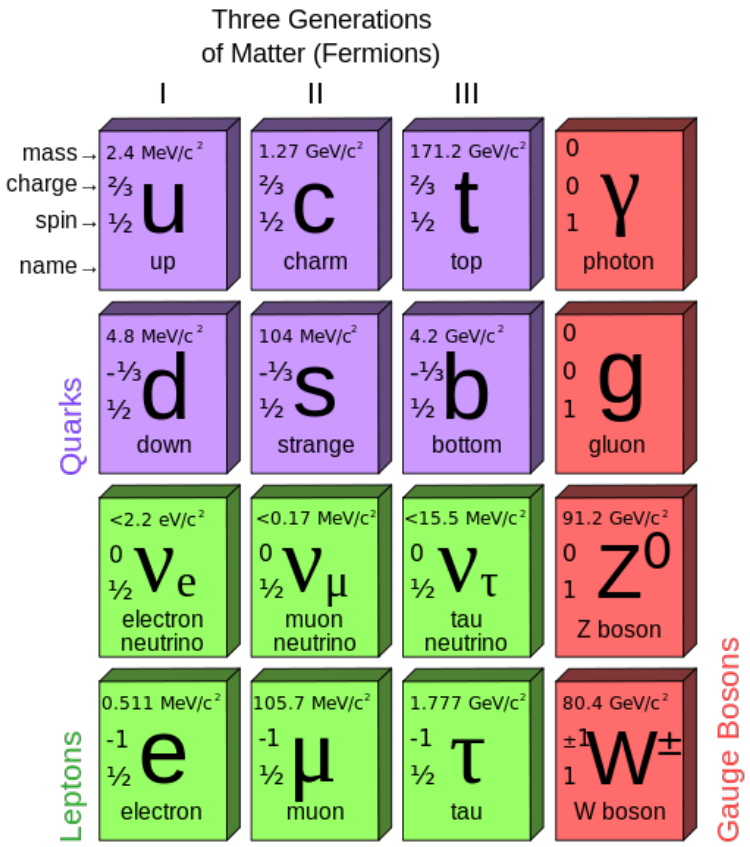

Figure 2.1: The fermions and bosons included within the Standard Model[2]. Fermions include the three generations of leptons and the three generations of quarks. The bosons are the twelve force carriers (photon, eight gluons, Z, and the two Ws). Not present in this image is the recently confirmed Higgs boson.

2.1.1 Quantum Electrodynamics (QED)

Quantum Electrodynamics (QED) is the relativistic quantum field theory that describes interactions between photons (spin one bosons) and electromagnetically charged fermions. It is a gauge theory with a U(1) symmetry.

[2]http://cms.web.cern.ch/news/what-do-we-already-know

A powerful tool used to describe and calculate interactions in the Standard Model is the use of Feynman diagrams. In Feynman diagrams fermions are represented by solid lines; gluons by curly lines; and the photon, W, and Z are represented by wavy lines. The vertexes that are allowed in a Feynman diagram are precisely those interactions that are present in the Standard Model[5, 4].

QED provides a simple example of how Feynman diagrams are used. In QED only the interaction vertex shown in Figure 2.2 is allowed. That one vertex is sufficient to account for all electromagnetic interactions.

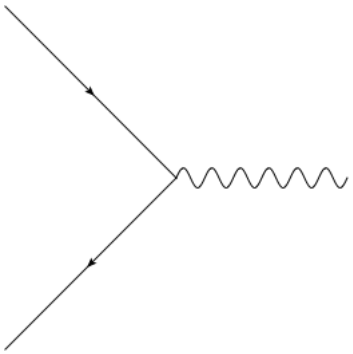

Figure 2.2: The primary vertex for QED. The wavy line represents the photon, and the straight lines represent any charged fermion.

2.1.2 Quantum Chromodynamics (QCD)

QCD is the relativistic quantum field theory describing the interactions between quarks and gluons. It is a gauge theory with an SU(3) symmetry. This theory is much more complicated than QED because gluons can interact with themselves, allowing for the vertices shown in figure 2.3.

QCD charge is called colour-hence the name Quantum Chromodynamics. There are three types of colour charge each with its own anti-colour. Gluons carry a colour neutral combination of colour and anti-colour-they are massless and there are 8 of

them. Quarks are always colour charged-they have mass and for some reason they come in three generations of weak isospin doublets. So far, we know of six quarks each with its own anti-quark.

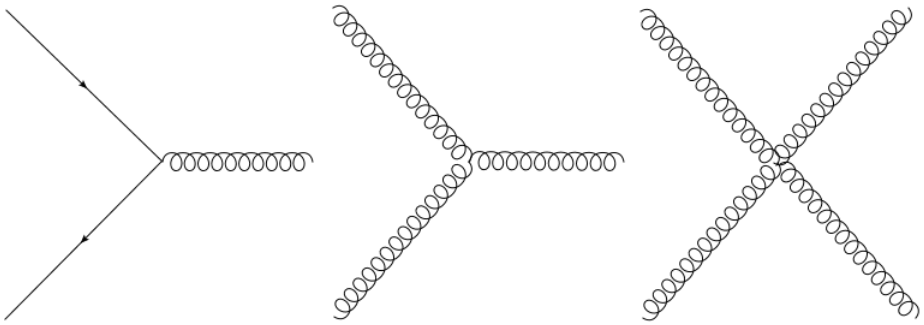

Figure 2.3: The three primary vertices for QCD. The curly lines represent the gluons and the straight lines represent quarks.

One implication of QCD is that there can be no free colour charge, this is known as quark confinement. Quarks and gluons that are produced in high energy particle collisions can not exist by themselves. When a quark or gluon is produced, it will spontaneously produce quarks out of the vacuum to create hadrons in colour singlets. Hadrons are composite particles, either consisting of a quark and an anti-quark (mesons) or three quarks (baryons). Therefore, a high energy single quark or gluon will create a narrow cone of hadrons called a jet. The process by which this occurs is known as hadronization. Jets must be simulated using Monte Carlo methods as it is not yet possible to calculate their properties analytically.

2.2 Proton-Proton Collisions

In high energy proton-proton collisions, such as those at the LHC, it is not actually the protons that are colliding. It is their constituents, known as partons, that take part in the collision. The tidy model of a proton being composed of two up quarks

and a down quark is not sufficient for such high energy collisions because of the implications of QCD. In collisions with high energy transfer, virtual quarks and gluons may also take part in the interaction. The initial state of collisions at the LHC is given by a probability density of what could interact. The measurement of the Parton Distribution Functions (PDFs) is a major topic in itself. The PDFs depend on the momentum transferred (Q^2) as well as the fraction of the proton's momentum carried by the parton (x). Fig 2.4[6] shows a fit to measurements of the PDF.

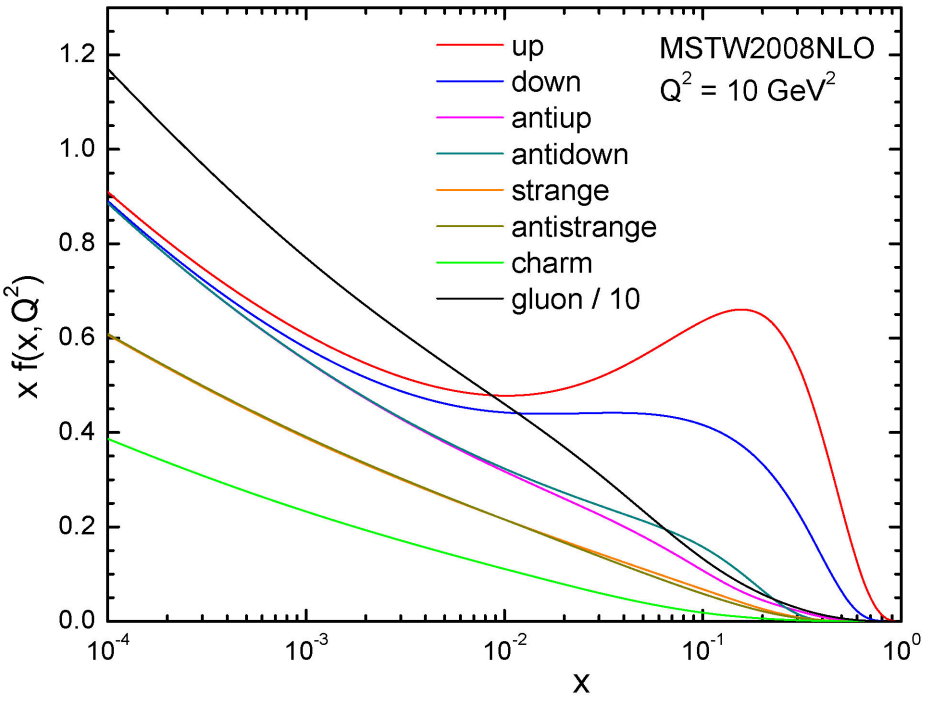

Figure 2.4: Measurement of the Parton Distribution Function for $Q^2 = 10GeV^2$[6]

The coupling constant for QCD depends on the momentum transfer in the QCD scattering process. Because of this, there are two very different regimes of QCD scattering. Hard scattering events involve high momentum transfer. These scattering events are fairly well understood using perturbative methods. On the other hand,

soft scattering events involve low momentum transfers. Since the QCD coupling is strong in soft scatters, it is very difficult to describe these events. The problem in understanding these events is that having a strong coupling makes it possible for many more interactions to dominate the process, as such perturbative methods do not converge and other techniques are needed to understand these interactions.

2.3 Direct Photon Events

In order to estimate the jet energy resolution, this thesis relies on finding events with a jet energetically balanced with a photon. Such events are called direct photon events; the section below describes how they can be produced by collisions at the ATLAS detector.

The initial state of any collision in ATLAS is between partons, either gluons or quarks. There are a number of ways these partons can interact to create direct photon events. Regardless of the interaction the final state should contain a photon and either a quark or a gluon. The quark or gluon in the final state will hadronize eventually leading to a jet of energetic particles. Hence, a direct photon event is one with a photon and a jet energetically balanced in the final state [7] [8].

There are 3 unique leading order processes that can create a direct photon event shown in fig 2.5. Two of these involve compton scattering where a quark interacts with a massless gluon, and the other is the result of quark anti-quark annihilation.

The next-to-leading order processes that produce the same final state particles can be found by connecting any two of the partons from the LO processes with a gluon. Other next to leading order processes typically result in a direct photon with a dijet final state. Events where a charged quark radiates a photon could produce a similar signature. In this case the photon is usually produced at a low energy colinear

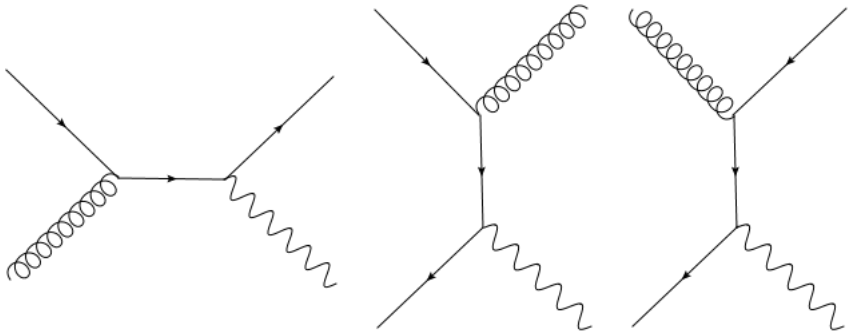

Figure 2.5: Leading order direct photon Feynman diagrams. In these Feynman diagrams time flows to the right. The first and last diagram describe compton scattering while the middle diagram describes quark anti-quark annihilation. The initial states all contain partons, while the final states must contain a photon and a parton.

with a hadronic jet; although there is a small probabilty that the photon can carry away most of the quark's energy and this would result in an isolated photon in the event [9].

2.4 Estimating Jet Response

In ATLAS there are a number of techniques used to estimate the energy resolution of jets[10]. These techniques typically rely on momentum conservation and jet balancing. For this thesis, the jet energy resolution is estimated by finding jets that are energetically balanced with photons. How this method works is described below.

Before a collision in the LHC, the protons carry all of the momentum down the beam pipe. The partons that interact do so with an unspecified fraction of the proton's momentum, x; therefore, it is impossible to know the total initial momentum in the direction parallel to the beam pipe. The direction perpendicular to the beam pipe (the transverse plane) on the other hand is more well defined. Before the collision, the net transverse momentum carried by the protons is zero. Since momentum must be conserved before and after the collision, the transverse momenta of all the final

state particles must sum to zero. While it is not always possible to measure the momentum of all of the particles resulting from a collision, the following relation is still approximately valid:

$$\Sigma \vec{P_T} = 0. \tag{2.1}$$

In events dominated by direct photon production, the objects may not be energetically balanced in the lab frame because of the unbalanced initial longitudinal momentum. However, in the transverse plane the jet and the photon should approximately be balanced since the initial transverse momentum is approximately zero. Using equation (2.1),

$$\vec{P_T^{\gamma}} + \vec{P_T^{jet}} = 0. \tag{2.2}$$

Any deviation from (2.2) must be the result of mis-measuring the energies of these objects; either because of the finite energy resolution, or the objects are traversing regions where their energy can not be measured properly. One can account for these crack regions by excluding objects that travel through them. The remaining discrepancy is accounted for by the energy resolution of the jet and the photon. As will be discussed later, in ATLAS electromagnetic objects such as photons have an energy resolution that is almost an order of magnitude better than the energy resolution of hadronic jets. Therefore deviations from (2.2) are mostly the result of the energy resolution of jets in the ATLAS detector.

A variable that corresponds to the estimated jet energy resolution can be constructed. The variable Z defined below is a measure of the deviation from (2.2),

$$Z = \frac{P_T^{jet}}{P_T^{\gamma}} - 1. \tag{2.3}$$

Ideally Z represents the jet energy resolution for direct photon events, and its accuracy is assumed to be dependent on the energy resolution of the photons. Since the jet energy resolution is smeared out, Z should be some distribution approximately centered around zero. The appendix A.2 contains a general description of smearing.

If the detector was modelled perfectly, a measurement of the distribution of Z should be the same in the data and in our simulations. However, the way we simulate particles traversing the detector is not always perfect. The difference between a measurement of an instance of Z in our data, Z_{data}, and an instance of Z from our simulations, Z_{MC} is due to an unaccounted for detector response, R. The probability distribution functions for Z in the data, $f_{data}(Z_{data})$, and in the simulation, $f_{MC}(Z_{MC})$, can be related by a convolution[11, 12].

$$f_{data}(Z_{data}) = R(Z_{data}|Z_{MC}) * f_{MC}(Z_{MC}) \tag{2.4}$$

If the measured distributions were continuous the convolution would be an integral. For binned histograms it can be represented as a sum.

$$f^i_{data} = \sum_{j=1}^{N_{bins}} R^{ij} f^j_{MC} \tag{2.5}$$

Where $R^{ij} = P(\text{data in bin i} \mid \text{simulation in bin j})$ is the matrix that describes the unaccounted for detector response. Later this will be referred to as the smearing function.

2.5 Unfolding

In equation (2.4) there are three components: the data distribution function, the simulation distribution function, and the smearing function. In practice, it is possible

to measure the data distribution and produce the simulation distribution. However, the smearing function must be found using an unfolding method which is described in more detail in the appendix section A.2.

In ATLAS, unfolding has traditionally been done using the method of bin by bin correction factors[13, 12]. More recently the iterative method of unfolding developed by D'Agostini[14] is gaining use. The second method will be used for this body of work. An explaination of this method is available in the appendix section A.3.

Chapter 3

Interaction of Particles with Matter

When proton-proton interactions create a photon and a hadronic jet, the energy and identification of these objects is accomplished using large purpose-built calorimeters. This chapter describes first how particles interact with matter, and then how this knowledge can be used in order to determine the type and energy of the particles.

3.1 Photons: Electromagnetic interactions with matter

A high energy (> 100 MeV) photon interacts with matter mainly by electron-positron pair production either from the electric field of the electrons or the nuclei of the medium through which it is traveling [15]. Figure 3.1 shows the probability that a high energy photon will undergo pair production in a material.

High energy (> 100 MeV) electrons and positrons lose most of their energy in matter by emitting bremsstrahlung radiation [15]. Bremsstrahlung radiation photons will pair produce more electrons and positrons, which will then radiate more. This process is known as an electromagnetic shower. This cycle will continue until the

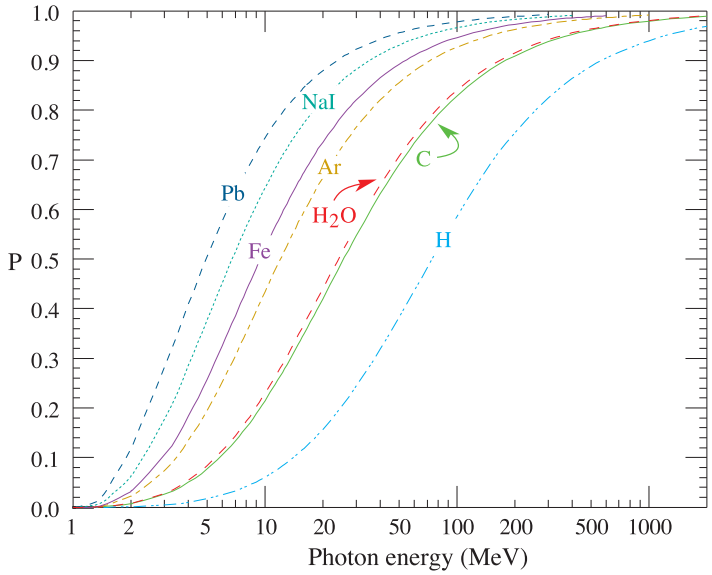

Figure 3.1: Probability, P, that a high energy photon will result in pair production in various materials.[15]

photons have a small enough energy for Compton scattering interactions to become dominant, and the electrons have a small enough energy for ionization interactions (see figure 3.2) to become significant. In both of these cases, new particles are no longer being created and the shower process will stop. This happens at the energy at which electrons lose as much energy from ionization as to bremsstrahlung and is known as the critical energy, E_c. Figure 3.2 shows the electron energy loss mechanisms in lead. An important electromagnetic shower characteristic is the radiation length, X_o, which is the length a high energy electron will travel before losing all but 1/e of its energy, or about 7/9 of the mean free path for pair production by a high energy photon. Both the critical energy and the radiation length are properties of the material through which the electromagnetic shower is traversing.

The depth through the material, X, that the shower will penetrate is related to these quantities and the initial energy of the electromagnetic particle, E_o, by the expression in equation (3.1).

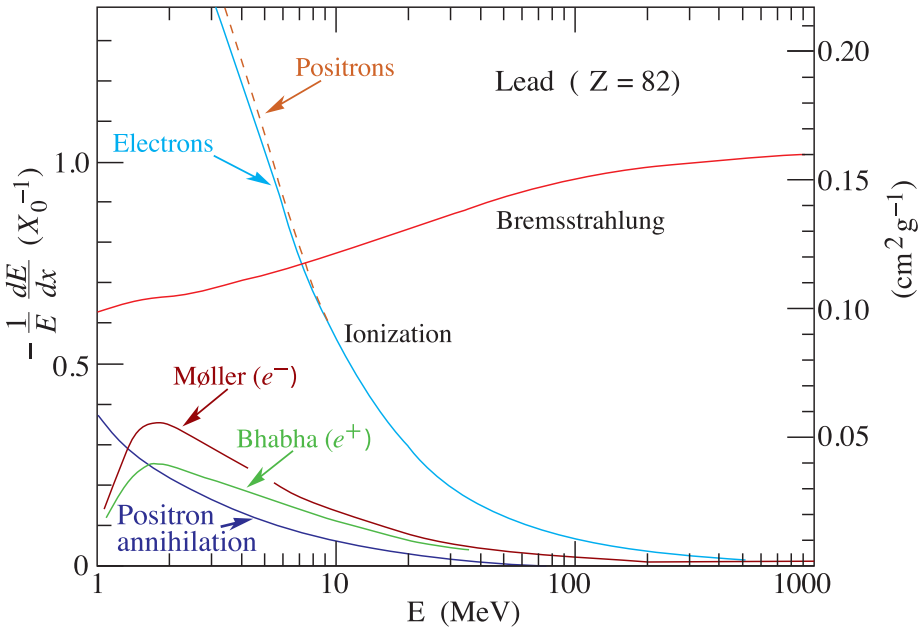

Figure 3.2: Dominant electron energy loss mechanisms at various energies in lead.[15]

$$X = X_o \frac{ln(\frac{E_o}{E_c})}{ln2} \tag{3.1}$$

In the transverse direction, the shower spreads mostly through multiple scattering and from the production angle between the electron positron pairs. The radius of the cylinder that contains about 95% of the shower is known as the Moliere radius. It is proportional to the radiation length and inversely proportional to the critical energy of the material through which the shower is progressing.

3.2 Hadrons: Hadronic jet interactions with matter

As was discussed earlier in the previous chapter, the phenomenon of QCD requires the production of a quark or a gluon to be followed by a process of hadronization. This favours the production of many pions in proportions of approximately 1/3 π^o

and 2/3 $\pi^{\pm}$. Due to their significantly different lifetimes, the π_o and $\pi^{\pm}$ will behave quite differently in matter.

As a $\pi^{\pm}$ traverses the bulk of a material, some of its energy will be lost due to ionization. In heavy materials, most of the pions will interact with a nucleon through various nuclear processes. These nuclear interactions produce more hadrons, mostly in the form of pions but also protons and other light hadrons. As well as producing these energetic hadrons, a significant number of lower energy neutrons can be freed from their nuclei. The newly produced secondary hadrons can interact with more nucleons in order to repeat this process. The low energy neutrons will usually be lost in the detector, which contributes to the lower resolution of hadronic calorimetry compared to electromagnetic calorimetry.

A neutral pion will quickly decay after it is produced and before it has a chance to interact with the material. Neutral pions almost always decay into two photons which will then begin an electromagnetic shower. Since roughly one third of the energetic particles produced in the hadronic shower are neutral pions, a hadronic shower will also contain a large amount of energy in the form of electromagnetic showers.

For energies above around 1 GeV, the nuclear interaction cross section for a hadron in a material is approximately independent of its energy or what type of particle it is. The hadronic interaction length for high energy hadrons then depends mostly on the amount of nucleons in the nucleus, and the material's density. The hadronic interaction length of a material is typically much larger than the electromagnetic interaction length.

The nuclear interactions that occur in a hadronic shower produce situations where some of the shower energy is lost. Some of the energy will be lost due to neutron spallation, by which low energy neutrons are liberated. These neutrons can be difficult to detect, as most detectors rely on the detection of ionizing particles, and the

lower energy neutrons are unlikely to promptly interact with anything. There are other processes that can lead to lost energy, such as delayed emissions from nuclear excitations or lost binding energy from the breakup of nuclei. Energy that is not detected must be accounted for in other ways such as calibration and corrections. This is a very non-trivial problem in any hadronic calorimeter.

3.3 Calorimetry

A high energy particle's energy can usually be measured by placing sufficient instrumented material in front of the particle, and measuring the properties of the shower that develops. The shower's size is described by the radiation length or interaction length depending on whether it is an electromagnetic or hadronic shower. The position and direction of the initial particle can be determined by segmenting the detector into volumetric elements. If one were to add up all of the volumetric elements in a cylinder containing the majority of the shower, and the cylinder shares an axis parallel to the initial particle direction, then the signal strength and size of the cylinder would depend on the particle's energy and type.

3.3.1 Electromagnetic Calorimetry

The ATLAS Electromagnetic Calorimeter uses layers of lead plates and liquid argon (LAr) chambers to absorb and measure electromagnetic showers. The shower will progress mainly through the lead, and to a lesser extent in the LAr which is less thick than the lead when measured in radiation lengths. As charged particles traverse the LAr, they leave ionization trails through the LAr. The lead plates are kept charged such that the ionized particles in the LAr chamber will drift to a plate and produce a measurable signal.

There is a slight difference between a photon and an electron incident on the calorimeter. As stated before, a photon will typically travel a short distance through a material before it will interact through pair production; whereas an electron will begin emitting bremsstrahlung radiation almost immediately. However, before a particle reaches the calorimeter in ATLAS it must first pass through the inner tracking detector, a magnet system, and possibly some electrical and mechanical services. This increases the likelihood of having a photon interact before it penetrates the calorimeter, making it difficult to discern the difference between a photon and an electron using just the calorimeter. To overcome this ATLAS uses a pre-shower detector, which samples the particles before they make it to the calorimeter in order to differentiate between photons and electrons. The pre-shower detector has an added benefit of being able to contribute to differentiating photons from neutral pions which is very important for efficient photon triggering.

3.3.2 Hadronic Calorimetry

The physics of the hadronic shower makes hadronic calorimetry much more complicated than electromagnetic calorimetry. The lower momentum transfer, soft QCD interactions between hadrons and nucleons are very difficult to model, meaning simulations of hadronic calorimeter are typically less accurate. The presence of missing energy by the processes named in an earlier section also add to the difficulty of modelling hadronic calorimetry; either the energy scale of the hadronic calorimeter must be independently determined, or the calorimeter must be built specially to compensate for this lost signal.

The main components of the ATLAS hadronic calorimeter used in the barrel section are built up of layers of steel and tile scintillators. A charged particle will excite some of the atoms in the scintillator, these excited atoms will emit photons of partic-

ular wavelengths. The scintillation radiation is the signal that is measured. This type of a calorimeter is non-compensating, the detector makes has no mechanism to reduce the hadronic component of the hadronic shower, as such the jet energy scale must be determined independently. The hadronic calorimeters in the end-caps are made with copper plates and liquid argon detectors and are similarily non-compensating. The ATLAS collaboration uses various analysis techniques utilizing offline software to properly scale the jet energy in the hadronic calorimeters.

Chapter 4

The LHC and ATLAS

This chapter includes a discussion on the experimental setup that is used for this analysis. Collisions in the ATLAS (A Toroidal LHC Apparatus) detector are produced by protons accelerated and collided by the Large Hadron Collider (LHC). The ATLAS detector consists of many different sub detectors designed to ensure the energy and momentum of particles produced in the collisions are reconstructed so that they can be used to make measurements of the physics occurring within the detector.

4.1 The LHC

The Large Hadron Collider (LHC) is housed at CERN just outside of Geneva, Switzerland. It is a synchrotron particle accelerator with a circumference of 26.7 km. Each of its two beam pipes circulates either protons or lead ions in opposite directions around the ring with four interaction points where the beams intersect and detectors are located. ATLAS and CMS are general purpose detectors, LHCb is designed for b physics, and ALICE is designed for heavy ion collisions. Figure 4.1 shows a schematic of the LHC ring with the experiments indicated.

The LHC was designed to produce proton-proton collisions at a centre of mass

energy of 14 TeV at an instantaneous luminosity of $\mathcal{L} = 10^{34} cm^{-2} s^{-1}$. Initial runs in 2010 and 2011 were made at 7 TeV, and in 2012 the energy was increased to 8 TeV.

In order to bend the protons around the LHC ring at such high energies very powerful superconducting magnets are used. These magnets must be cooled by liquid helium down to around 1.9 K in order to provide a magnetic field of 8T. There are 1232 dipole magnets that channel the protons in an approximately circular orbit, and 392 quadrapole magnets that focus the proton bunches. The protons are in bunches that are separated by 50 ns in time for the data taking periods used in this thesis. The LHC design allows for bunch separations as small as 25 ns.

To accelerate the protons up to the energies achieved in the LHC, they are sent through a series of separate accelerators that were used at CERN before the LHC was built. Starting with the LINAC 2 the protons are first accelerated up to 50 MeV. The second step is an acceleration up to 1.4 GeV by the Proton Synchrotron Booster and then up to 26 GeV in the Proton Synchrotron. The final step before entering the LHC beam pipe is a boost up to 450 GeV in the Super Proton Synchrotron. The LHC then accelerates two counter-rotating beams of protons each up to one half of the desired centre of mass energy.

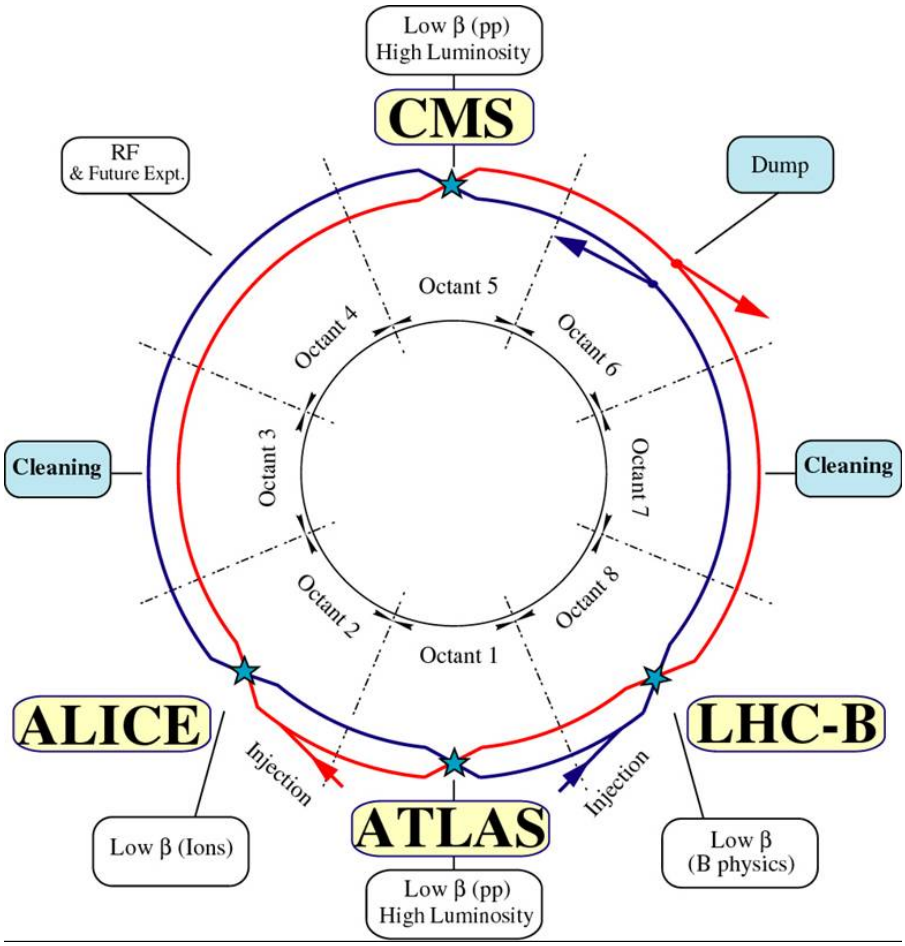

Figure 4.1: A schematic of the LHC with the location of its interaction points, beam dumps, and injection sites.

4.2 The ATLAS Detector

The ATLAS detector is one of two general purpose detectors being used to measure LHC collisions. Rather than focusing on a particular physical process, the ATLAS detector has been designed to measure almost any physical process that will result from LHC collisions [16] [17]. The flexible design ensures that any energetically favourable theory can be tested and many Standard Model measurements can be

made. It requires measuring the energy and momentum of any of the high energy particles present in a detector with state of the art accuracy.

Measuring the energy and momentum of most of the particles that are produced in LHC collisions requires a large detector with several different instrumented layers such as ATLAS, shown in figure 4.2. The momentum of most charged particles is measured by tracking their progress through a magnetic field in the ATLAS Inner Detector. The energy of most of the particles is measured using calorimetry in the ATLAS Calorimeters. Muons are difficult to absorb, since the rate at which they lose their energy to a medium is usually minimal and they are not likely to decay in the detector. In order to accurately measure any of the muons, it is necessary to include a muon detector with its own magnet system. The layers are listed in order, from closest to the LHC beam pipe to the farthest, the muon detector must be last so as to ensure only muons can make it through. This does not ensure that ATLAS will be able to detect everything; for example if neutrinos are created they will not produce a signal in the detector, and their only trace will be an amount of missing energy.

4.2.1 Inner Detector

At 6.2 meters long, and a radius of 1.05 meters, the ATLAS Inner Detector (ID)[18] is the smallest component of the ATLAS detector, and lies closest to the beam pipe. The ID has been designed to be hermetic and provide very accurate momentum measurements of charged particles. This is achieved by immersing the detector in a 2T magnetic field from a solenoidal magnet, and by using fine grained detector components to reconstruct the trajectory of charged particles (known as tracks) as the particles emerge from the interaction point (known as the primary vertex) and move outwards. A typical charged particle will create on average 36 position measurements per track[19]. Lying closest to the beam pipe, the ID allows for the accurate measure-

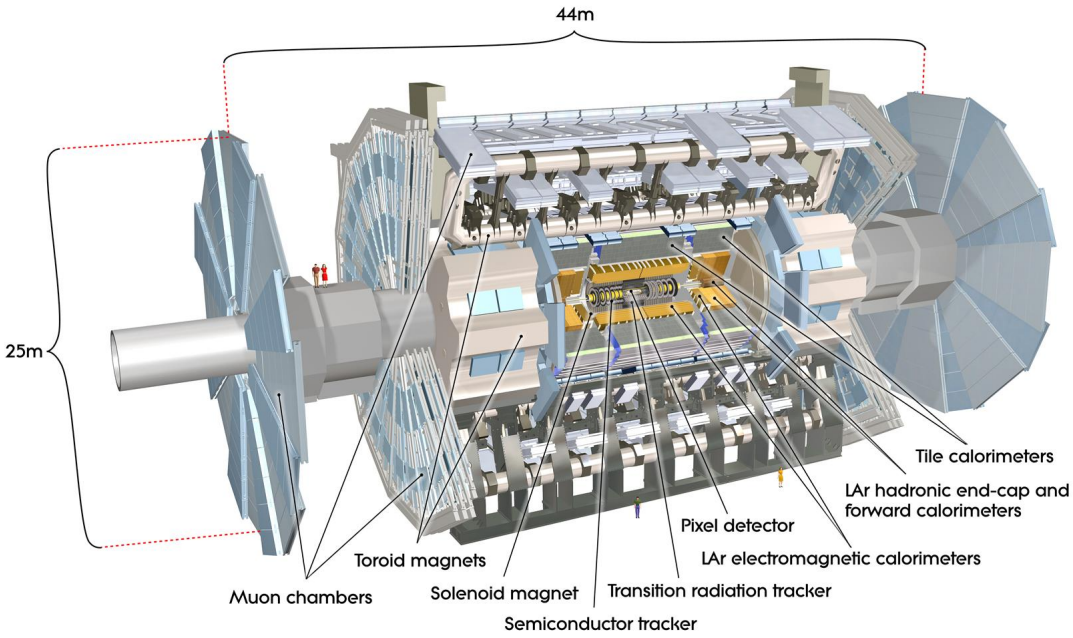

Figure 4.2: Cut away depiction of the ATLAS detector to scale.

ment of both primary vertices resulting from the initial interactions and secondary vertices resulting from particle decays. These vertex measurements are achieved using charged tracks $> 0.5GeV$ and in the range $|\eta| < 2.5$.

The ID is made up of three independent sub-detectors. Each sub-detector has its own barrel and end cap region. See fig 4.3 for a cutaway image of the ATLAS Inner Detector. The pixel detector is closest to the beam pipe with a sensitive barrel region of $50.5mm < R < 122.5mm$. The silicon microchip (SCT) sensor is the next layer with a sensitive barrel region of $299mm < R < 514mm$. The last layer of the ID is the transition radiation tracker with a sensitive barrel region of $563mm < R < 1066mm$. Figure 4.4 shows the active regions for a quarter section of the ATLAS inner detector's components.

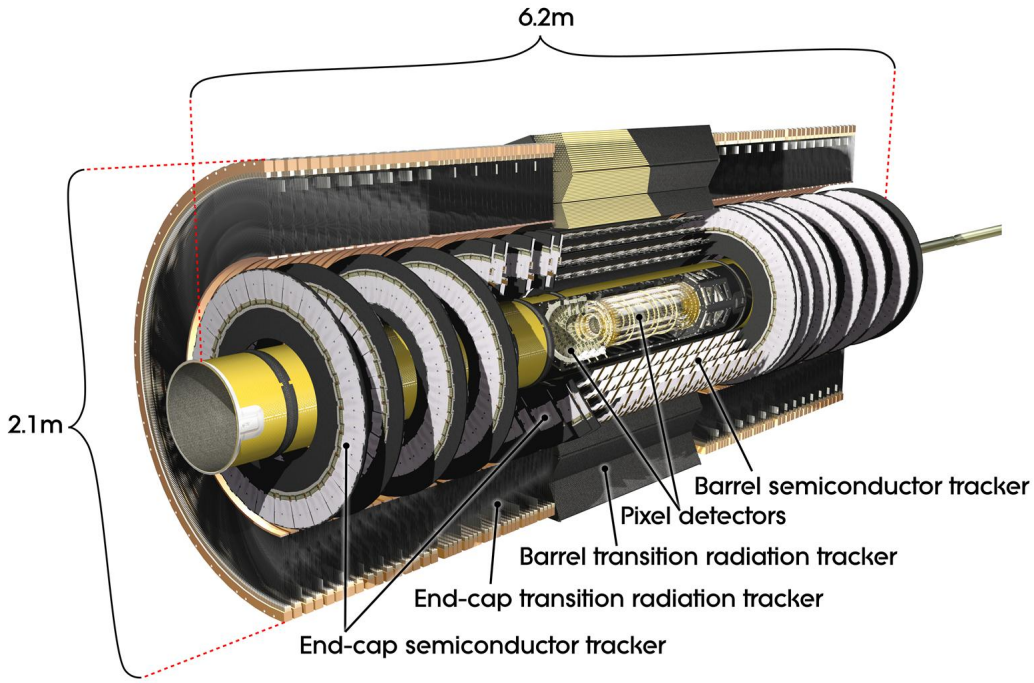

Figure 4.3: Cut away of the ATLAS Inner Detector, and its sub detectors

Pixel Detector

The pixel sub-detector consists of 1744 pixel sensors. Each sensor has 47232 pixels, and 46080 readout channels[20]. The nominal pixel size is $50 \times 400 \mu m^2$, and about 10% are $50 \times 600 \mu m^2$[20]. This sub-detector is very fine grained to provide accurate vertex measurements. It has a $10 \mu m$ azimuthal resolution in the $R - \phi$ plane, and a $115 \mu m$ longitudinal resolution in z (or R in the end cap)[20].

Silicon Microstrip Detector

The silicon microstrip (SCT) sub-detector is made up of 15912 sensors[21, 22]. Each sensor has 768 12cm long active strips[21, 22]. It provides a $17 \mu m$ azimuthal ($R - \phi$) resolution, and a $115 \mu m$ longitudinal (z in barrel or R in end cap) resolution[21, 22].

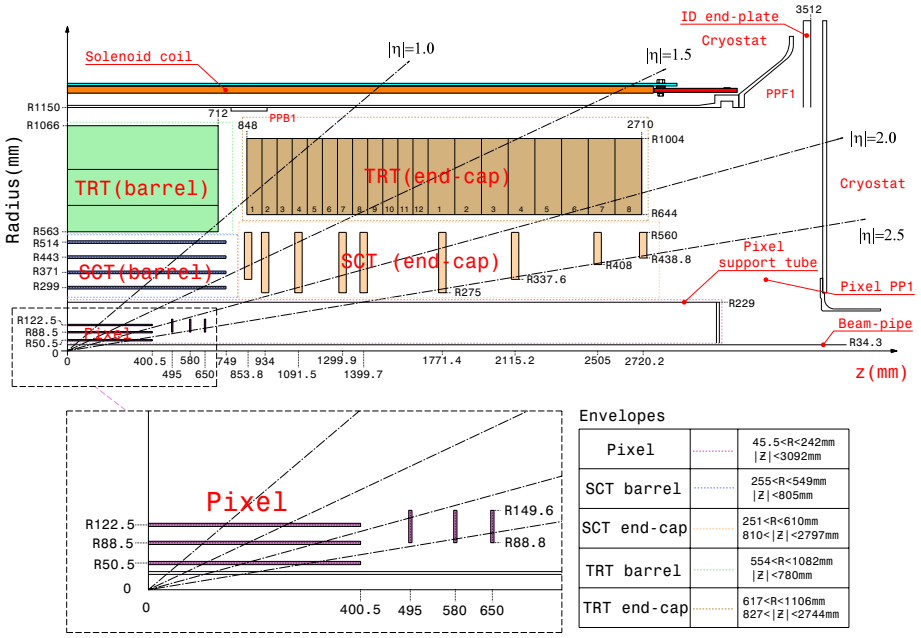

Figure 4.4: Quarter-section of the ATLAS inner detector demonstrating the sub-detectors and the active regions[19].

Transition Radiation Tracker

The transition radiation tracker (TRT) sub-detector is made up of layers of straw tubes. These tubes are filled with an air mixture of $70\%Xe, 27\%CO_2, 3\%O_2$[23]. In the barrel region there are 73 layers, and in the end cap region there are 160 straw planes. The TRT provides a z resolution of $130\mu m$[23].

4.2.2 Calorimetry

ATLAS calorimetry has been designed to absorb and measure the energy of most of the particles that enter it. In order to absorb all of the energy in any electromagnetic or hadronic shower, the calorimeters have been built with a thickness of 11 interaction lengths (at $\eta = 0$). Producing the best energy measurements requires multiple calorimetry components. See fig 4.5 for a cutaway of the ATLAS calorimetry.

There are three subsystems that make up the ATLAS calorimetry system. In order

to produce high resolution electron and photon energy measurements, an electromagnetic calorimeter is the first detector particles will traverse after the ID. The electromagnetic calorimeter lies inside of a larger hadronic calorimetry system designed to contribute to E_T^{miss} measurements as well as perform efficient jet reconstruction. The EM Calorimeter and the Hadronic Calorimeter provide effective calorimetry for $|\eta| < 3.2$. In order to cover the high $|\eta|$ regions, there is also a forward calorimeter. This combination of calorimeter detectors allow energy measurements up to $|\eta| < 4.9$.

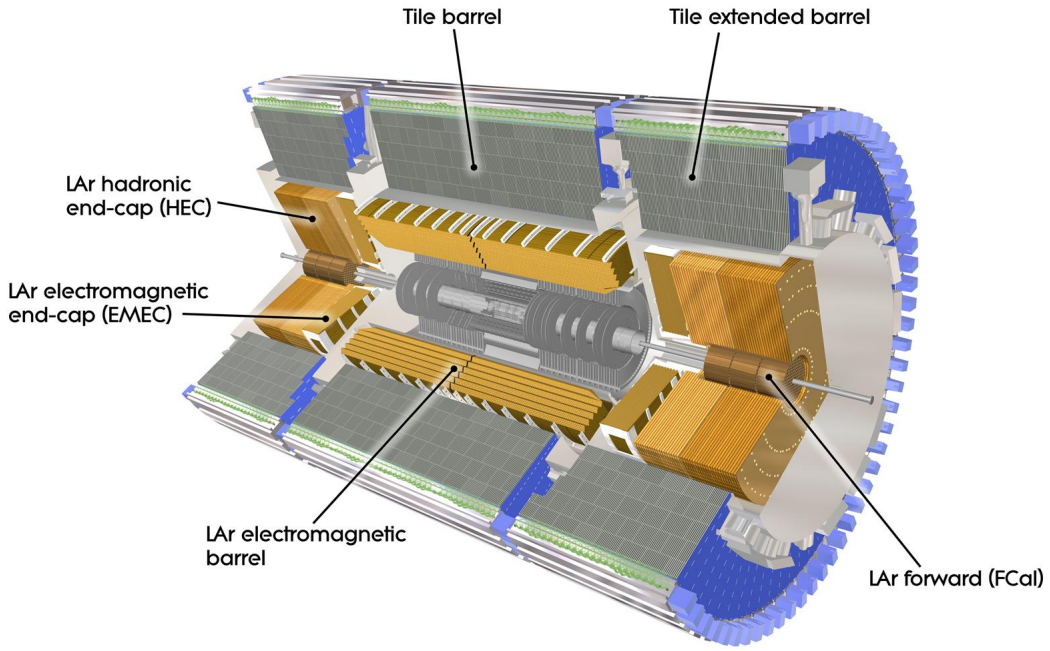

Figure 4.5: ATLAS Calorimetry including the LAr barrel and FCal, and the Tile barrel and extended barrels

Electromagnetic Calorimetry

The EM Calorimeter barrel ($|\eta| < 1.47$) and the two wheels, one in each end cap ($1.375 < |\eta| < 3.2$) are lead LAr detectors[24]. These detectors consist of lead absorber plates with gaps filled by LAr. The absorber plates are laid out in an accordion

shape in order to provide azimuthal symmetry and hermiticity. The thickness of the absorber plates varies with η to optimize performance. The EM Calorimeter also has a presampler in the part of the tracking region $|\eta| < 1.8$. The presampler samples the energy of photons and electrons before they enter the absorbers, which improves the overall energy resolution. The LAr EM Calorimeters provide an energy resolution of $\frac{\sigma_E}{E(GeV)} = \frac{10\%}{\sqrt{E(GeV)}} \oplus 0.07\%$.

Hadronic Calorimetry

The Hadronic Calorimeter has several parts: there is a barrel ($|\eta| < 1$), two extended barrels ($0.8 < |\eta| < 1.7$), and two wheels in each end cap ($1.5 < |\eta| < 3.2$). These components allow for an energy resolution of $\frac{\sigma_E}{E(GeV)} = \frac{50\%}{\sqrt{E(GeV)}} \oplus 3\%$.

The barrel and extended barrels are tile calorimeters[25], using layers of steel absorber with scintillating tiles. The layers are 7.4 interaction lengths thick combined, but the barrel and extended barrels have layers of different thicknesses.

Each LAr hadronic end cap is made up of two independent wheels. Each of these wheels is two sandwiches containing layers of copper plates with LAr gaps.

Liquid Argon Forward Calorimeter

The forward calorimeter covers $3.1 < |\eta| < 4.9$, it has three layers with an absorber and a LAr active material. The first layer is copper, meant to measure electromagnetic showers, the last two layers are tungsten. Together these three layers are 10 interaction lengths deep. The FCal provides a hadronic energy resolution of $\frac{\sigma_E}{E(GeV)} = \frac{100\%}{\sqrt{E(GeV)}} \oplus 10\%$

4.2.3 Muon Spectrometer

Muons that are produced within the ATLAS detector with transverse momentum greater than a few hundred MeV/c will make their way through all of the detector material. In order to better identify them, and measure their momentum, ATLAS uses a dedicated muon detector (see fig 4.6). The muon spectrometer[26] primarily relies on magnetic deflection of charged tracks.

There are three magnets that make up the muon magnet system. There is a large barrel toroid for $|\eta| < 1.4$ which provides 1.5 Tm to 5.5 Tm of bending power. There are also two end cap magnets for $1.6 < |\eta| < 2.7$ providing 1 Tm to 7.5 Tm of bending power. These magnets are all air core superconducting toroidal magnets. The magnetic fields are aligned such that they are orthogonal to the direction of the incoming muon, and the field direction of the inner barrel solenoid magnet.

The muon spectrometer has a number of different types of sensors in order to measure muon tracks. Precision position measurements are performed by the Monitored Drift Tubes (MDTs)[26]. The MDTs cover $|\eta| < 2.7$ and each chamber provides a resolution of 30 μm. Cathode Strip Chambers (CSCs)[26] are used in the forward region $2 < |\eta| < 2.7$. CSCs have better rate capability and time resolution. They provide a resolution of 40 μm in the bending plane and 5mm in the transverse plane.

The muon spectrometer also has its own triggering system. This system allows for bunch crossing identification, well defined P_T thresholds, and measures all of the muon coordinates. In the barrel, $|\eta| < 1.05$, this is done with Resistive Plate Chambers [27] and in the end caps, $1.05 < |\eta| < 2.4$, Thin Gap Chambers [26] are used.

4.2.4 The Trigger System

When running at its design luminosity, the LHC will produce bunch crossings at an astounding rate of 40MHz. This would correspond to producing about 40 TB of data

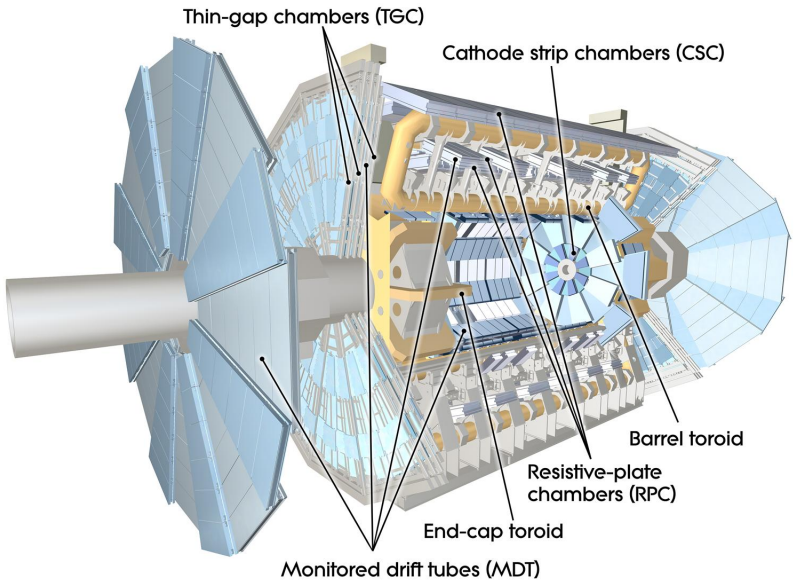

Figure 4.6: ATLAS muon systems

every second, the recording of which would be an impossibly expensive task. However, not every event (an event in ATLAS is a snap-shot of all of the collisions during a beam crossing) is useful to the physicists analyzing this data, and some events are more useful than others. In order to reduce the rate of data that is to be stored, while sorting out the useful events, an advanced triggering system is used.

The ATLAS trigger system has three levels. The goal of each trigger level is to reduce the event rate without throwing away events that are useful for physics studies. The three triggers are the level 1 (L1) trigger, the level 2 (L2) trigger, and the event filter (EF). Typically the L2 trigger and the EF combined are referred to as the high level trigger (HLT). The L1 trigger is purpose built hardware, where as the HLT uses software and information from the L1 trigger.

The L1 trigger uses information from the calorimeter and muon spectrometer to identify regions of interest (ROIs) which will be used by the HLT. Events that pass the L1 trigger are required to have substantial transverse momentum, this ensures

selected events have come from a hard scatter. This trigger reduces the event rate from the nominally designed beam crossing rate of 40 MHz down to 70 kHz, with a decision time of about 2 μs.

The L2 trigger uses the information passed on from the L1 trigger. This trigger investigates the ROIs using the full granularity of all the ATLAS sub detectors. The event rate from the L2 trigger is further reduced from 70 kHz down to around 3.5 kHz with a decision time of about 40 ms.

The EF is seeded by the L2 trigger. It uses complex software algorithms in order to further reduce the event rate down to around 200 Hz with a decision time of 1-4 s. Events pass the EF at a rate that is manageable to write to disk, and thus are written for offline analysis. The EF is mainly limited by the quality of the calibration data that is known during the run.

Often the criteria for passing a trigger is not sufficient to reduce the event rate to the desired output. To overcome this problem, a prescale can be applied to any level of trigger. A prescaled trigger is designed to let a only predetermined fraction of events pass. For example a trigger with a prescale of 100 would only allow one out of every 100 of a type of event to pass. Prescaling triggers are very useful for reducing the event rate. Another way event rates are reduced is by increasing trigger thresholds. Thresholds are employed by examining the transverse momentum of specific objects in the event; a 10 GeV photon trigger requires there to be at least one photon in the event that with a transverse momentum greater than 10 GeV.

Chapter 5

ATLAS Computing Model

ATLAS uses advanced algorithms for sifting through data, and reconstructing physics objects as well as advanced computational methods to distribute the data and MC samples that are collected and generated.

5.1 Data

5.1.1 ATLAS Data

Events in ATLAS that pass a set of triggers are written to tape at CERN's Tier-0 computing facility[28]. At this point only minimal processing and calibration is applied to the data. This processing includes classification into physics streams and the first round of object reconstruction. Each physics stream represents events with certain objects in them. There is an egamma stream for events containing electrons and photons; a muon stream for events containing muons; and a jet, tau and E_T^{miss} stream for events with jets, taus, and missing transverse energy. Separating events into different streams allows for an analysis of ATLAS data to focus on a subset of the full ATLAS data set.

Efficient processing and archival of the raw data is done by sending the data to Tier-1 computing centres. There are 11 Tier-1 sites, each receives and stores on average one-eleventh of the ATLAS data that is produced. The Tier-1 sites are not located at CERN, instead they are located around the world from France to Canada to Taiwan. The Tier-1 sites are tasked with processing the raw data, storing copies of the processed data from other Tier-1 sites, and storing Monte Carlo samples that are generated at the Tier-2 sites.

Tier-2 sites in the ATLAS computing model are often at university-operated sites. These sites are mainly used for simulations and analysis.

Data goes through a couple of processing steps before it is analyzed. Events that are reconstructed along with the raw detector information are stored as event summary data (ESDs). Each physics stream then produces analysis object data (AODs), which contain the reconstructed objects in each event. AODs can be used in an analysis but often another step of reprocessing is done by different groups studying various physics processes (working groups). Working groups produce a third derived physics object (D3PD) that is used in ROOT [29] software for analysis.

Data taken at ATLAS are divided into periods based on periods of time when consistent accelerator conditions such as luminosity and bunch grouping last a couple of weeks. Each period is divided up into runs which last a few hours; and each run is broken up into luminosity blocks that last about a minute. A luminosity block is a set of events with a single value of luminosity averaged over the collection time. In order to track data taking blocks with good running conditions, a good runs list (GRL) is produced that allows analyzers to select only good data.

5.1.2 Analysis Data

The data used in this analysis come from the egamma stream. The analysis is carried out on D3PDs prepared by the Super Symmetry working group. The selected data set represents all of the data collected in the 2011 period which are labelled periods B and D-M. These periods are the 2011 runs corresponding to collisions between protons with a center of mass energy of 7 TeV; combined they contain 277 432 258 events.

5.2 Monte Carlo

Monte Carlo simulations are ideal for modelling stochastic processes, such as nuclear decay or particle interactions. The Monte Carlo method uses pseudo-random variables to generate many instances of a stochastic event, such as a particle decay or interaction. Particle physicists can test theories by creating a Monte Carlo model of their theories, and seeing if these events are occurring in their data.

5.2.1 ATLAS Monte Carlo

Monte Carlo methods have become a necessary tool for particle physicists. In order to verify the predictions made by theorists, whether using the Standard Model or a more exotic theory, one produces a sample that should be, in a perfect situation, identical on a statistical basis to the data that is collected. There are three steps to producing these samples: generation, simulation, and reconstruction.

Generation

Generating Monte Carlo starts with choosing a model. The model must describe the result of collisions in ATLAS mathematically. A few different models are used in

ATLAS, but they all must perform a similar task. Models produce lists of initial, intermediate, and final state particles in collisions. This information is generated from the parton distribution functions, and a mathematical description of the physics being modelled.

Simulation

After particles have been generated they must be sent through a simulation of the detector. Each particle must be tracked as it progresses through the simulated detector, including particles that are created from interactions with the simulated detector material. The simulated energy deposition is recorded and digitized, a process designed to produce digital signals that would be similar to those coming from the ATLAS detector. For the purpose of simulation, ATLAS uses a program called GEANT.

Reconstruction

Similar to the readout data coming from the detector, the simulated events must be reconstructed. For this end, the digitized simulations are fed into ATLAS reconstruction software, building objects such as photons, electron, jets, etc.

5.2.2 Analysis Monte Carlo

The MC for this analysis has been simulated with PYTHIA by the SUSY working group. The samples are simulated to contain jets and photons in the final state. There are five different samples each representing a different photon P_T threshold: 17 GeV, 35 GeV, 70 GeV, 140 GeV, and 280 GeV. Each of the selected samples contain approximately one million events.

5.3 Physics Object Reconstruction and Identification

Both the data and the simulated MC sample in ATLAS must be reconstructed by sophisticated software in order to properly identify physics objects. This section explains the algorithms that are used to reconstruct photons and jets.

5.3.1 Photon Reconstruction and Identification

Most of the photons that are produced from collisions with the ATLAS detector will traverse the inner detector without leaving any tracks. This would not be true if the photon interacts with the material in the inner detector, since a photon interaction would create charged particles that would leave tracks. Photons that do interact in the inner detector are called converted photons[30], this analysis uses only those photons that do not interact, known as unconverted photons.

In order to identify objects in the electromagnetic calorimeter, ATLAS uses a clustering algorithm to collect detector cells together. The same clustering algorithm is used to build both electron and photon objects, the difference between the two mainly being the tracking information in the inner detector. ATLAS uses a sliding window clustering algorithm[31] for electromagnetic objects. This works by using a fixed sized rectangle over the cells of the calorimeter. The energy deposited in the cells contained in the rectangle is added together, and the position of the rectangle is optimized such that the transverse energy within it is a local maximum. Since photons are massless, the magnitude of the momentum of a photon is equal to the magnitude of the energy of the photon; and their direction is determined by where in the calorimeter the photons are found and the direction that they are pointing.

5.3.2 Jet Reconstruction and Identification

In order to identify and isolate jets in the ATLAS calorimetry a clustering algorithm is necessary similar to how photons and electrons are identified in the electromagnetic calorimeter. In this analysis the jets used are labelled antikt4LCtopo. The antikt4[32] is the type of clustering algorithm that is used to identify the jet objects. LCtopo refers to what has been input into the clustering algorithm, in this case it is the output of a different type of clustering algorithm that identifies energy in calorimeter cells.

The number 4 in antikt4 means that the majority of the jet should lie in a cone of $\Delta R = 0.4$. In order to carry out the algorithm, for each input the following must be computed[33]:

$$d_{ij} = min(P_{Ti}^{-2}, P_{Tj}^{-2}) \frac{(\Delta R_{ij})^2}{R^2} \tag{5.1}$$

$$d_i = P_{Ti}^{-2} \tag{5.2}$$

- P_{Ti} is the transverse momentum of the i^{th} input
- $(\Delta R_{ij})^2 = (\eta_i - \eta_j)^2 + (\phi_i - \phi_j)^2$
- R is the desired jet cone size, 0.4 in this case

The algorithm creates a list for each pair of inputs. If the smallest value is d_{ij} then objects i and j are merged and the list is recomputed. If the smallest value is d_i then object i is a complete jet, it is removed from the list and the list is recomputed.

The topological clustering algorithm that is used to provide inputs to the antikt algorithm is based on evaluating a signal to noise ratio in the cells[31]. This method is efficient at suppressing noise in clusters with many cells. It works by starting with

a seed cell, defined by meeting a threshold signal to noise ratio. Neighbours of cells that are already in the cluster are added in if their signal is above a threshold that is above the expected noise level.

The energy, momentum and mass of jets is more complicated to calculate than for photons. Each cluster identified as above is assumed to be massless, the magnitude of their momentum is equal to the energy deposited in the cluster, and the direction of the momentum is determined by where the energy is deposited in the cluster relative to the primary vertex of the event. When the clusters are collected together to produce a jet, all of their four momenta are also added together to produce the jet's four momentum. This produces a non-zero jet mass, which corresponds to the mass of the initial parton only for top quarks, meaning the magnitude of the jet momentum will not end up corresponding exactly to the energy deposited in the calorimeter for that jet.

Chapter 6

Analysis Method

The methodology by which this analysis has been carried out is described in detail in this chapter. The chapter begins with a description of the event selection used to identify direct photon events in the ATLAS data and MC sets. MC smearing corrections are produced for a number of different regions based on the kinematics of the jets. The choice of binning is described in the binning section. The next couple of sections describe how the smearing corrections are generated and how they are applied to the MC. Finally the last section explains the closure test that is done to compare the newly corrected MC to the data providing a measure of the effectiveness of this method.

6.1 Event Selection

This analysis relies on selecting appropriate events containing direct photons for the data and Monte Carlo samples. This section describes the steps necessary to select these events.

In the data, events are first compared to a good run list. The good run list is a list of which luminosity blocks are usable in an analysis, and which are not. The

decision is made by each data production group and is based primarily on the status of ATLAS's sub-detectors. For this analysis, the data set and good run list are both produced by the SUSY group.

It is possible that the data from the calorimeters is not from an actual proton proton collision even if an event passes the good run list. The quality of both the LAr and tile cells are monitored while the ATLAS machine is operating, and their status is recorded with the data. The events with poor tile or LAr conditions have been removed in this analysis.

A set of photon triggers that use a combination of hardware and software to identify photons in an event is used in this analysis. These triggers have transverse energy thresholds of 20, 40, 60, and 80 GeV. The 20, 40, and 60 GeV triggers have been prescaled; to account for this the events that were passed with these triggers have been weighted by the prescale value.

Objects identified as photons in the event are required to have a transverse momentum of at least 10 GeV/c more than the trigger threshold. Additionally photons must satisfy specific requirements designed to reduce possible mis-identification. An outline of these requirements are listed as follows: the photon must be in the tracking range ($|\eta| < 2.37$), but not be in the uninstrumented crack region between the electromagnetic barrel and end cap ($1.37 < |\eta| < 1.52$). The majority of the transverse energy must be deposited in the electromagnetic calorimeter and the shower width in all layers of the electromagnetic calorimeter is discriminated against to eliminate diphoton showers that could be caused by neutral hadron decays. This type of photon selection criteria is known as tight selection. Additionally, photons are checked against each electron in the event with transverse momentum greater than 10 GeV/c. If a photon has been reconstructed as an electron as well then it is more likely to be an electron and is rejected. The criteria that is used to determine if a photon overlaps

with an electron is $\delta R = \sqrt{(\eta^{\gamma} - \eta^{e})^2 + (\phi^{\gamma} - \phi^{e})^2} < 0.2$.

The transverse momentum of the jets must be at least 30 GeV/c, this corresponds to the lowest photon transverse momentum cut. Hardware problems, changes in the LHC beam conditions, and cosmic showers can produce fake jets, which are discriminated against based on calorimeter quality and kinematic cuts; this has been done by the ATLAS jet and missing energy group. Accepted jets are compared to photons and electrons in the event to determine if they have been reconstructed as multiple objects. The criteria that is used to compare a jet to a photon or electron is for $\delta R < 0.3$. If the jet has also been reconstructed as an electron or a photon it is rejected.

Events are only considered for this analysis if there have not been any electrons, muons, or taus reconstructed with transverse momentum above 10 GeV/c. Each event may only have one jet and one photon that has passed the selection requirements detailed above. The final requirement is that the jet and photon must be kinematically balanced, meaning $|\delta\phi| = |\phi^{jet} - \phi^{\gamma}| > 2.9$. If an event passes the criteria above, it is considered by this analysis to be a direct photon event.

Due to the large size of the data sets that have been analyzed, the event selection described above is carried out on the ATLAS computing grid, which is a collection of computers allocated for analysis purposes operating on the ATLAS Tier 2 sites. Running on the grid over data sets this large can take days. In order to avoid such a large turn around time, this event selection is carried out on the grid and useful properties such as the kinematic variables of the jets and photons are retrieved and stored locally. The event selection criteria chooses 642 441 events in the 2011 $\sqrt{s} = 7$ TeV ATLAS data set, and 200 028 events in the MC sample.

6.2 Binning

The jet resolution is expected to vary depending on the detector geometry. This analysis is carried out on independent bins based on the jet's η, ϕ, and P_T. After direct photon events have been identified and selected their appropriate bin is determined. The binning choice is explained below.

The η bins have been selected to correspond to the geometry of the hadronic calorimeter. There is one bin for each half barrel ($|\eta| < 1$); one bin for each extended barrel ($1 < |\eta| < 1.7$); one bin for each end cap ($1.7 < |\eta| < 3.2$); and one bin for each forward calorimeter ($3.2 < |\eta| < 4.9$). The event selection described in the previous section selects limited events in the forward calorimeter. To provide sufficient statistics in these η ranges, there will not be any ϕ or P_T binning for $3.2 < |\eta| < 4.9$.

In ϕ the detector is split into four quadrants and the choice of phi bins reflects this. There are two bins for the top half of the detector ($0 < \phi < \frac{\pi}{2}$ and $\frac{\pi}{2} < \phi < \pi$), and two bins for the lower half ($\frac{-\pi}{2} < \phi < 0$ and $-\pi < \phi < \frac{-\pi}{2}$).

The P_T bins have been selected in order to ensure a roughly even number of events in each bin. Three bins have been selected with 30 GeV$< P_T <$ 45 GeV, 45 GeV$< P_T <$ 70 GeV, and $P_T >$ 70 GeV.

The binning choices explained above will produce seventy-four different bins. Z is calculated for each event according to equation (2.3), and its value is filled into a histogram. This is done separately for the data and for the MC. These histograms are filled on local computers event by event, and each event is weighted by a certain amount.

For the data, each event is weighted by the luminosity of the data. This luminosity is calculated by the ATLAS luminosity calculator tool. The tool uses the trigger information and the good run list to determine the correct luminosity for the data set. Since the tool calculates a different luminosity for each trigger, the luminosity

weighting applied to each event depends on which trigger accepted the event. The luminosity associated with each trigger is given in table 6.1.

Table 6.1: Luminosities for each trigger in 2011 ATLAS data

Trigger	Luminosity
EF_g20_loose	$12.77pb^{-1}$
EF_g40_loose	$176.5pb^{-1}$
EF_g60_loose	$999.8pb^{-1}$
EF_g80_loose	$4587pb^{-1}$
Total	$5.776fb^{-1}$

For the MC, each event is weighted according to the formula (6.1). The MC event weight is calculated by the MC generator and provided in the MC sample. The MC was produced using a fixed value for the average number of pileup interactions per recorded event. The actual pileup is luminosity dependant and accounted for by the MC pileup weighting factor. The trigger prescale is the prescale of the trigger that has accepted the event in the MC sample. The luminosity of the MC sample is different for each file and is calculated by dividing the number of events in the file by the cross section of the MC sample; both of these values are provided by the MC generator.

$$event\_weight = \frac{pileup * MC\_event\_weight * trigger\_prescale}{MC\_luminosity} \tag{6.1}$$

The rest of this chapter will ignore the binning described in this section. This is done for illustrative purposes. It is not expected to work effectively for the full MC sample since the differences between the jet energy resolution in the data and MC will depend on the kinematic properties of the jet. A comparison of the normalized Z distributions between the full data and full MC sets is provided in figure 6.1. The two distributions do not agree. A smearing function for the MC sample is calculated that should improve the agreement.

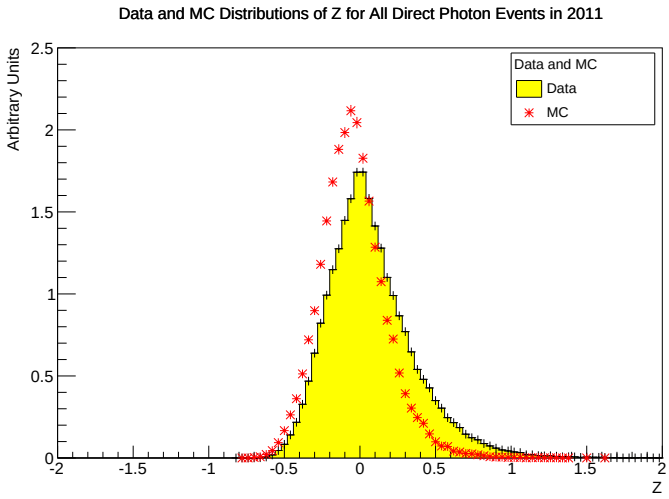

Figure 6.1: Comparison of the full data and full MC distributions of Z measured from direct photon events.

6.3 Creation of Smearing Functions

The D'Agostini [14] method described in the appendix section A.3 is used to unfold the Monte Carlo from the data. This has been done using the RooUnfold package [34] built for root. RooUnfold is designed to unfold a detector resolution from a set of experimental measurements. The inputs in this case would be a vector, or one dimensional histogram, containing the measurements; and a matrix, or a two dimensional histogram, which gives the detector resolution. Normally the resolution matrix is determined using independent methods, and represents a mapping from the value of an actual data point to that which has been measured. For the implementation here there is no resolution matrix, instead the desired result is to unfold the normalized MC from the normalized data so as to produce a distribution that when smeared with the MC will reproduce the data.

Since a matrix is required as input to the RooUnfold package, one has been built out of the MC. The process by which this has been done is motivated by considering the convolution equation, see appendix A.2 for further discussion. The following

equation shows the process used to convert the MC histogram with ν_i entries in the i^{th} bin into a two dimensional resolution histogram with R_{ij} entries in the i, j^{th} bin:

$$R_{ij} = \nu_{j-i} \tag{6.2}$$

The resolution matrix built from the MC Z distribution as described in equation (6.2) and the data Z distribution are fed into the RooUnfold package for each of the seventy-four jet bins. Three iterations are used to obtain the resulting smearing histograms. This is sufficient to ensure that the change in the χ^2 between iterations is less than one but not too small such that unnecessary errors or fluctuations are introduced.

The result of unfolding is a new histogram which represents the resolution between the data and the MC. This new histogram will be used to correct the jet P_T in the MC with the goal of producing a better agreement between the data and the Monte Carlo. Figure 6.2 shows the smearing function produced by unfolding the Z distributions in figure 6.1.

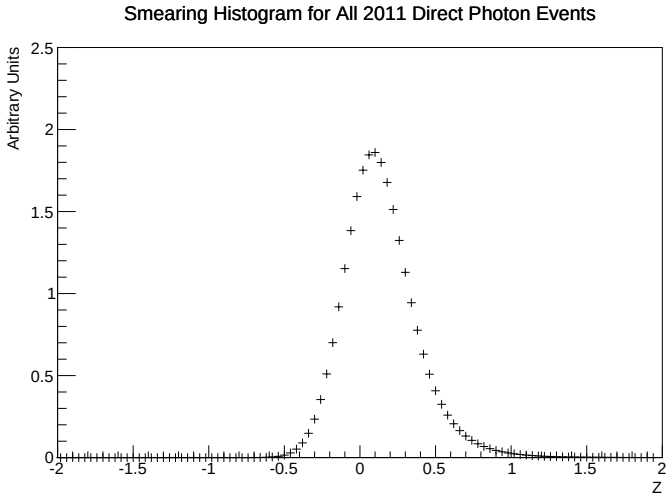

Figure 6.2: Distribution resulting from unfolding the MC from the data distributions in figure 6.1.

6.4 Correcting the Monte Carlo

The smearing distribution produced by unfolding the Monte Carlo from the data is used to smear the jet P_T in MC direct photon events. The corrected MC will be compared to the data to see if any improvement is achieved. To smear the MC a random instance of Z, Z_{rndm}, is generated from the smearing distribution corresponding to the MC jet bin. Z_{rndm} is used to smear the jet P_T, giving a $P_T^{corrected}$. Equation (6.3) below shows how this is done.

$$P_T^{corrected} = P_T(1 + Z_{rndm}) \tag{6.3}$$

$Z_{new} = \frac{P_T^{corrected}}{P_T^{\gamma}} - 1$ is then calculated and added to a new histogram. This process is repeated one thousand times producing one thousand smeared histograms for each jet bin. For the purpose of this thesis, the average of all of these smeared histograms will be compared to the data. The goal is to determine the average result of smearing. This does not represent how this correction should be applied in an independent analysis; in that case the MC jet P_T would be smeared only once. Instead taking the average of many smeared histograms is used to determined the effectiveness of this method. The normalized data is compared to the normalized average of the smeared MC in figure 6.3, and an example of the 1000 histograms collected into a single histogram is provided in figure 6.4. From here on, the normalized average of the smeared MC will be referred to as the corrected MC. The content of each bin of the corrected MC is the mean of the bin content of all of the one thousand smeared MC histograms for that jet bin. The error in this case is the standard deviation from the mean.

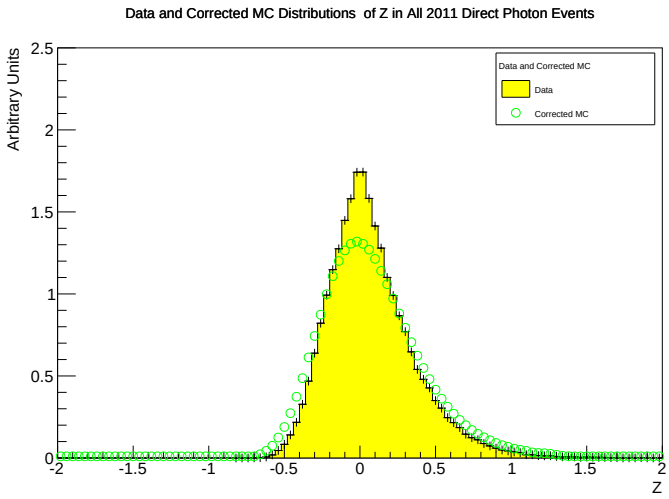

Figure 6.3: Comparison of the Z distributions between the full corrected MC set to the full data set.

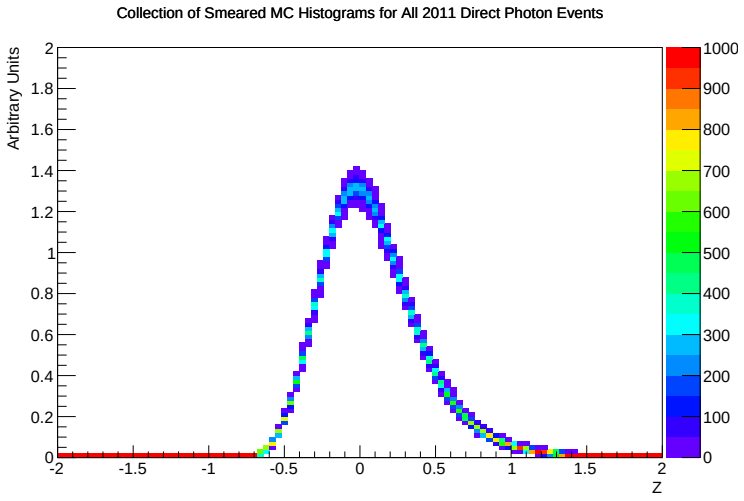

Figure 6.4: Collection of 1000 smeared MC histograms from the full data set without kinematic binning.

6.5 Comparing the Data to the Corrected and Uncorrected MC

The Monte Carlo is compared to the data both before and after corrections using a form of Pearson's χ^2 test. In each jet bin the data, MC and each of the one

thousand smeared MC are all weighted, and will be normalized by the total area of each histogram such that they can be compared to each other. The χ^2 test between two weighted histograms is explained in appendix A.5. It is expected that the χ^2 value calculated by this method will approximate the χ^2 distribution but not be exact [35]. Therefore, rather than calculate the probability from the χ^2 value, the χ^2 values and the number of degrees of freedom (NDF) will be directly compared between the MC and the corrected MC. The NDF corresponds to the number of non-zero bins of the two histograms being compared, since this is not equal for every set of histograms the value of χ^2/NDF will provide a standard test statistic for these comparisons. One more point of note is that since all of these histograms have been normalized, this test statistic is only comparing their shapes.

It is not straightforward to do a χ^2 comparison between the data and the corrected MC. This is because Root does not easily account for the errors when averaging histograms. To get around this issue, for each bin the normalized data is compared to each of the one thousand normalized smeared MC histograms. The mean of the one thousand χ^2 and χ^2/NDF for each jet bin will be used as the comparison between the data and the corrected MC.

The χ^2 test provides a comparison between the squared deviations between two distributions. This is visualized by taking the difference between the histograms that are being compared. Figure 6.5 provides an example of the difference comparisons between the data and the MC and corrected MC. Table 6.2 displays their χ^2, NDF and χ^2/NDF.

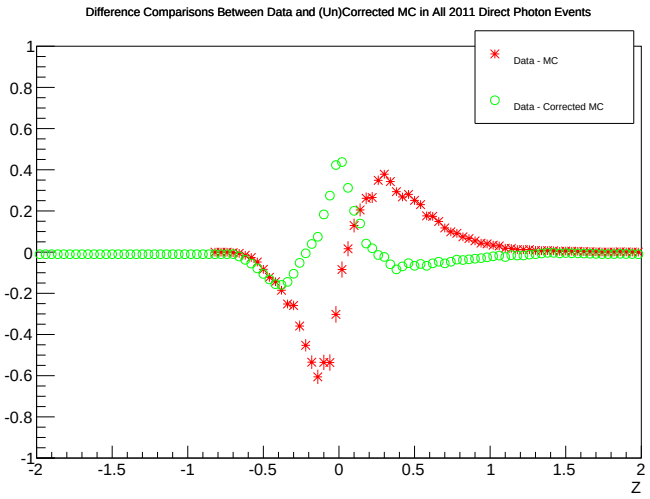

Figure 6.5: Comparison between the Z distribution in the full MC set and the full corrected MC each subtracted from the full data set.

	χ^2	NDF	χ^2/NDF
MC	8037	70	115
Corrected MC	1817 $\pm$ 54	71	25.6 $\pm$ 0.8

Table 6.2: χ^2, NDF, and χ^2/NDF for comparisons between the data and MC, and between the data and corrected MC. These comparisons do not include the jet binning. For the corrected MC the standard deviation on the mean χ^2 is provided.

Chapter 7

Results and Discussion

The full set of difference plots for this analysis is available in appendix B. This chapter provides a detailed summary of the results obtained by using the method outlined in the previous chapter. The first sections display the differences between the data and the MC with respect to the kinematic binning. The next section provides a summary of the effectiveness of this analysis, along with a summary plot showing the improvement gained as a result of this correction method. The discussion section highlights the cases where this method works less well, and provides some possible explaination as to why.

7.1 P_T Bins

The difference between the Z distribution in the data, the MC, and the corrected MC in each P_T bin is shown in figures 7.1, 7.2, and 7.3. These plots represent the differences between the data and the uncorrected MC for each P_T bin, there is no ϕ or η binning applied in these plots. For the corrected MC, what is being displayed are the events that belong to each particular P_T bin, but corrected based on the corrections calculated using the full set of η, ϕ, and P_T bins. In the next sections,

similar plots are produced for the η and ϕ binning. A summary of the χ^2/NDF between the data and the MC and the mean and standard deviation of the χ^2/NDF between the data and the corrected MC is provided in table 7.1.

P_T Bin	MC χ^2/NDF	Corrected MC $< \chi^2/NDF >$
30 GeV $< P_T <$ 45 GeV	$\frac{2244}{33}$	$\frac{2268\pm52.15}{49.35}$
45 GeV $< P_T <$ 70 GeV	$\frac{3674}{50}$	$\frac{1294\pm44.76}{70.87}$
70 GeV $< P_T$	$\frac{1235}{64}$	$\frac{139\pm17.53}{71.14}$

Table 7.1: χ^2/NDF for data compared to MC and the mean and standard deviation χ^2/NDF for data compared to corrected MC between P_T^{jet} bins in 2011 direct photon events. NDF is the number of non-zero bins in the comparison, and χ^2 is calculated using equation A.10.

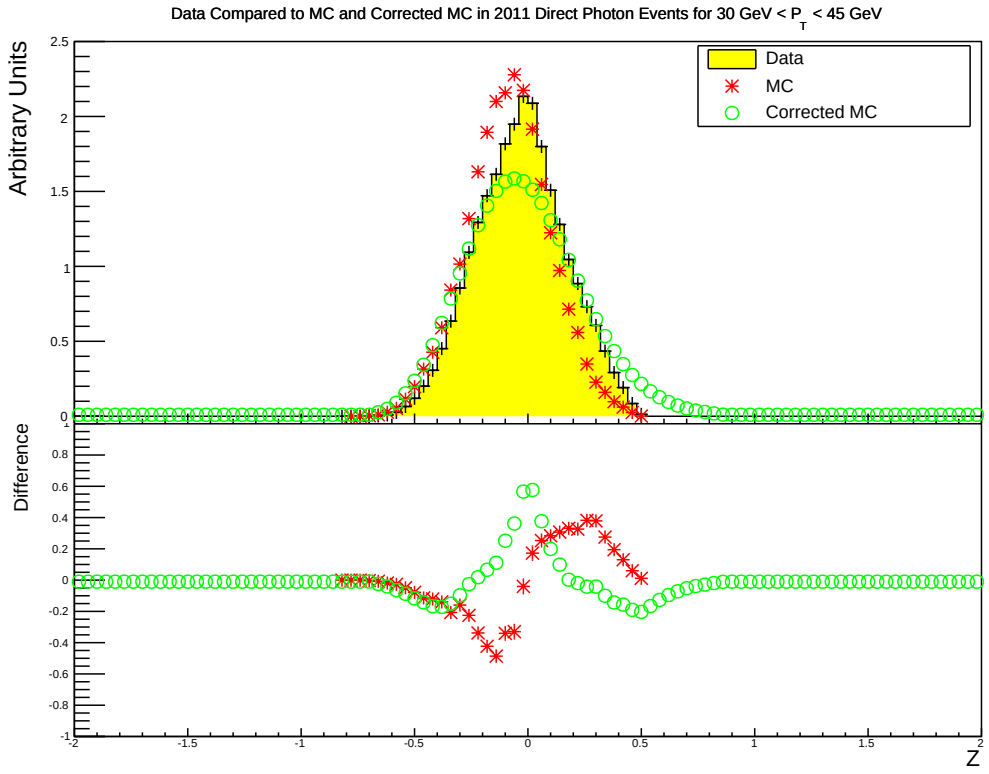

Figure 7.1: Comparison of the distributions of Z in the data, MC, and corrected MC for 30 GeV$< P_T <$ 45 GeV. The upper plot shows the data as a yellow histogram with the uncorrected MC distribution plotted as red points and the corrected MC distribution plotted as green points. The lower plot shows the difference between the data and the uncorrected MC (red) and corrected MC (green) distributions.

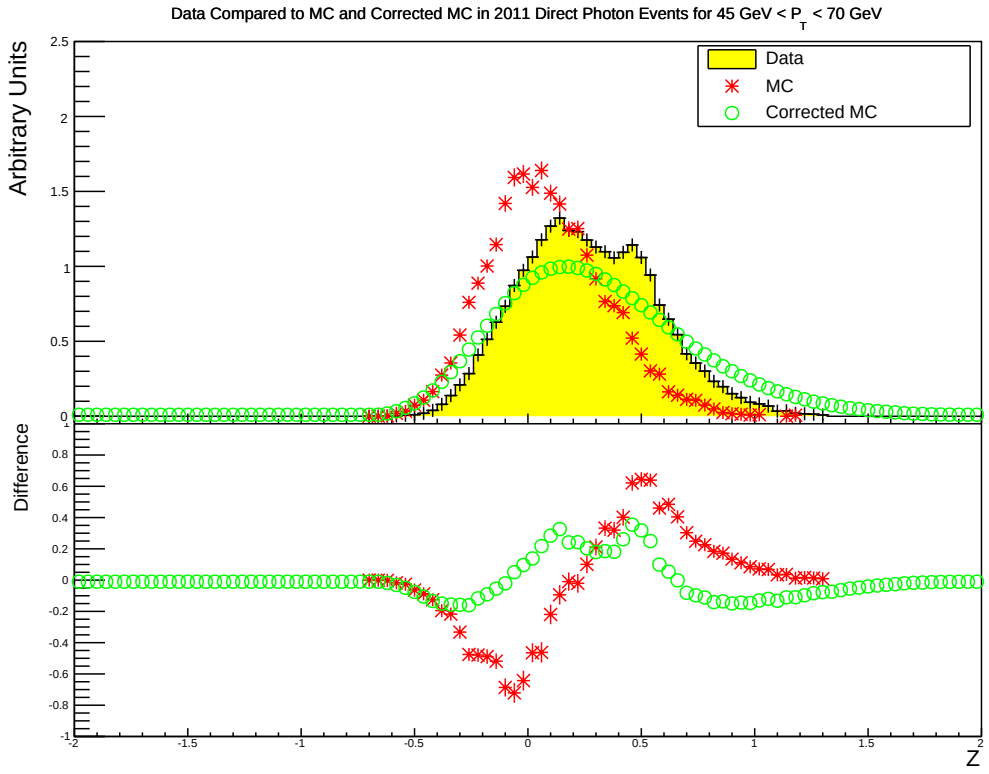

Figure 7.2: Comparison of the distributions of Z in the data, MC, and corrected MC for 45 GeV$< P_T <$ 70 GeV. The upper plot shows the data as a yellow histogram with the uncorrected MC distribution plotted as red points and the corrected MC distribution plotted as green points. The lower plot shows the difference between the data and the uncorrected MC (red) and corrected MC (green) distributions.

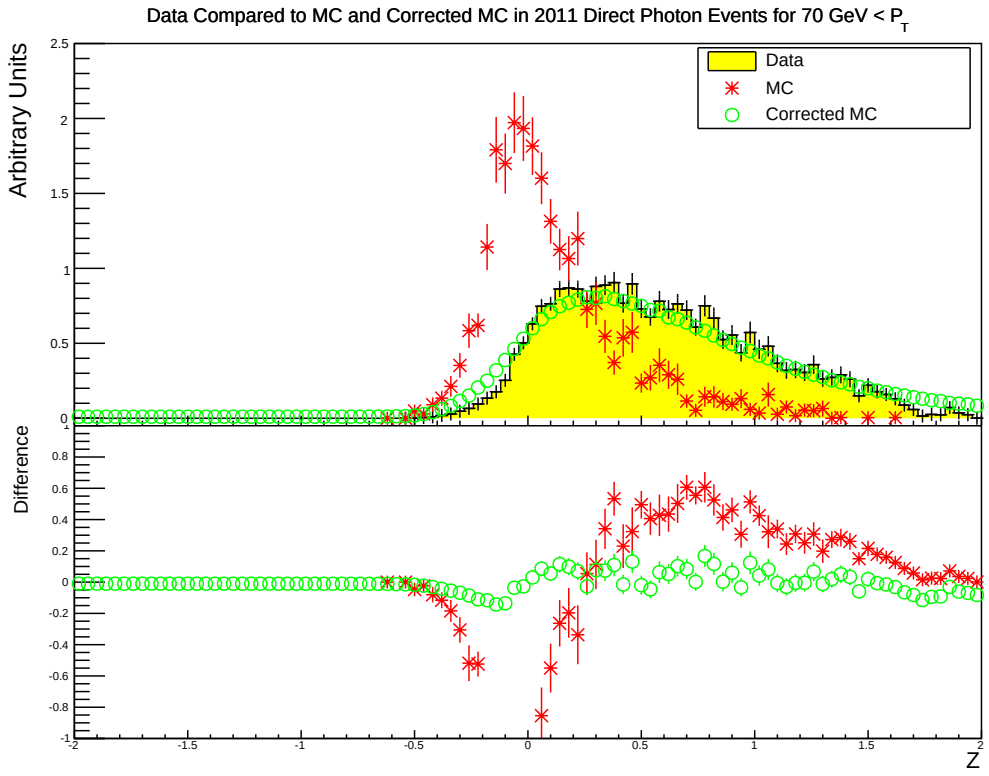

Figure 7.3: Comparison of the distributions of Z in the data, MC, and corrected MC for 70 GeV$< P_T$. The upper plot shows the data as a yellow histogram with the uncorrected MC distribution plotted as red points and the corrected MC distribution plotted as green points. The lower plot shows the difference between the data and the uncorrected MC (red) and corrected MC (green) distributions.

In the lowest P_T bin there is very little improvement after applying this correction method. The improvement in χ^2/NDF comes mainly from the increase in the number of degrees of freedom which is the result of the MC being smeared out. It is evidenced in figure 7.1 that this method smooths out the peak near $Z = 0$.

The double peaks in the data for the middle P_T bin is not well modeled by the MC. The MC correction stretches out the MC to improve the agreement.

The greatest improvement is achieved in the highest P_T bin. The large high Z

tail is hardly seen in the MC at all; however, the corrected MC includes this feature and manages to describe the data quite well.

It should be pointed out that the χ^2 method being used to compare these results is dependent on the number of entries in each histogram. The evidence for this claim is the difference in χ^2 values when comparing the MC to the data in the high jet P_T bin compared to the low jet P_T bin. There is much more discrepancy in the high P_T bin, yet the χ^2 is almost half. This discrepancy is attributable to the difference in the number of events in each bin. There are more events in the lower P_T bin which means the errors are smaller and the χ^2 calculation is inversely proportional to the square of the errors.

Since the P_T bins show such different behaviour over the different bins, some additional plots are included. Figure 7.4 shows the jet P_T distribution for direct photon events in the full data and MC sets from 2011. These distributions shows a smooth exponential decay over most of the P_T region.

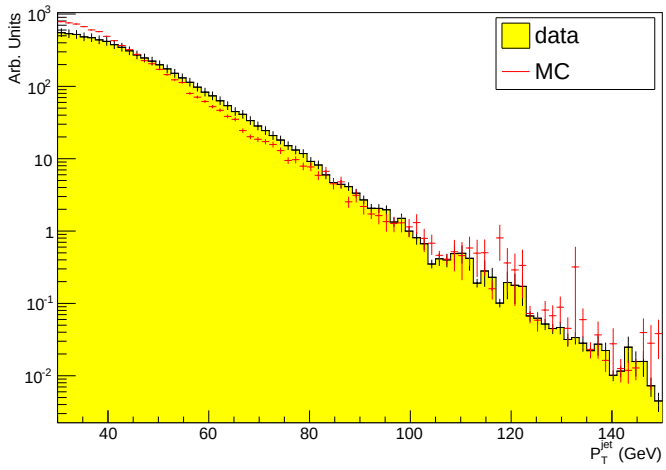

Figure 7.4: Jet P_T in direct photon events in 2011 ATLAS data and MC.

Figure 7.5 is the distribution of the jet P_T minus the photon P_T for the direct

photon events in the data and MC sets. This is essentially the variable Z from equation (2.3) unscaled by the photon P_T. The MC and data distributions peak at nearly zero, which is desirable but there is a clear discrepancy between the data and the MC, with the MC shifted to the higher photon P_T side. In these histograms, the errors are statistical which means there is a bias in the data for direct photon events with a larger photon P_T than jet P_T. This bias is expected as it is much more likely to mis-measure a jet to have less energy than it really has due to various loss mechanisms in the calorimeters. Figures 7.6 and 7.7 are two dimensional plots of the relationship between the jet P_T and the photon P_T in the data and the MC respectively. These plots show that there is a correlation between the photon and jet transverse momenta but that the distributions are broad as can also be seen in figure 7.5.

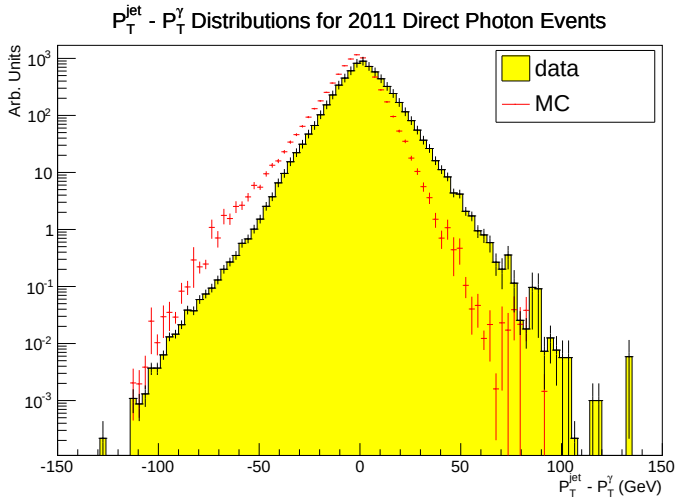

Figure 7.5: Jet P_T minus photon P_T in direct photon events in 2011 ATLAS data and MC.

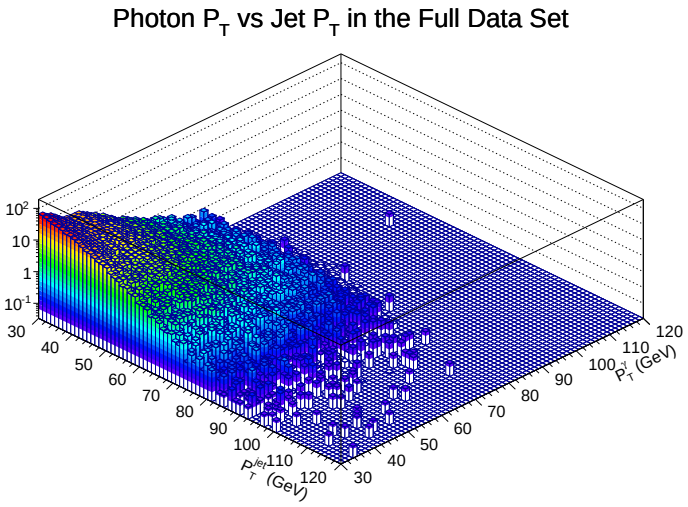

Figure 7.6: Photon P_T compared to jet P_T in direct photon events in 2011 ATLAS data in a two-dimensional histogram. The vertical axis is the total weight of all the entries in each bin.

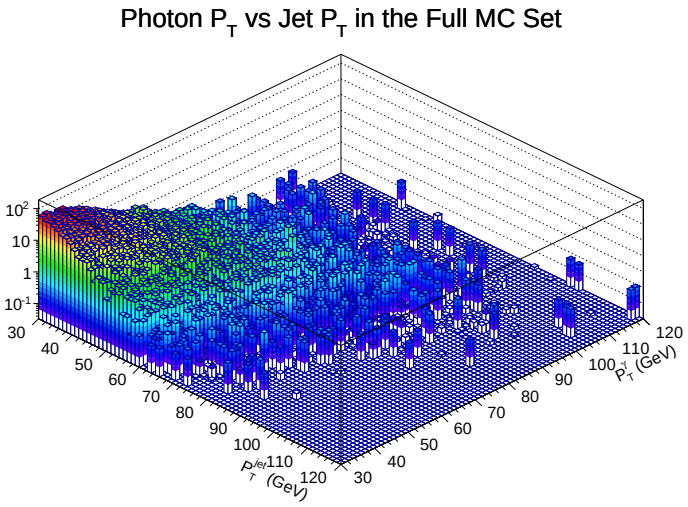

Figure 7.7: Photon P_T compared to jet P_T in direct photon events in 2011 ATLAS MC in a two-dimensional histogram. The vertical axis is the total weight of all the entries in each bin.

7.2 η Bins

The variation in the Z distributions between most of the η bins is minimal. The main difference in behavior is in the forward calorimeter region shown in figures 7.8, and 7.9. These two η regions have fewer events compared to the rest of the calorimeter regions, which are otherwise quite similar to each other. The rest of the calorimeter regions are provided in 7.10, 7.11, 7.12, 7.13, 7.14, and 7.15. Table 7.2 displays the χ^2/NDF between the data and the MC and the mean and standard deviation of the χ^2/NDF between the data and the corrected MC between the η bins. Similar to the previous section, the plots in this section represent the differences only between the chosen η bins. There is no P_T or ϕ binning applied in these plots, except when calculating the correction to the MC. These plots show again that the corrected MC describes the data better but the method over-smooths the correction near $Z = 0$ at the peak.

η Bin	MC χ^2/NDF	Corrected MC $< \chi^2/NDF >$
$-4.9 < \eta < -3.2$	$\frac{72.32}{30}$	$\frac{63.75 \pm 15.95}{31.43}$
$-3.2 < \eta < -1.7$	$\frac{888.7}{61}$	$\frac{229.2 \pm 17.69}{68.88}$
$-1.7 < \eta < -1.0$	$\frac{1137}{64}$	$\frac{286.7 \pm 20.34}{70.41}$
$-1.0 < \eta < 0.0$	$\frac{2160}{67}$	$\frac{569.6 \pm 26.29}{70.41}$
$0.0 < \eta < 1.0$	$\frac{2286}{67}$	$\frac{543.2 \pm 26.86}{70.58}$
$1.0 < \eta < 1.7$	$\frac{1148}{66}$	$\frac{275.8 \pm 20.75}{69.87}$
$1.7 < \eta < 3.2$	$\frac{911.6}{61}$	$\frac{227.8 \pm 17.68}{70.86}$
$3.2 < \eta < 4.9$	$\frac{83.35}{27}$	$\frac{62.02 \pm 15.05}{29.8}$

Table 7.2: χ^2/NDF for data compared to MC and the mean and standard deviation χ^2/NDF for data compared to corrected MC between η bins in 2011 direct photon events. NDF is the number of non-zero bins in the comparison, and χ^2 is calculated using equation A.10.

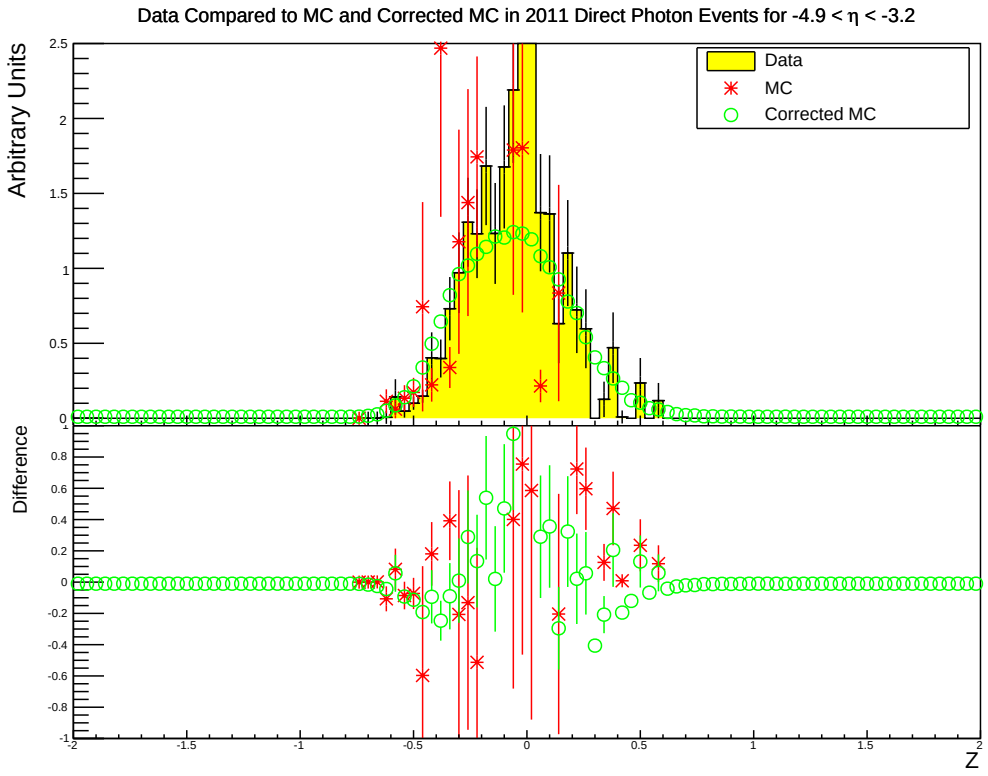

Figure 7.8: Comparison of the distributions of Z in the data, MC, and corrected MC for $-4.9 < \eta < -3.2$. The upper plot shows the data as a yellow histogram with the uncorrected MC distribution plotted as red points and the corrected MC distribution plotted as green points. The lower plot shows the difference between the data and the uncorrected MC (red) and corrected MC (green) distributions.

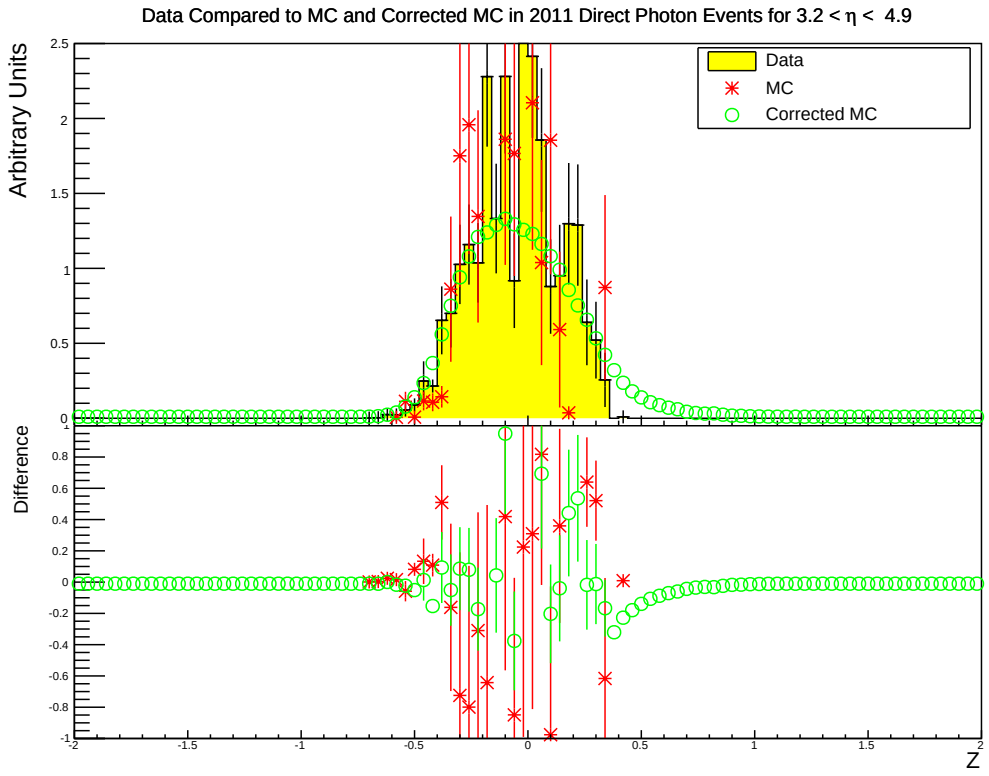

Figure 7.9: Comparison of the distributions of Z in the data, MC, and corrected MC for $3.2 < \eta < 4.9$. The upper plot shows the data as a yellow histogram with the uncorrected MC distribution plotted as red points and the corrected MC distribution plotted as green points. The lower plot shows the difference between the data and the uncorrected MC (red) and corrected MC (green) distributions.

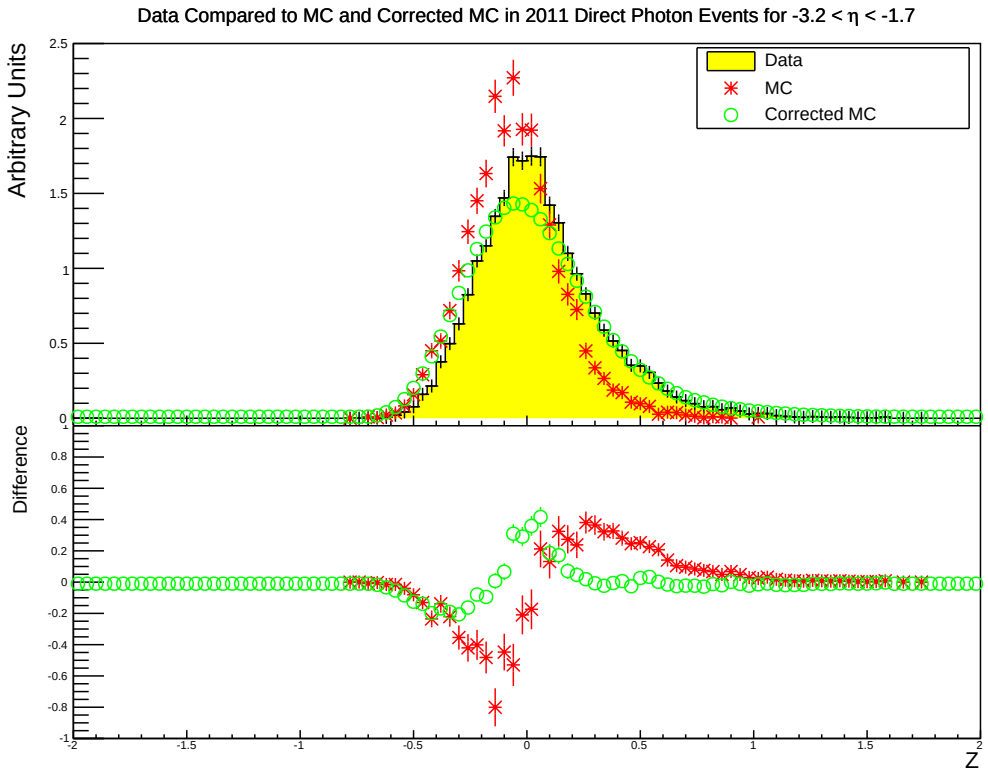

Figure 7.10: Comparison of the distributions of Z in the data, MC, and corrected MC for $-3.2 < \eta < -1.7$. The upper plot shows the data as a yellow histogram with the uncorrected MC distribution plotted as red points and the corrected MC distribution plotted as green points. The lower plot shows the difference between the data and the uncorrected MC (red) and corrected MC (green) distributions.

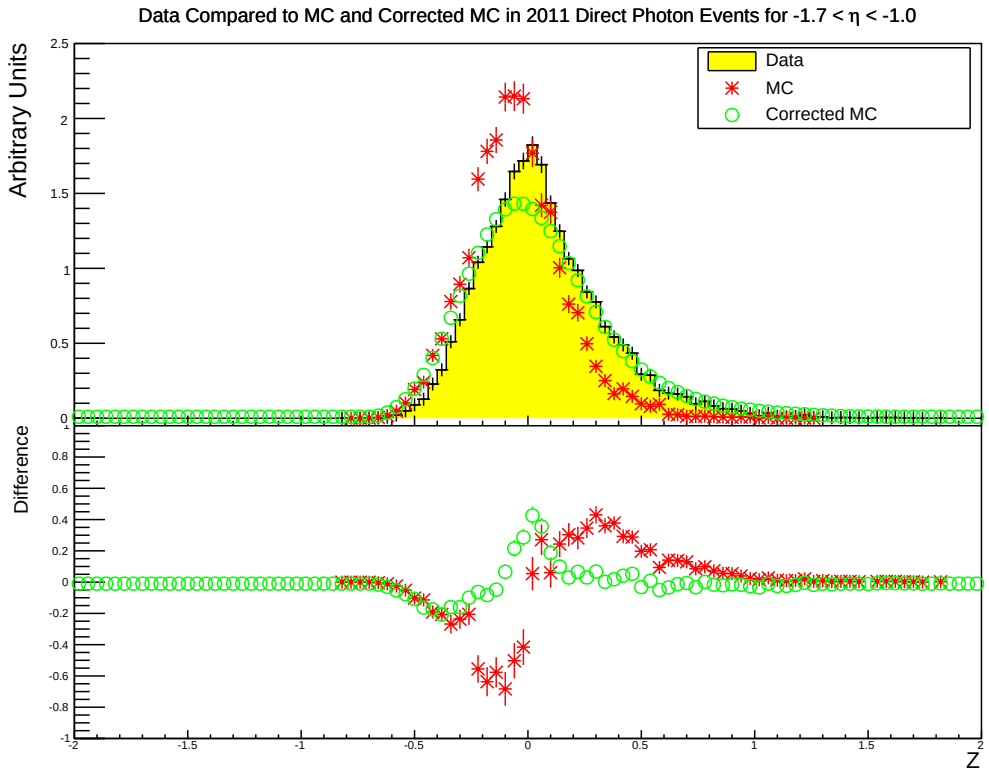

Figure 7.11: Comparison of the distributions of Z in the data, MC, and corrected MC for $-1.7 < \eta < -1.0$. The upper plot shows the data as a yellow histogram with the uncorrected MC distribution plotted as red points and the corrected MC distribution plotted as green points. The lower plot shows the difference between the data and the uncorrected MC (red) and corrected MC (green) distributions.

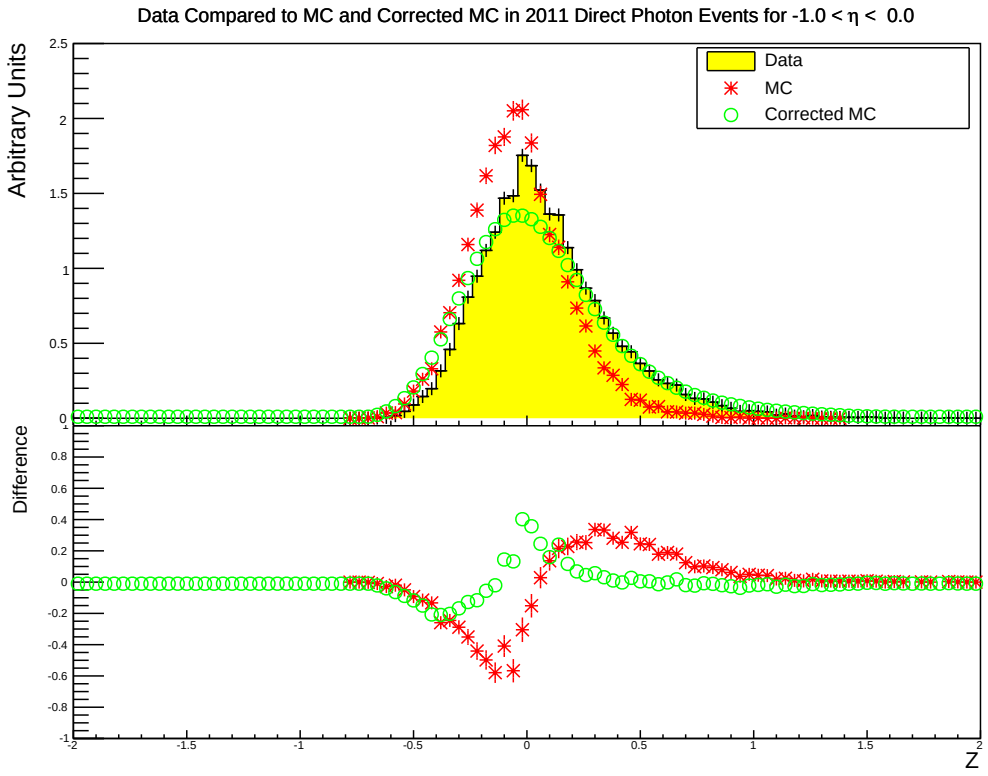

Figure 7.12: Comparison of the distributions of Z in the data, MC, and corrected MC for $-1.0 < \eta < 0.0$. The upper plot shows the data as a yellow histogram with the uncorrected MC distribution plotted as red points and the corrected MC distribution plotted as green points. The lower plot shows the difference between the data and the uncorrected MC (red) and corrected MC (green) distributions.

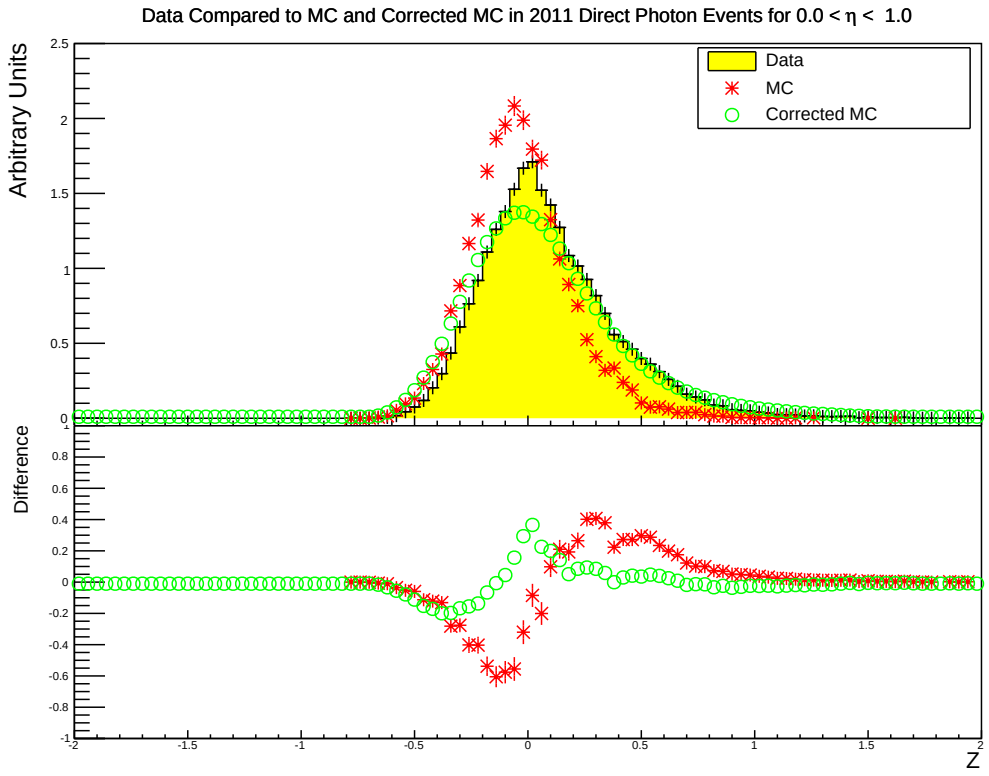

Figure 7.13: Comparison of the distributions of Z in the data, MC, and corrected MC for $0 < \eta < 1.0$. The upper plot shows the data as a yellow histogram with the uncorrected MC distribution plotted as red points and the corrected MC distribution plotted as green points. The lower plot shows the difference between the data and the uncorrected MC (red) and corrected MC (green) distributions.

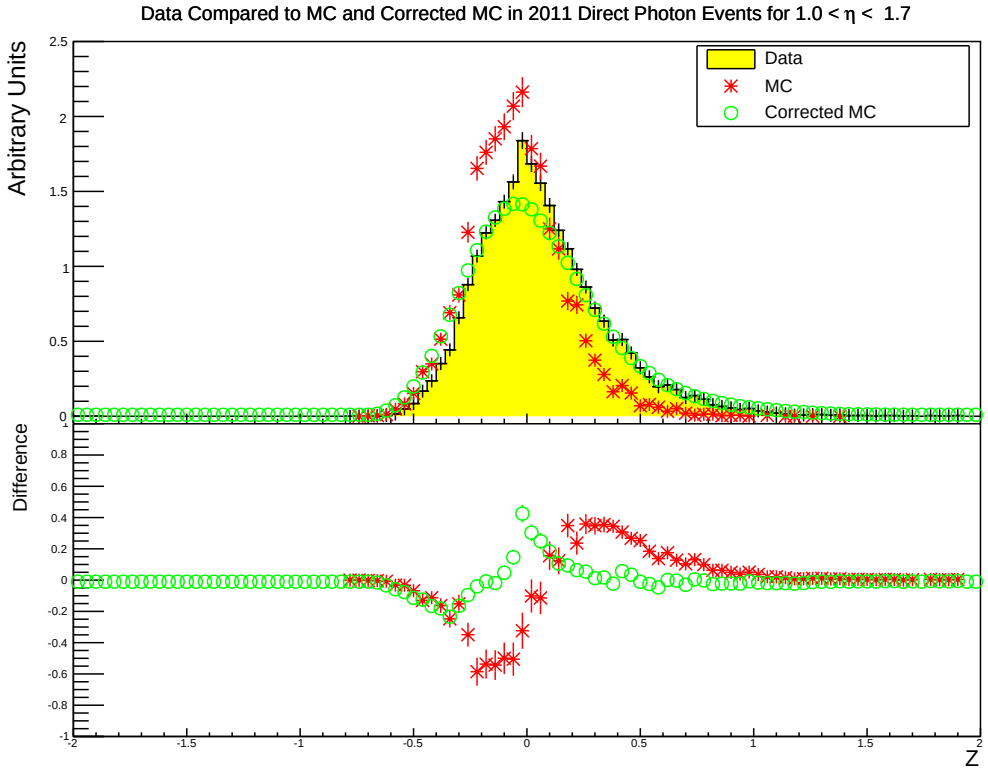

Figure 7.14: Comparison of the distributions of Z in the data, MC, and corrected MC for $1.0 < \eta < 1.7$. The upper plot shows the data as a yellow histogram with the uncorrected MC distribution plotted as red points and the corrected MC distribution plotted as green points. The lower plot shows the difference between the data and the uncorrected MC (red) and corrected MC (green) distributions.

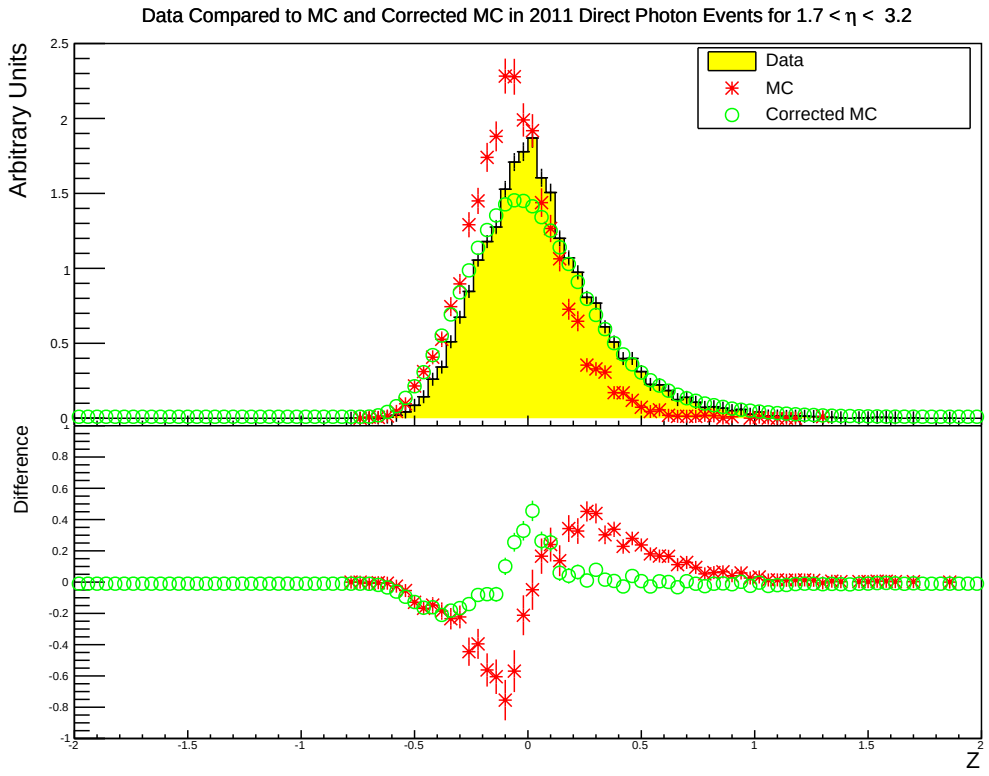

Figure 7.15: Comparison of the distributions of Z in the data, MC, and corrected MC for $1.7 < \eta < 3.2$. The upper plot shows the data as a yellow histogram with the uncorrected MC distribution plotted as red points and the corrected MC distribution plotted as green points. The lower plot shows the difference between the data and the uncorrected MC (red) and corrected MC (green) distributions.

7.3 ϕ Bins

Figures 7.16, 7.17, 7.18, and 7.19 show that each ϕ bin has roughly the same distribution for Z in data or the MC sample. This is expected as the calorimeter is designed to be symmetric in ϕ, and a discrepancy between ϕ bins should only exist if there were problems with the calorimeter that were not modeled in the MC for the majority of the 2011 data taking period. A summary of the χ^2/NDF between the

data and the MC and the mean and standard deviation of the χ^2/NDF between the data and the corrected MC between the ϕ bins is provided in table 7.3. Similar to the previous sections, the plots in this section represent the differences only between the chosen ϕ bins. There is no P_T or η binning applied in these plots, except when calculating the correction to the MC. These plots show again that the corrected MC describes the data better but the method over smooths the correction near $Z = 0$ at the peak.

ϕ Bin	MC χ^2/NDF	Corrected MC $< \chi^2/NDF >$
$-\pi < \phi < -\frac{\pi}{2}$	$\frac{2179}{67}$	$\frac{525.6 \pm 27.58}{72.15}$
$-\frac{\pi}{2} < \phi < 0$	$\frac{2081}{67}$	$\frac{480.1 \pm 25.36}{70.5}$
$0 < \phi < \frac{\pi}{2}$	$\frac{1897}{66}$	$\frac{479.1 \pm 25.03}{70.22}$
$\frac{\pi}{2} < \phi < \pi$	$\frac{2139}{67}$	$\frac{516.9 \pm 26.18}{70.72}$

Table 7.3: χ^2/NDF for data compared to MC and the mean and standard deviation χ^2/NDF for data compared to corrected MC between ϕ bins in 2011 direct photon events. NDF is the number of non-zero bins in the comparison, and χ^2 is calculated using equation A.10.

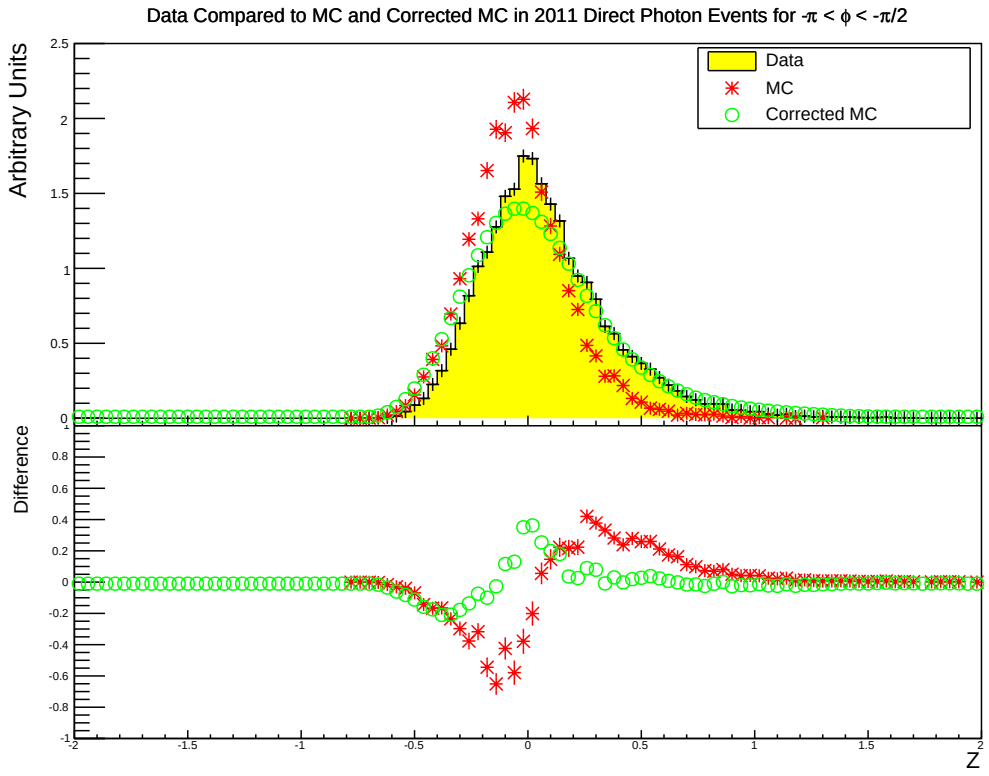

Figure 7.16: Comparison of the distributions of Z in the data, MC, and corrected MC for $-\pi < \phi < -\pi/2$. The upper plot shows the data as a yellow histogram with the uncorrected MC distribution plotted as red points and the corrected MC distribution plotted as green points. The lower plot shows the difference between the data and the uncorrected MC (red) and corrected MC (green) distributions.

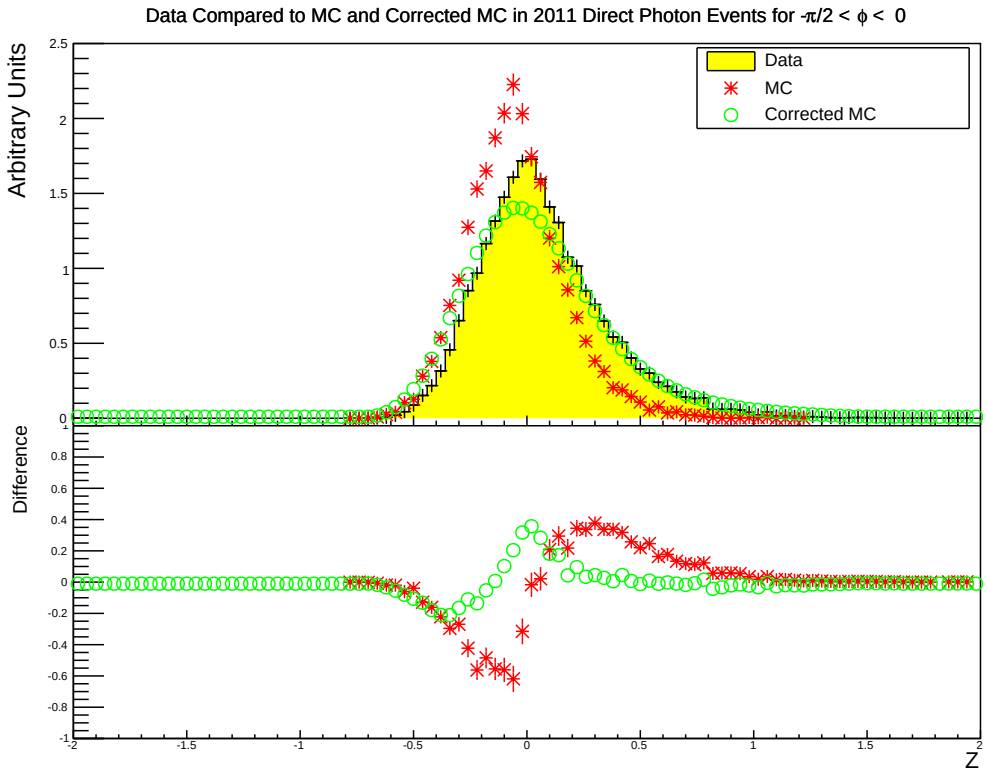

Figure 7.17: Comparison of the distributions of Z in the data, MC, and corrected MC for $-\pi/2 < \phi < 0$. The upper plot shows the data as a yellow histogram with the uncorrected MC distribution plotted as red points and the corrected MC distribution plotted as green points. The lower plot shows the difference between the data and the uncorrected MC (red) and corrected MC (green) distributions.

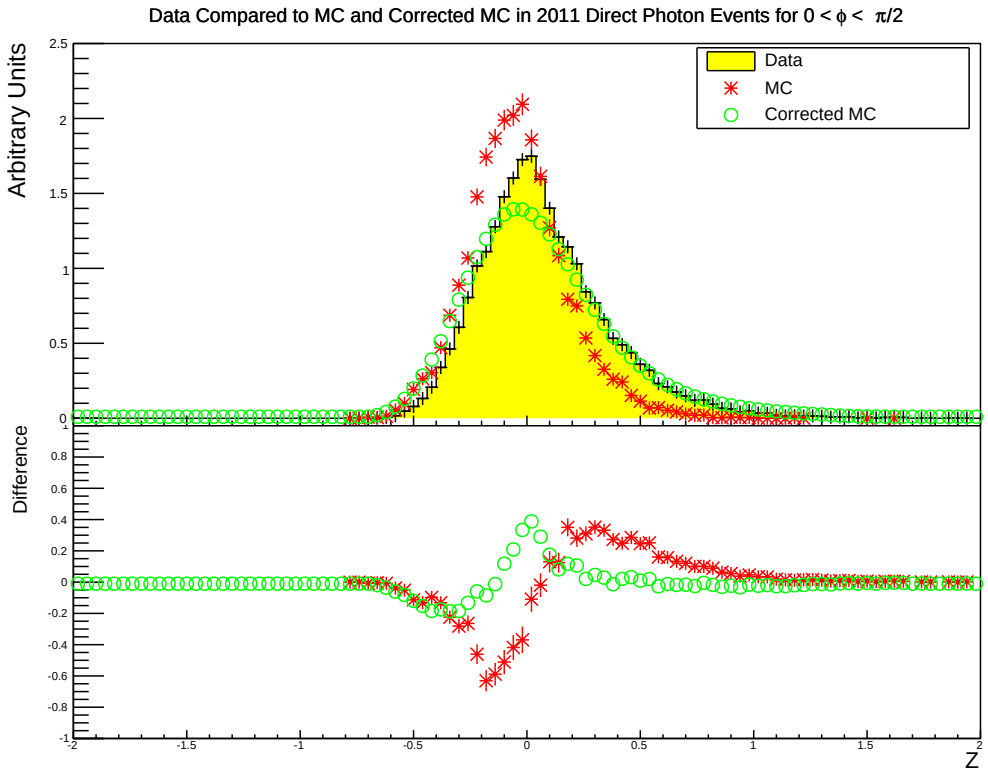

Figure 7.18: Comparison of the distributions of Z in the data, MC, and corrected MC for $0 < \phi < \pi/2$. The upper plot shows the data as a yellow histogram with the uncorrected MC distribution plotted as red points and the corrected MC distribution plotted as green points. The lower plot shows the difference between the data and the uncorrected MC (red) and corrected MC (green) distributions.

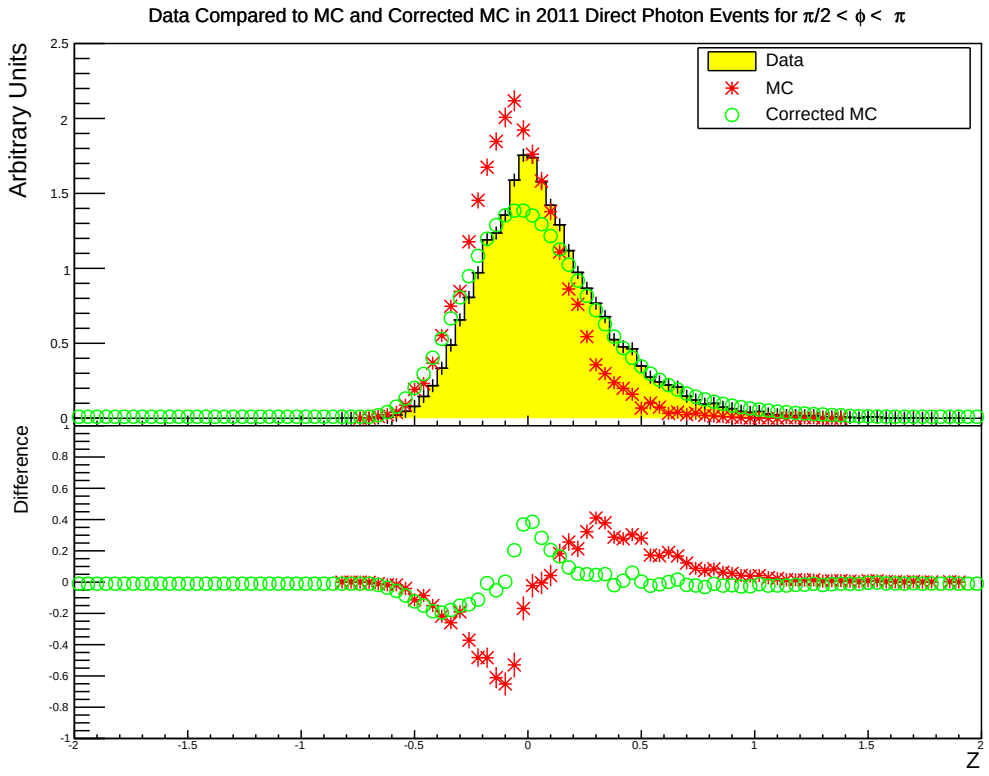

Figure 7.19: Comparison of the distributions of Z in the data, MC, and corrected MC for $\pi/2 < \phi < \pi$. The upper plot shows the data as a yellow histogram with the uncorrected MC distribution plotted as red points and the corrected MC distribution plotted as green points. The lower plot shows the difference between the data and the uncorrected MC (red) and corrected MC (green) distributions.

7.4 All Bins

Figure 7.20 presents the χ^2/NDF from comparing the data to the MC and the mean χ^2/NDF from comparing the corrected MC to the data in all the bins. This plot demonstrates the effectiveness of this method. It is easy to see that improvement is achieved on average in the corrected MC. Ideally the value of χ^2/NDF should be around one. The outliers in figure 7.20 where $\chi^2/NDF > 6$ in the MC comparison

and $\chi^2/NDF > 4$ in the corrected MC comparison mainly correspond to the central regions of the calorimeter where there are more events and so the χ^2 is testing the correction with a much higher sensitivity.

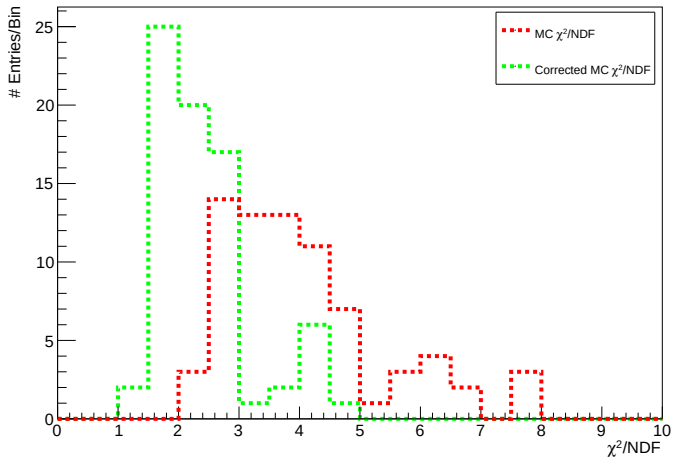

Figure 7.20: χ^2/NDF values from comparing the MC to the data (red) and the corrected MC to the data (green) in all jet bins for 2011 direct photon events.

Figure 7.21 and table 7.4 have been included below to mirror figure 6.5 and table 6.2 from the previous chapter. Earlier these comparisons were made neglecting the full kinematic binning, here the comparisons utilize the binning selection. The improvement when using the full binning choice is not evident because most of the correction is occuring in the bins with the most number of entries which dominates the comparison in both cases. It is barely noticable that the high Z tail and the peak near $Z = 0$ are better modelled here.

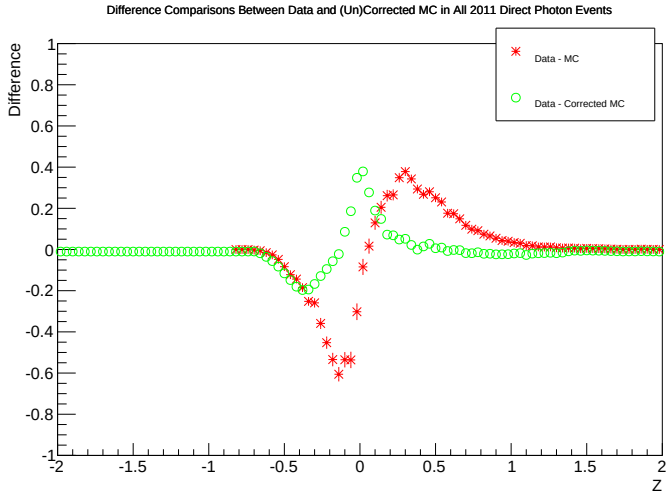

Figure 7.21: Comparison between the Z distribution in the full MC set and the full corrected MC each subtracted from the full data set.

	χ^2	NDF	χ^2/NDF
MC	8037	70	115
Corrected MC	1787 $\pm$ 47	73	24.4 $\pm$ 0.77

Table 7.4: χ^2, NDF, and χ^2/NDF for comparisons between the data and MC, and between the data and corrected MC. These comparisons include the jet binning. For the corrected MC the standard deviation on the mean is provided.

Tables 7.5, 7.7, 7.9, and 7.11 provide a summary of the χ^2/NDF values when comparing the data to the MC, and the mean χ^2/NDF values and the standard deviation of χ^2 when comparing the data to the corrected MC. Each of these tables represents a different ϕ bin and are followed by a summary of the fraction of events in each bin for the data and the MC. It is clear that in most cases the corrected MC shows better agreement to the data, even within the standard deviation of the χ^2 value.

	$P_T \in [30,45]$(GeV)		$P_T \in [45,70]$(GeV)		$P_T \in [70,\infty]$(GeV)	
η Bin	$\frac{\chi^2}{NDF}$	$< \frac{\chi^2}{NDF} >$	$\frac{\chi^2}{NDF}$	$< \frac{\chi^2}{NDF} >$	$\frac{\chi^2}{NDF}$	$< \frac{\chi^2}{NDF} >$
$[-3.2,-1.7]$	$\frac{112}{31}$	$\frac{89.6\pm10.6}{40.1}$	$\frac{193}{45}$	$\frac{103\pm16.1}{56.1}$	$\frac{125}{50}$	$\frac{119\pm25.7}{58.5}$
$[-1.7,-1.0]$	$\frac{184}{32}$	$\frac{110\pm11.9}{40.7}$	$\frac{151}{47}$	$\frac{111\pm15.8}{58.8}$	$\frac{130}{47}$	$\frac{110\pm25.6}{60.1}$
$[-1.0,0.0]$	$\frac{122}{32}$	$\frac{202\pm16.2}{43.2}$	$\frac{322}{49}$	$\frac{176\pm18.1}{63.2}$	$\frac{231}{57}$	$\frac{142\pm34.5}{63.3}$
$[0.0,1.0]$	$\frac{193}{31}$	$\frac{186\pm14.6}{43}$	$\frac{380}{49}$	$\frac{193\pm19.9}{64.9}$	$\frac{235}{55}$	$\frac{102\pm15.6}{62.6}$
$[1.0,1.7]$	$\frac{104}{30}$	$\frac{111\pm12.1}{40.4}$	$\frac{221}{46}$	$\frac{111\pm15.2}{60.2}$	$\frac{157}{54}$	$\frac{147\pm34.9}{60.9}$
$[1.7,3.2]$	$\frac{113}{30}$	$\frac{90.3\pm11.1}{39.5}$	$\frac{189}{43}$	$\frac{112\pm16.2}{56}$	$\frac{120}{46}$	$\frac{92.4\pm17.2}{57.4}$

Table 7.5: χ^2/NDF comparing data to the MC and $< \chi^2/NDF >$ with standard deviation comparing the data to the corrected MC for 2011 direct photon events with $-\pi < \phi < -\frac{\pi}{2}$.

	$P_T \in [30,45]$(GeV)		$P_T \in [45,70]$(GeV)		$P_T \in [70,\infty]$(GeV)	
η Bin	Data	MC	Data	MC	Data	MC
$[-3.2,-1.7]$	0.0134	0.0149	0.0105	0.00714	0.00252	0.00177
$[-1.7,-1.0]$	0.0165	0.0205	0.0139	0.0102	0.0034	0.00233
$[-1.0,0.0]$	0.0302	0.0412	0.0304	0.0249	0.0096	0.00759
$[0.0,1.0]$	0.0296	0.0418	0.0305	0.0251	0.0099	0.00768
$[1.0,1.7]$	0.0166	0.0204	0.0146	0.0108	0.00353	0.00234
$[1.7,3.2]$	0.0137	0.0147	0.0105	0.00711	0.00261	0.00179

Table 7.6: Fraction of events included in each bin in data (642 441 total events) and MC (200 028 total events) for 2011 direct photon events with $-\pi < \phi < -\frac{\pi}{2}$.

	$P_T \in [30,45]$(GeV)		$P_T \in [45,70]$(GeV)		$P_T \in [70,\infty]$(GeV)	
η Bin	$\frac{\chi^2}{NDF}$	$< \frac{\chi^2}{NDF} >$	$\frac{\chi^2}{NDF}$	$< \frac{\chi^2}{NDF} >$	$\frac{\chi^2}{NDF}$	$< \frac{\chi^2}{NDF} >$
$[-3.2,-1.7]$	$\frac{117}{30}$	$\frac{92.9\pm11.3}{38.9}$	$\frac{200}{42}$	$\frac{95.6\pm16.5}{54.9}$	$\frac{128}{48}$	$\frac{92\pm27.6}{52.7}$
$[-1.7,-1.0]$	$\frac{120}{30}$	$\frac{102\pm10.9}{40.6}$	$\frac{154}{45}$	$\frac{110\pm14.8}{57.9}$	$\frac{130}{48}$	$\frac{78.5\pm16}{58.2}$
$[-1.0,0.0]$	$\frac{184}{31}$	$\frac{188\pm15.4}{42.3}$	$\frac{297}{48}$	$\frac{166\pm17.4}{63.3}$	$\frac{191}{55}$	$\frac{90.9\pm12.1}{62.6}$
$[0.0,1.0]$	$\frac{197}{32}$	$\frac{166\pm14}{43.1}$	$\frac{367}{48}$	$\frac{155\pm16.9}{63}$	$\frac{192}{60}$	$\frac{115\pm26}{63.1}$
$[1.0,1.7]$	$\frac{126}{31}$	$\frac{102\pm11.2}{40.5}$	$\frac{185}{46}$	$\frac{115\pm14.9}{58.2}$	$\frac{143}{47}$	$\frac{96.2\pm24.4}{56.9}$
$[1.7,3.2]$	$\frac{83}{31}$	$\frac{80.1\pm11.2}{39}$	$\frac{197}{45}$	$\frac{90.2\pm15.2}{56.3}$	$\frac{118}{44}$	$\frac{199\pm43.3}{54.4}$

Table 7.7: χ^2/NDF comparing data to the MC and $< \chi^2/NDF >$ with standard deviation comparing the data to the corrected MC for 2011 direct photon events with $-\frac{\pi}{2} < \phi < 0$.

	$P_T \in [30,45]$(GeV)		$P_T \in [45,70]$(GeV)		$P_T \in [70,\infty]$(GeV)	
η Bin	Data	MC	Data	MC	Data	MC
$[-3.2,-1.7]$	0.0121	0.0135	0.00943	0.00639	0.00237	0.00156
$[-1.7,-1.0]$	0.0148	0.0189	0.0133	0.0101	0.00315	0.00255
$[-1.0,0.0]$	0.0267	0.0383	0.0271	0.0225	0.00887	0.00721
$[0.0,1.0]$	0.0275	0.0378	0.0286	0.0232	0.00906	0.00713
$[1.0,1.7]$	0.0154	0.0194	0.0136	0.0107	0.00318	0.00243
$[1.7,3.2]$	0.012	0.0142	0.00984	0.00652	0.00232	0.00161

Table 7.8: Fraction of events included in each bin in data (642 441 total events) and MC (200 028 total events) for 2011 direct photon events with $-\frac{\pi}{2} < \phi < 0$.

	$P_T \in [30,45]$(GeV)		$P_T \in [45,70]$(GeV)		$P_T \in [70,\infty]$(GeV)	
η Bin	$\frac{\chi^2}{NDF}$	$< \frac{\chi^2}{NDF} >$	$\frac{\chi^2}{NDF}$	$< \frac{\chi^2}{NDF} >$	$\frac{\chi^2}{NDF}$	$< \frac{\chi^2}{NDF} >$
$[-3.2,-1.7]$	$\frac{97.4}{32}$	$\frac{81.1\pm11}{40}$	$\frac{127}{44}$	$\frac{96.9\pm16.3}{54.2}$	$\frac{130}{47}$	$\frac{160\pm47.1}{55.6}$
$[-1.7,-1.0]$	$\frac{106}{31}$	$\frac{101\pm10.8}{40}$	$\frac{186}{44}$	$\frac{109\pm14.2}{57}$	$\frac{123}{50}$	$\frac{204\pm47.5}{59.5}$
$[-1.0,0.0]$	$\frac{145}{32}$	$\frac{182\pm14.8}{42.6}$	$\frac{310}{48}$	$\frac{155\pm16.5}{63.8}$	$\frac{177}{56}$	$\frac{118\pm27.2}{62.9}$
$[0.0,1.0]$	$\frac{159}{32}$	$\frac{185\pm15.1}{42.5}$	$\frac{267}{50}$	$\frac{166\pm17}{64.5}$	$\frac{183}{57}$	$\frac{166\pm34.2}{63.7}$
$[1.0,1.7]$	$\frac{116}{31}$	$\frac{99.1\pm10.9}{40.9}$	$\frac{171}{45}$	$\frac{108\pm14.5}{59.3}$	$\frac{163}{51}$	$\frac{173\pm43.7}{60.5}$
$[1.7,3.2]$	$\frac{79.6}{30}$	$\frac{91.2\pm10.7}{39.8}$	$\frac{181}{47}$	$\frac{86.9\pm16.5}{55.3}$	$\frac{174}{49}$	$\frac{117\pm32.8}{57}$

Table 7.9: χ^2/NDF comparing data to the MC and $< \chi^2/NDF >$ with standard deviation comparing the data to the corrected MC for 2011 direct photon events with $0 < \phi < \frac{\pi}{2}$.

	$P_T \in [30,45]$(GeV)		$P_T \in [45,70]$(GeV)		$P_T \in [70,\infty]$(GeV)	
η Bin	Data	MC	Data	MC	Data	MC
$[-3.2,-1.7]$	0.012	0.0137	0.00964	0.00624	0.00251	0.00161
$[-1.7,-1.0]$	0.0147	0.0185	0.0129	0.00986	0.00318	0.00226
$[-1.0,0.0]$	0.0268	0.0369	0.027	0.0225	0.00873	0.00685
$[0.0,1.0]$	0.0261	0.0356	0.0276	0.0227	0.0091	0.00696
$[1.0,1.7]$	0.0145	0.019	0.0132	0.01	0.00315	0.00251
$[1.7,3.2]$	0.0122	0.0146	0.00982	0.00601	0.00249	0.00178

Table 7.10: Fraction of events included in each bin in data (642 441 total events) and MC (200 028 total events) for 2011 direct photon events with $0 < \phi < \frac{\pi}{2}$.

	$P_T \in [30,45]$(GeV)		$P_T \in [45,70]$(GeV)		$P_T \in [70,\infty]$(GeV)	
η Bin	$\frac{\chi^2}{NDF}$	$< \frac{\chi^2}{NDF} >$	$\frac{\chi^2}{NDF}$	$< \frac{\chi^2}{NDF} >$	$\frac{\chi^2}{NDF}$	$< \frac{\chi^2}{NDF} >$
$[-3.2,-1.7]$	$\frac{71.9}{31}$	$\frac{112\pm12.2}{40.3}$	$\frac{166}{45}$	$\frac{102\pm17.1}{57.6}$	$\frac{118}{44}$	$\frac{121\pm29.6}{53.3}$
$[-1.7,-1.0]$	$\frac{140}{32}$	$\frac{98.5\pm11.6}{41.8}$	$\frac{204}{48}$	$\frac{113\pm14.9}{60.4}$	$\frac{177}{49}$	$\frac{139\pm33.4}{58.4}$
$[-1.0,0.0]$	$\frac{174}{31}$	$\frac{189\pm14.5}{42.7}$	$\frac{395}{50}$	$\frac{160\pm16.3}{64}$	$\frac{219}{55}$	$\frac{117\pm20.6}{63.3}$
$[0.0,1.0]$	$\frac{158}{32}$	$\frac{188\pm16.5}{42.8}$	$\frac{317}{48}$	$\frac{174\pm18.3}{64.2}$	$\frac{197}{55}$	$\frac{107\pm15.7}{64.3}$
$[1.0,1.7]$	$\frac{104}{31}$	$\frac{113\pm12.7}{40.9}$	$\frac{204}{44}$	$\frac{108\pm15.7}{59.3}$	$\frac{127}{50}$	$\frac{152\pm35.4}{60.3}$
$[1.7,3.2]$	$\frac{134}{32}$	$\frac{92.4\pm11.5}{40}$	$\frac{207}{46}$	$\frac{100\pm16.9}{56.8}$	$\frac{136}{50}$	$\frac{145\pm27.4}{58.8}$

Table 7.11: χ^2/NDF comparing data to the MC and $< \chi^2/NDF >$ with standard deviation comparing the data to the corrected MC for 2011 direct photon events with $\frac{\pi}{2} < \phi < \pi$.

	$P_T \in [30,45]$(GeV)		$P_T \in [45,70]$(GeV)		$P_T \in [70,\infty]$(GeV)	
η Bin	Data	MC	Data	MC	Data	MC
$[-3.2,-1.7]$	0.0134	0.0153	0.0104	0.00683	0.0026	0.00162
$[-1.7,-1.0]$	0.0167	0.0203	0.0142	0.011	0.00348	0.00241
$[-1.0,0.0]$	0.0299	0.04	0.0296	0.0241	0.00961	0.00727
$[0.0,1.0]$	0.029	0.0387	0.0303	0.0239	0.00969	0.00723
$[1.0,1.7]$	0.0164	0.0202	0.0146	0.01	0.00342	0.00275
$[1.7,3.2]$	0.0136	0.0148	0.0108	0.00674	0.00272	0.00167

Table 7.12: Fraction of events included in each bin in data (642 441 total events) and MC (200 028 total events) for 2011 direct photon events with $\frac{\pi}{2} < \phi < \pi$.

η Bin	Data	MC
$-4.9 < \eta < -3.2$	0.00138	0.0008
$3.2 < \eta < 4.9$	0.00133	0.00092

Table 7.13: Fraction of events included in each bin in data (642 441 total events) and MC (200 028 total events) for 2011 direct photon events in the forward calorimeters.

It is interesting to note that the MC has a larger fraction of events for the lower P_T bins compared to the data than for the higher P_T bins. Since we are looking at the resolution, the absolute number of events should not have a direct effect on the results calculated in this thesis.

There are some common features and some outliers seen in the preceding tables. The number of bins included in the χ^2 calculation always increases from the MC to the corrected MC. This is evident in the difference in the number of degrees of freedom between the MC and the corrected MC. This is shown more clearly in figure 7.22. The increase in the width seen in the corrected MC was expected to occur due to the smearing.

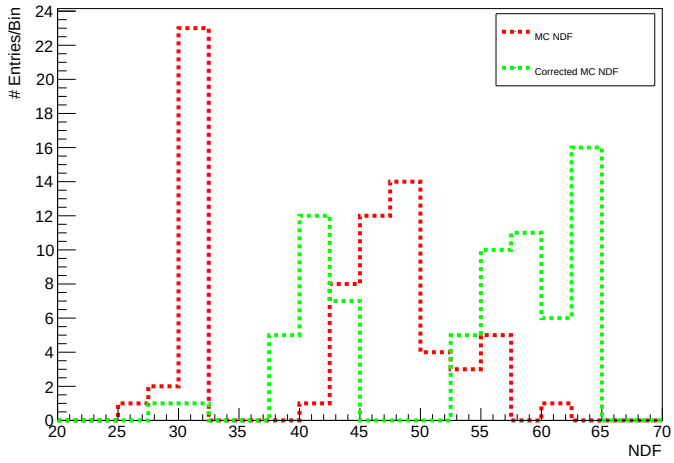

Figure 7.22: NDF values from comparing the MC to the data (red) and the corrected MC to the data (green) in all jet bins for 2011 direct photon events.

With a few exceptions, the χ^2 value gets smaller from the MC to the corrected MC. Together with the increase in the number of degrees of freedom, this results in an improvement to the χ^2/NDF in all but the five bins given in table 7.14. For the high P_T bins, this can be understood as a result of having few entries in these bins. Having few entries can exaggerate outliers especially in the smearing process. For the low energy bins these non-improvements are the result mainly of the behavior near the peak around $Z = 0$. Since these bins are being tested to a high precision (because they have many entries), the over smoothing of the peak causes the correction to mis-represent the data there by a wide margin. This can be seen in the difference plots in Appendix B, the plots in question are the top left plot in figure B.11 and the middle left plot in figure B.2 .

MC $\frac{\chi^2}{NDF}$	Corrected $<\frac{\chi^2}{NDF}>$	η Bin	ϕ Bin	P_T Bin
2.77	2.88±0.846	$[-3.2,-1.7]$	$[0,\frac{\pi}{2}]$	$[70,\infty]$(GeV)
2.32	2.77±0.304	$[-3.2,-1.7]$	$[\frac{\pi}{2},\pi]$	$[30,45]$(GeV)
2.46	3.43±0.799	$[-1.7,-1.0]$	$[0,\frac{\pi}{2}]$	$[70,\infty]$(GeV)
3.82	4.68±0.376	$[-1.0,0.0]$	$[-\pi,-\frac{\pi}{2}]$	$[30,45]$(GeV)
2.68	3.67±0.796	$[1.7,3.2]$	$[-\frac{\pi}{2},0]$	$[70,\infty]$(GeV)

Table 7.14: Bins where $\chi^2/NDF << \chi^2/NDF >$ in 2011 direct photon events.

Recall that for each bin the one thousand smeared MC distributions are created and compared to the data and the standard deviation shows the width of the χ^2 between these one thousand comparisons. If the standard deviation is large then the smeared MC behaves quite differently from one instance of smearing to the next, this situation would be expected in bins with a low number of data points.

There are eighteen bins where the standard deviation is larger than twenty percent of the χ^2 value, these are shown in table 7.15. It is clear that the standard deviation is above 20% only in the highest P_T bins. This is expected because these bins have the fewest number of events and there is more likely to be entries for which smearing can drastically change the result. In most of these cases the corrected MC describes the data better within the error given by the standard deviation.

MC $\frac{\chi^2}{NDF}$	Corrected $<\frac{\chi^2}{NDF}>$	$\frac{\sigma_{\chi^2}}{\chi^2}$	η Bin	ϕ Bin	P_T Bin
2.51	2.04±0.44	0.215	$[-3.2,-1.7]$	$[-\pi,-\frac{\pi}{2}]$	$[70,\infty]$(GeV)
2.67	1.75±0.524	0.3	$[-3.2,-1.7]$	$[-\frac{\pi}{2},0]$	$[70,\infty]$(GeV)
2.77	2.88±0.846	0.294	$[-3.2,-1.7]$	$[0,\frac{\pi}{2}]$	$[70,\infty]$(GeV)
2.67	2.27±0.556	0.245	$[-3.2,-1.7]$	$[\frac{\pi}{2},\pi]$	$[70,\infty]$(GeV)
2.77	1.83±0.425	0.233	$[-1.7,-1.0]$	$[-\pi,-\frac{\pi}{2}]$	$[70,\infty]$(GeV)
2.7	1.35±0.275	0.204	$[-1.7,-1.0]$	$[-\frac{\pi}{2},0]$	$[70,\infty]$(GeV)
2.46	3.43±0.799	0.233	$[-1.7,-1.0]$	$[0,\frac{\pi}{2}]$	$[70,\infty]$(GeV)
3.61	2.38±0.572	0.24	$[-1.7,-1.0]$	$[\frac{\pi}{2},\pi]$	$[70,\infty]$(GeV)
4.06	2.25±0.545	0.242	$[-1.0,0.0]$	$[-\pi,-\frac{\pi}{2}]$	$[70,\infty]$(GeV)
3.15	1.87±0.432	0.231	$[-1.0,0.0]$	$[0,\frac{\pi}{2}]$	$[70,\infty]$(GeV)
3.21	1.83±0.412	0.225	$[0.0,1.0]$	$[-\frac{\pi}{2},0]$	$[70,\infty]$(GeV)
3.2	2.6±0.537	0.207	$[0.0,1.0]$	$[0,\frac{\pi}{2}]$	$[70,\infty]$(GeV)
2.91	2.41±0.574	0.238	$[1.0,1.7]$	$[-\pi,-\frac{\pi}{2}]$	$[70,\infty]$(GeV)
3.03	1.69±0.428	0.253	$[1.0,1.7]$	$[-\frac{\pi}{2},0]$	$[70,\infty]$(GeV)
3.19	2.87±0.722	0.252	$[1.0,1.7]$	$[0,\frac{\pi}{2}]$	$[70,\infty]$(GeV)
2.54	2.52±0.586	0.233	$[1.0,1.7]$	$[\frac{\pi}{2},\pi]$	$[70,\infty]$(GeV)
2.68	3.67±0.796	0.217	$[1.7,3.2]$	$[-\frac{\pi}{2},0]$	$[70,\infty]$(GeV)
3.55	2.05±0.575	0.28	$[1.7,3.2]$	$[0,\frac{\pi}{2}]$	$[70,\infty]$(GeV)

Table 7.15: Bins where $\frac{\sigma_{\chi^2}}{\chi^2} > 0.2$ in 2011 direct photon events.

Chapter 8

Conclusions

This thesis expands on the work done by Dr. Lorraine Courneyea in her PhD thesis. The common idea is to find a way to correct for mis-modeled jet energy resolution by producing a smearing correction. In this thesis, the method is applied to a larger data set with a unique unfolding method and test statistic of the MC correction. Based on the results contained within this body of work, this method has been shown to be effective at improving the agreement between the data and the MC simulations of 2011 direct photon events produced within the ATLAS detector.

Events containing a photon energetically balanced with a jet were studied. Due to the superior energy resolution of the photon in the electromagnetic calorimeter, these events allow for a meaningful way to measure the jet energy resolution. A variable based on the difference in the transverse momentum of the jet and the photon has been used to quantify the jet energy resolution. This variable is explored in different kinematic regions. A correction to the jet energy resolution is produced in each kinematic region by unfolding the distribution of the resolution variable in the MC sample from that in the data using an iterative unfolding method based on Bayes' theorem. This correction is then applied to the jets in the MC by smearing the MC jet

P_T. In order to determine the effectiveness of randomly smearing from one instance to another, this smearing is done multiple times and the mean of the results is used in comparisons. The MC and the corrected MC are compared to the data in each kinematic region by using a form of Pearson's χ^2 test.

This method has been shown to produce a result that is satisfactory. There is an improvement in the χ^2/NDF in all but 5% of the selected kinematic bins, and the standard deviation of the average χ^2, which is a measure of how precisely the smearing function is known, is sufficiently low such that the smearing can be used without significantly increasing the errors on the MC distribution. These results are quite promising and show that this method may be useful.

Limitations to this method are mostly caused by having bins with a limited number of MC events. This can be remedied in two ways. Theoretically one could just produce more MC; although this can be resource intensive, and many researchers would probably not want to carry out this solution. Otherwise, one could loosen up the kinematic binning choice. For example, the difference in the behaviour between the ϕ bins is minimal and one may consider in the future excluding ϕ binning unless it is suspected that a specific region in ϕ is behaving differently between the data and the MC.

Mis-identifying direct photon events may cause this method to not be a completely accurate measure of the jet energy resolution. The leading background to these events is a charged quark radiating a photon, which is a difficult background to eliminate. These types of events can be partially accounted for by utilizing a photon isolation cut, which has not been done in this work but is done elsewhere such as in [9].

Appendix A

Additional Information

A.1 ATLAS Coordinate System

A right-handed Cartesian coordinate system is used in ATLAS. Coordinates are defined so that x points towards the middle of the LHC ring, y points upwards, and z points down the beam pipe. It is more useful to define a coordinate system using semi-cylindrical coordinates z, ϕ, and η. The angle ϕ is in the x-y plane. The pseudorapidity η is defined in terms of the polar angle θ measured from the z axis, $\eta = -ln(tan(\frac{\theta}{2}))$.

A.2 Smearing and Unfolding

A measurement, x, of some variable, y, is affected by the detector's resolution. The measured probability distribution of x is the convolution of the true distribution of y with the detector resolution:

$$f_{meas}(x) = \int R(x-y) f_{true}(y) dy \tag{A.1}$$

When dealing with binned distributions, the integral becomes a sum over the bins of the true distribution, μ_j, and the detector resolution distribution R_{i-j}:

$$\nu_i = \sum_{j}^{allbins} R_{i-j}\mu_j \tag{A.2}$$

The components of equation A.2 can be described as follows:

- ν_i are the expected number of events in each bin of the measured distribution
- μ_j are the expected number of events in each bin of the true distribution
- R_{i-j} is the conditional probability P(observed in bin i|true value in bin j)

When the detector resolution can be determined independently of the experiment, one can produce a MC simulation of the detector effects on the true value to compare to the measured distribution. The resolution distribution becomes a matrix mapping the true value to the measured value, and the convolution equation can be written as a matrix multiplication.

$$\nu_i = \sum_{j}^{allbins} R_{ij}\mu_j \tag{A.3}$$

When comparing the results of two different experiments measuring the same quantity, it is better to compare the true distributions. Unfolding is an attempt to retrieve the true distribution based on the measured distribution and the detector resolution[12, 11, 13].

Unfolding is not a trivial problem for statistical data. When the measured distribution is also subject to statistical fluctuations, one can not simply find the inverse matrix and apply it to the measured distribution to achieve the true distribution. This can lead to huge variances in the results. Despite the large variances, the matrix inversion method would provide an unbiased estimate of the true distribution. In

order to reduce the variances, bias must be introduced. All unfolding methods must introduce some bias in order to produce results with useful levels of certainty [11].

A.3 Iterative Bayesian Unfolding

The iterative method [14] begins with a uniform distribution as an initial estimator of the truth distribution, $\hat{\mu}^o$. Each iteration updates the estimators based on the resolution matrix, and the previous estimators.

$$\hat{\mu}_i = \frac{1}{\epsilon_i} \sum_j^{allbins} P(true\_value\_in\_bin\_i | found\_in\_bin\_j) n_j \tag{A.4}$$

$$\epsilon_i \equiv \sum_j^{allbins} R_{ij} \tag{A.5}$$

This method uses Bayes' theorem to relate one conditional probability to another. The probability in equation A.4 can be related to the resolution matrix, $P(found\_in\_bin\_i | true\_value\_in\_bin\_j) = R_{ij}$, and the normalized prior estimators, p_i:

$$P(true\_value\_in\_bin\_i | found\_in\_bin\_j) = \frac{R_{ij} p_i}{\sum_k^{allbins} R_{ij} p_i} \tag{A.6}$$

Using Bayes' theory from equation A.6 in the definition of the iteration, equation A.4 one gets:

$$\mu_i = \frac{1}{\epsilon_i} \sum_j^{allbins} \frac{R_{ij} p_j}{\sum_k^{allbins} R_{jk} p_k n_j} \tag{A.7}$$

After each iteration the new estimator is compared to the old estimator using a χ^2 to determine convergence. Iteration is stopped when the current iteration is sufficiently close to the previous iteration. Very few iterations are required.

A.4 Testing the Iterative Bayesian Unfolding

In this section the iterative bayesian unfolding method is demonstrated and tested by unfolding gaussian functions. Gaussian functions have been chosen because the convolution of two gaussians is another gaussian, where the new mean is the sum of the means of the convolved gaussians and the square of the new standard deviation is the sum of the squares of the standard deviations of the convolved gaussians. Because of this simple property of the convolution of gaussians, unfolding one gaussian from another can be solved analytically. The parameters for the gaussians used in this section are summed up in table A.1.

$$G_3(\mu_3, \sigma_3) = G_1(\mu_1, \sigma_1) \otimes G_2(\mu_2, \sigma_2) \tag{A.8}$$

$$\mu_3 = \mu_1 + \mu_2$$

$$\sigma_3^2 = \sigma_1^2 + \sigma_2^2$$

	μ	σ
G_1	0.3	0.03
G_2	-0.1	0.04
G_3	0.2	0.05

Table A.1: Parameters of the gaussian functions used to test the D'Agostini smearing method.

The implementation of the iterative bayesian method takes as input a resolution matrix in the form of a two dimensional histogram, and a histogram representing the distribution to be unfolded from. Since this is done in ROOT, the resolution matrix is in the form of a two dimensional histogram and the distribution is in the form of a

one dimensional histogram. Consider unfolding G_1 from G_3 in order to estimate G_2. The form of G_3 must be given as a histogram and the form of G_1 must be given as a two dimensional histogram. Filling the G_3 histogram is done by filling a histogram with random instances selected from the function G_3. For the G_1 histogram, first a histogram is filled by selecting random instances from the function G_1. The two dimensional histogram is created using $R_{ij} = R_{i-j}$, this is the result of comparing the resolution functions of equation A.2 and A.3. The histograms of G_1 and G_3 are displayed in figure A.1 and the matrix form of G_1 is displayed in figure A.2.

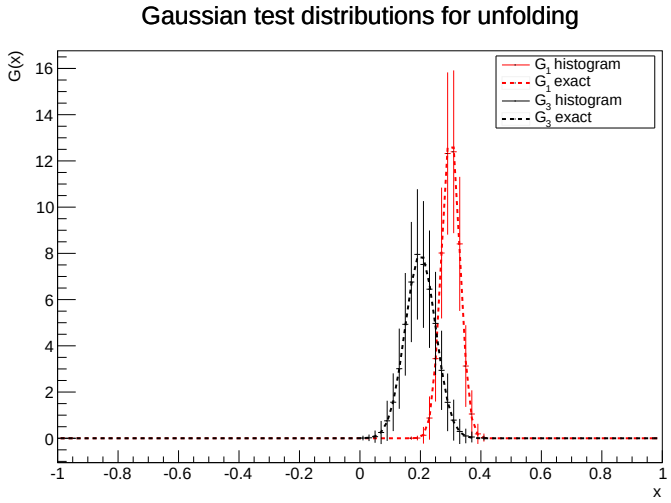

Figure A.1: G_1 and G_3 in histogram form, with their functions drawn on for comparison.

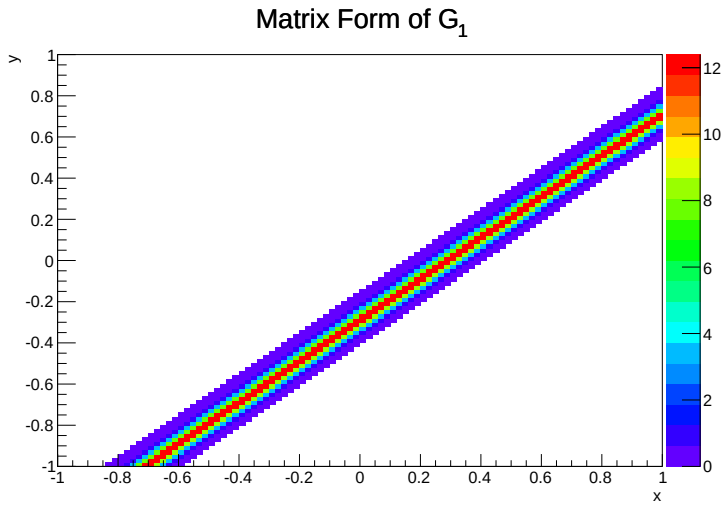

Figure A.2: G_1 in the form of a two dimensional histogram determined by $R_{ij} = R_{i-j}$.

Figures A.3, A.4, and A.5 show the results of unfolding using one, three, and nine iterations respectively. It is easy to see that this method converges to the desired value very quickly, within three iterations. At nine iterations the agreement has not improved, but the errors of the result have increased. The criteria for convergence to the correct unfolding result is to have the χ^2 from one iteration to the next be less than one, in most cases this occurs in about three iterations. Continuing the unfolding process after the result has already converged does not serve to improve upon the result.

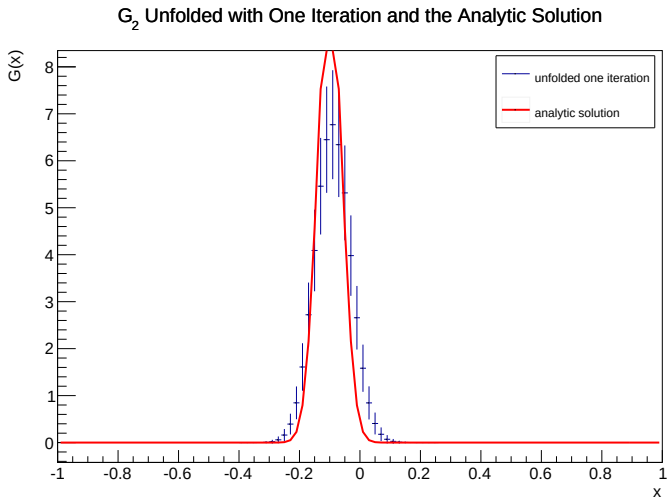

Figure A.3: The result of unfolding G_1 from G_3 using one iteration of the D'Agostini method compared to G_2.

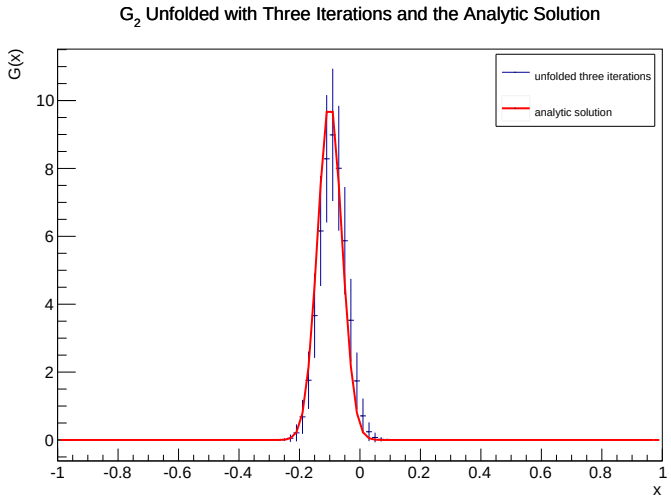

Figure A.4: The result of unfolding G_1 from G_3 using three iterations of the D'Agostini method compared to G_2.

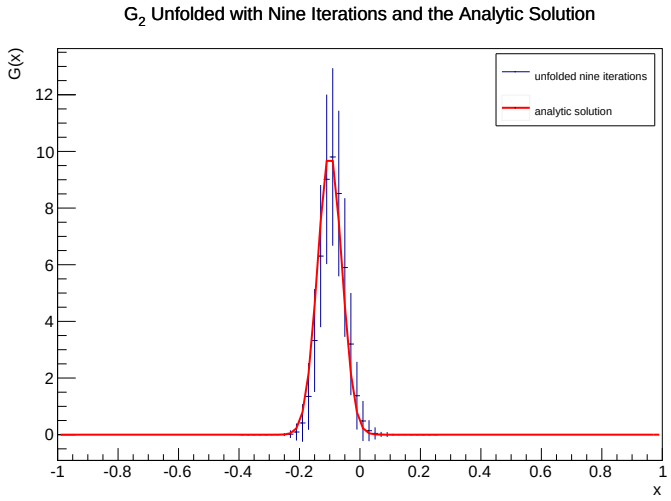

Figure A.5: The result of unfolding G_1 from G_3 using nine iterations of the D'Agostini method compared to G_2.

A.5 χ^2 Test

The χ^2 test statistic used in this thesis is a modified version of the standard χ^2 test that provides a measurement of the sum of the normalized squared deviations between two histograms. Equation A.9 shows how to calculate this test statistic [36]. In this equation two unweighted histograms are being compared each with r total bins. There are N total entries in the first histogram, with n_i entries in the i^{th} bin, and M total entries in the second histogram, with m_i entries in the i^{th} bin. In this case the number of degrees of freedom is the number of bins where there is at least one entry in either histogram. The χ^2 value that is calculated should fall on the χ^2 distribution (an incomplete gamma function) which provides a method for determining a p-value for comparing the two histograms.

$$\chi^2 = \sum_{i=1}^{r} \frac{(\sqrt{\frac{M}{N}} n_i - \sqrt{\frac{N}{M}} m_i)^2}{n_i + m_i} \tag{A.9}$$

In this thesis, the histograms that are being compared are weighted. This requires a different method for computing the χ^2 test statistic, this method is shown in equation A.10 [35]. This method does not give exactly the χ^2 distribution, however in reference [35] it is demonstrated that it should approximately follow a χ^2 distribution where again the number of degrees of freedom is the number of bins where there is at least one entry in either histogram.

$$\chi^2 = \sum_{i=1}^{r} \frac{(\frac{w_{1i}}{W_1} - \frac{w_{2i}}{W_2})^2}{\frac{s_{1i}^2}{W_1} + \frac{s_{2i}^2}{W_2}} \tag{A.10}$$

- r is the common number of bins of both histograms
- w_{ji} is the weighting for the i^{th} bin of histogram j
- $W_j = \sum_i w_{ji}$ is the total weight of events in histogram j
- s_{ji} is the bin error contained in the i^th bin (square root of the sum of the squares of the weight)

Appendix B

Additional Plots

This appendix chapter includes difference plots for each kinematic region that was studied in this thesis. There are a total of 74 different regions, which made this an unwieldy set of plots to include in the main body of this thesis. Each plot is a set of difference plots for the variable Z defined in equation (2.3). In red is the data minus the MC and in green is the data minus the mean of the corrected MC. For the data and the MC the errors that are included in these histograms are purely statistical, while for the corrected MC the errors in these histograms are the standard deviation of the mean of the multiple smearing instances used.

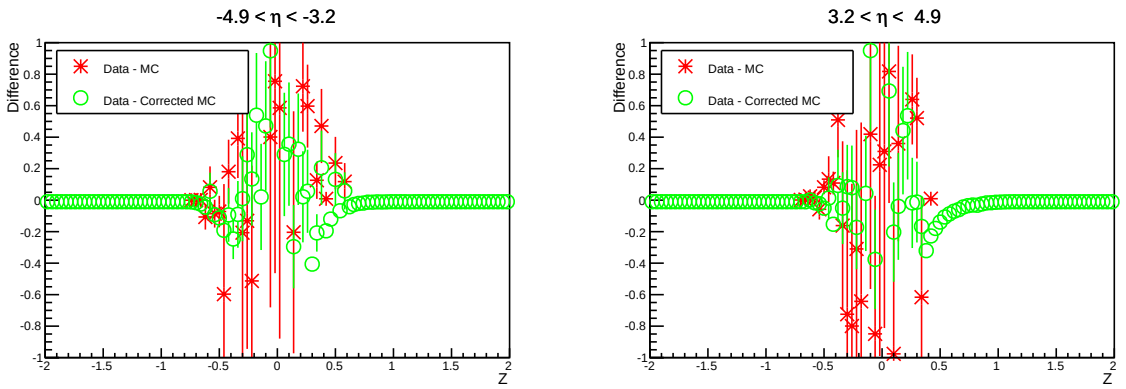

Figure B.1: Comparison of the differences in the Z distributions between the data and the MC (red), and the data and the corrected MC (green) in the forward calorimeter.

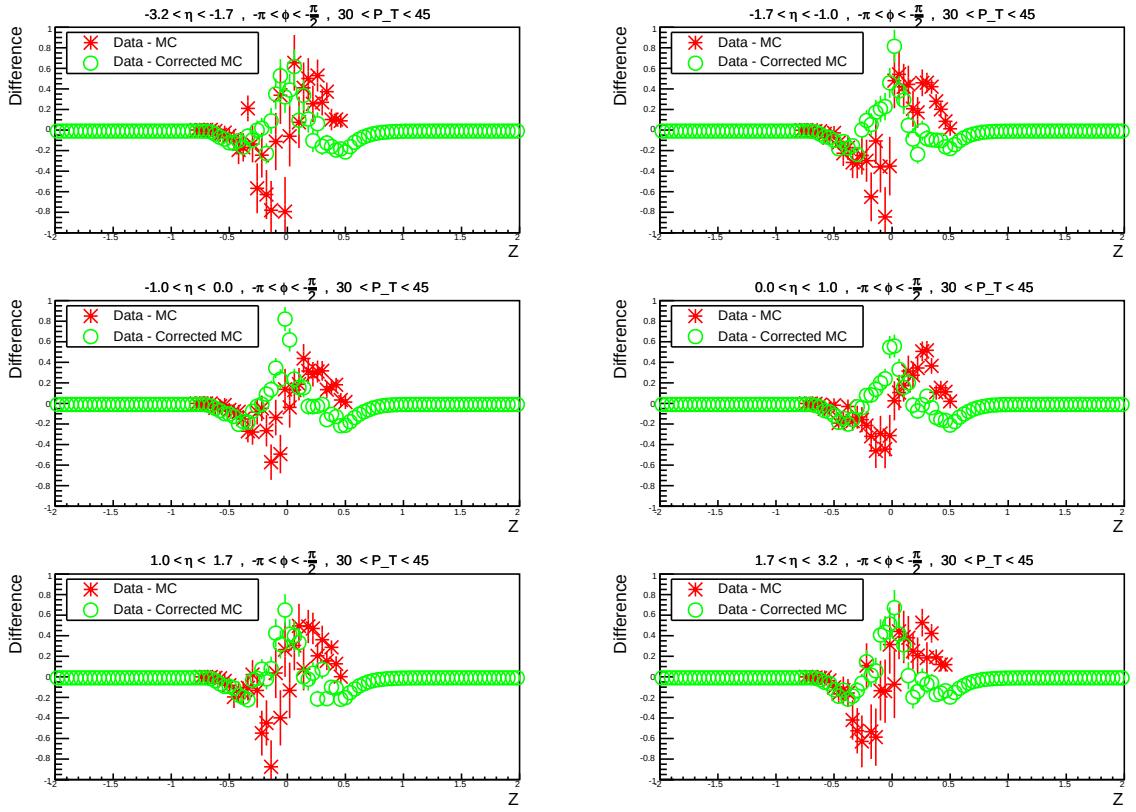

Figure B.2: Comparison of the differences in the Z distributions between the data and the MC (red), and the data and the corrected MC (green) for 30 GeV$< P_T^{jet} <$ 45 GeV and $-\pi < \phi < -\frac{\pi}{2}$.

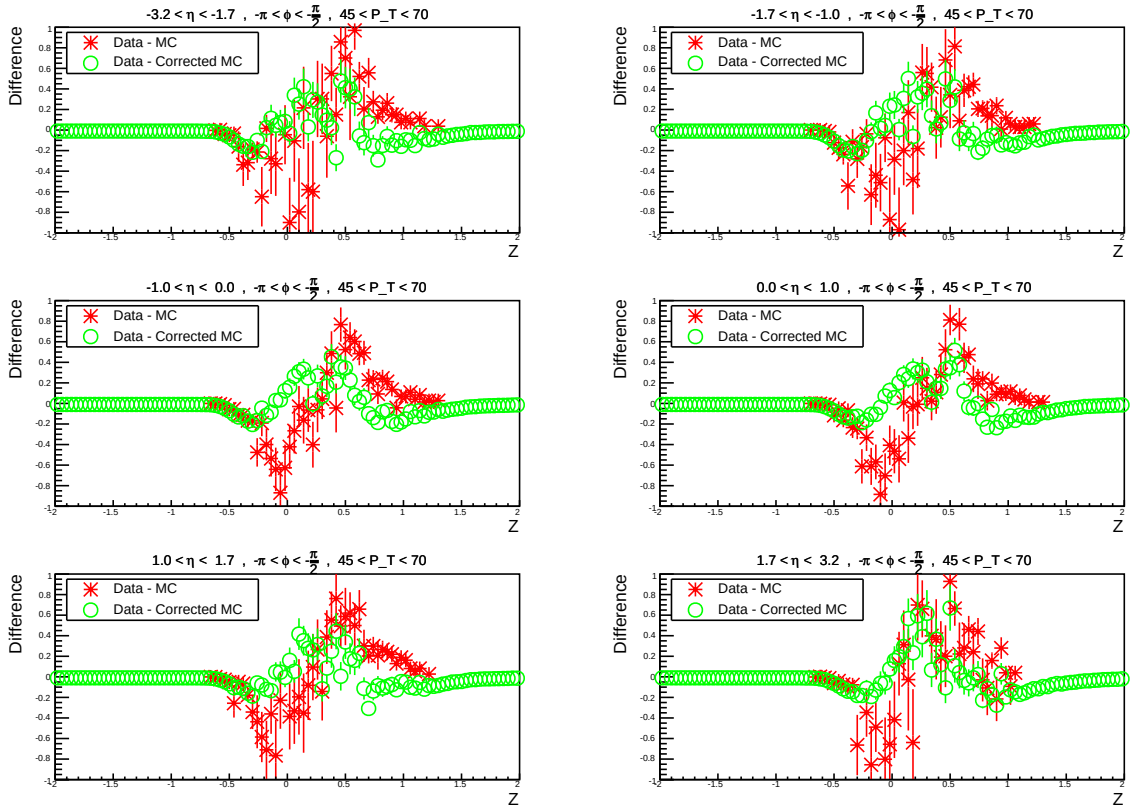

Figure B.3: Comparison of the differences in the Z distributions between the data and the MC (red), and the data and the corrected MC (green) for 45 GeV $< P_T^{jet} <$ 70 GeV and $-\pi < \phi < -\frac{\pi}{2}$.

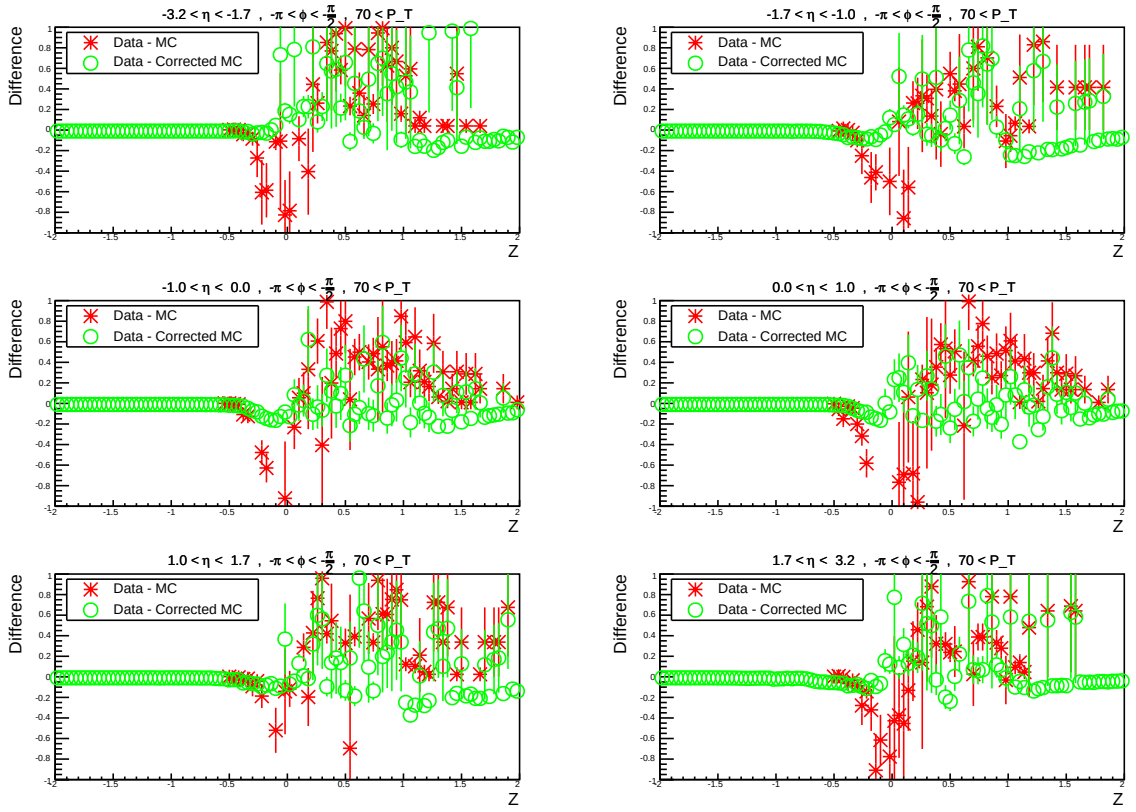

Figure B.4: Comparison of the differences in the Z distributions between the data and the MC (red), and the data and the corrected MC (green) for 70 GeV $< P_T^{jet}$ and $-\pi < \phi < -\frac{\pi}{2}$.

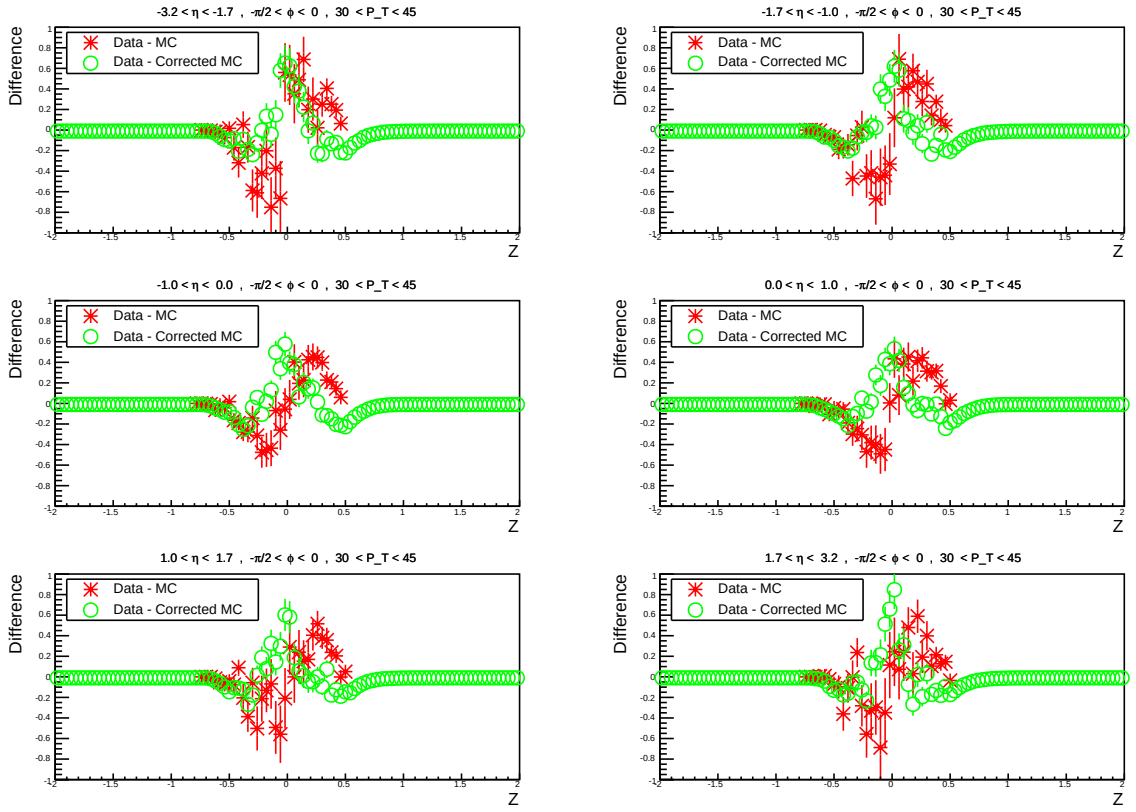

Figure B.5: Comparison of the differences in the Z distributions between the data and the MC (red), and the data and the corrected MC (green) for 30 GeV$< P_T^{jet} <$ 45 GeV and $-\frac{\pi}{2} < \phi < 0$.

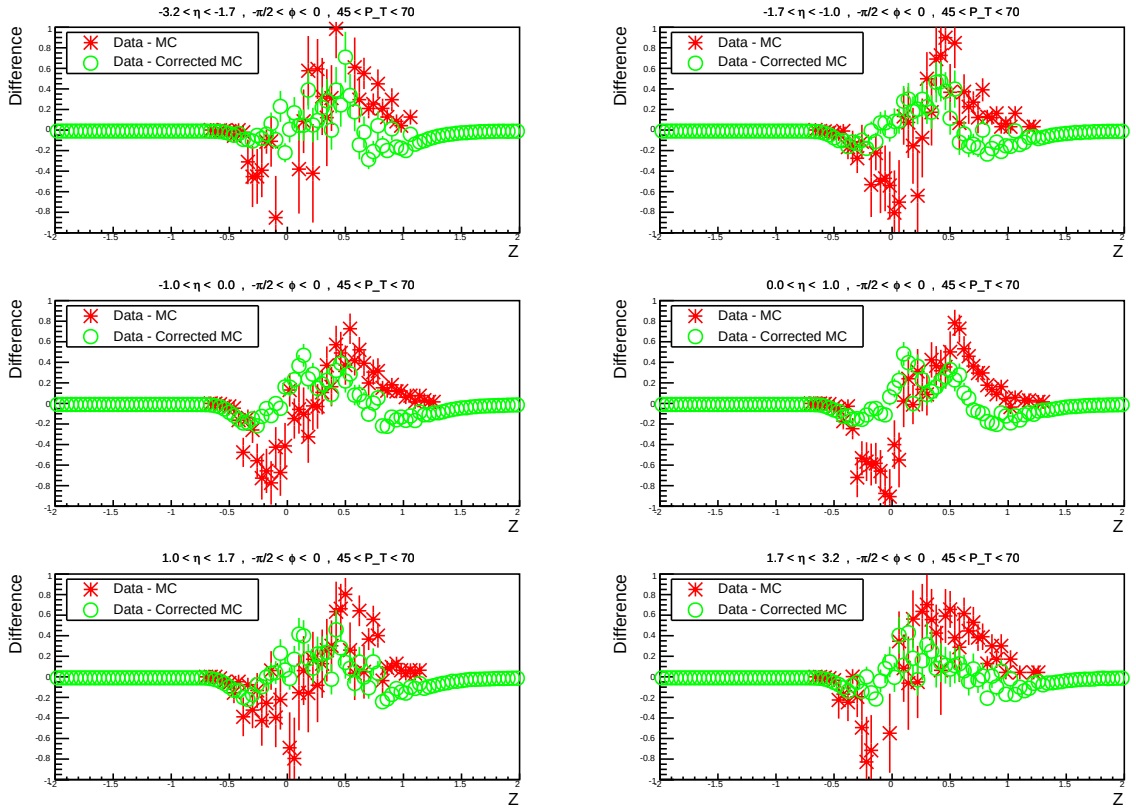

Figure B.6: Comparison of the differences in the Z distributions between the data and the MC (red), and the data and the corrected MC (green) for 45 GeV $< P_T^{jet} <$ 70 GeV and $-\frac{\pi}{2} < \phi < 0$.

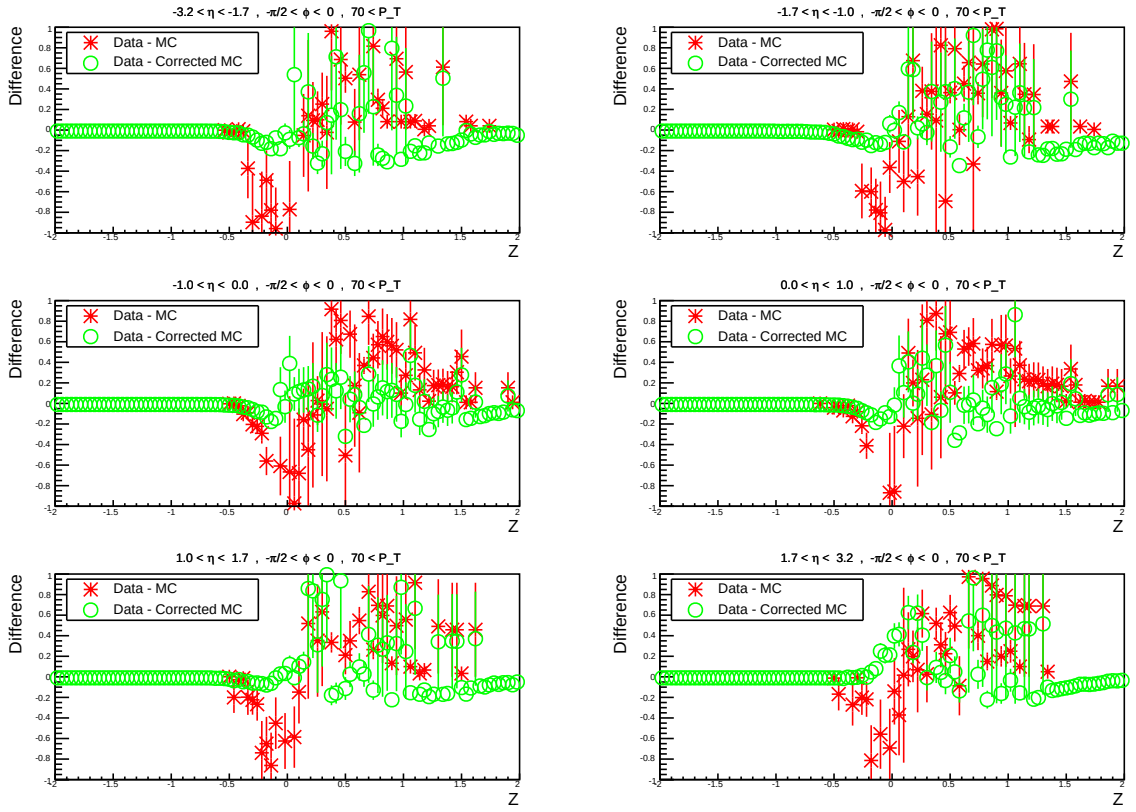

Figure B.7: Comparison of the differences in the Z distributions between the data and the MC (red), and the data and the corrected MC (green) for 70 GeV $< P_T^{jet}$ and $-\frac{\pi}{2} < \phi < 0$.

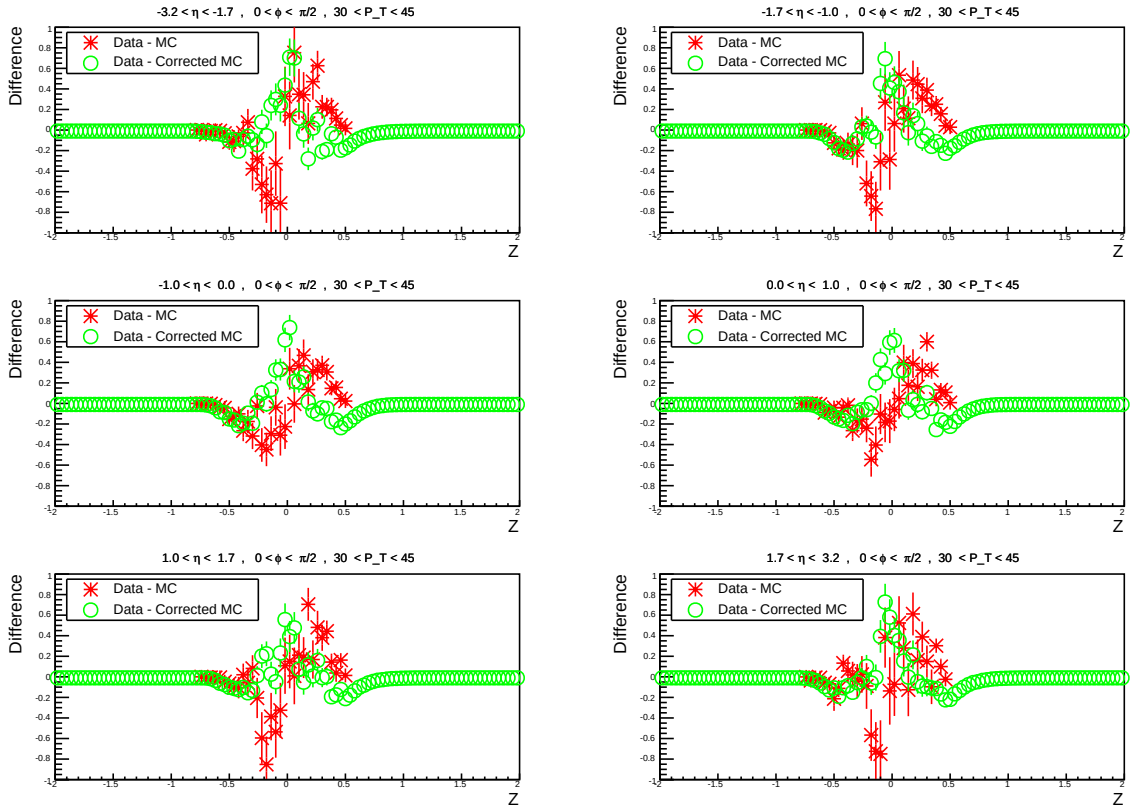

Figure B.8: Comparison of the differences in the Z distributions between the data and the MC (red), and the data and the corrected MC (green) for 30 GeV$< P_T^{jet} <$ 45 GeV and $0 < \phi < \frac{\pi}{2}$.

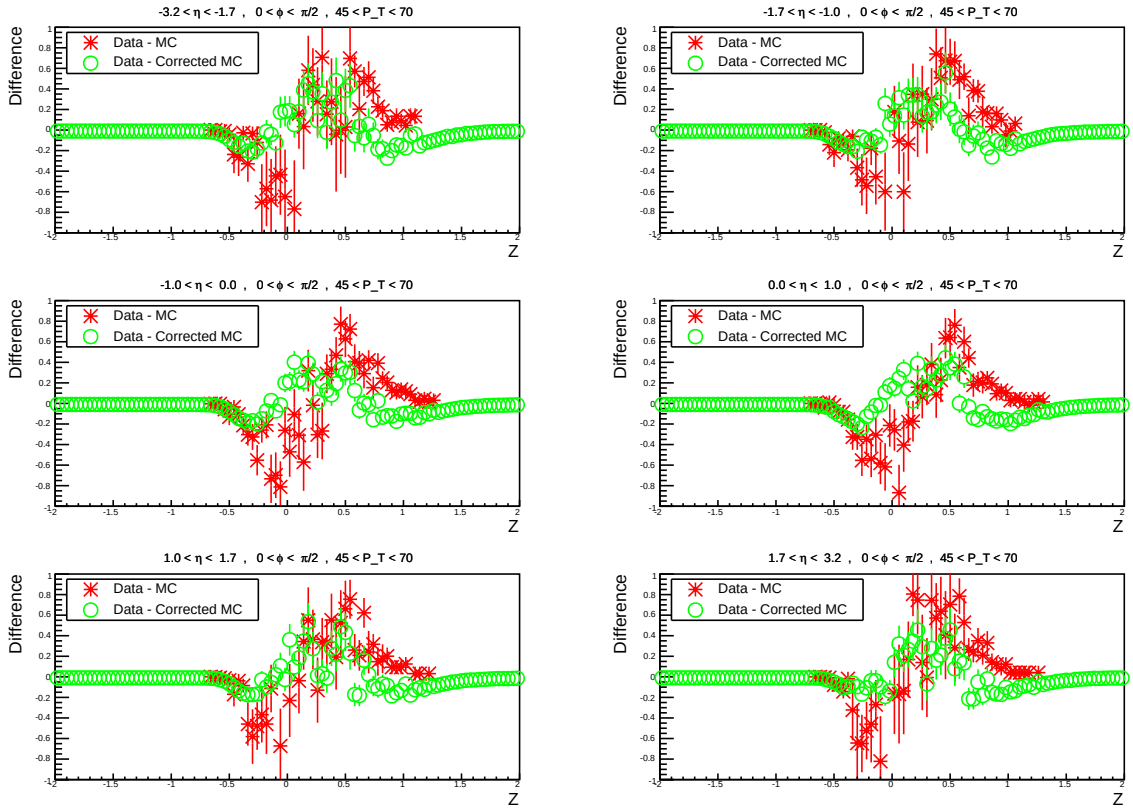

Figure B.9: Comparison of the differences in the Z distributions between the data and the MC (red), and the data and the corrected MC (green) for 45 GeV $< P_T^{jet} <$ 70 GeV and $0 < \phi < \frac{\pi}{2}$.

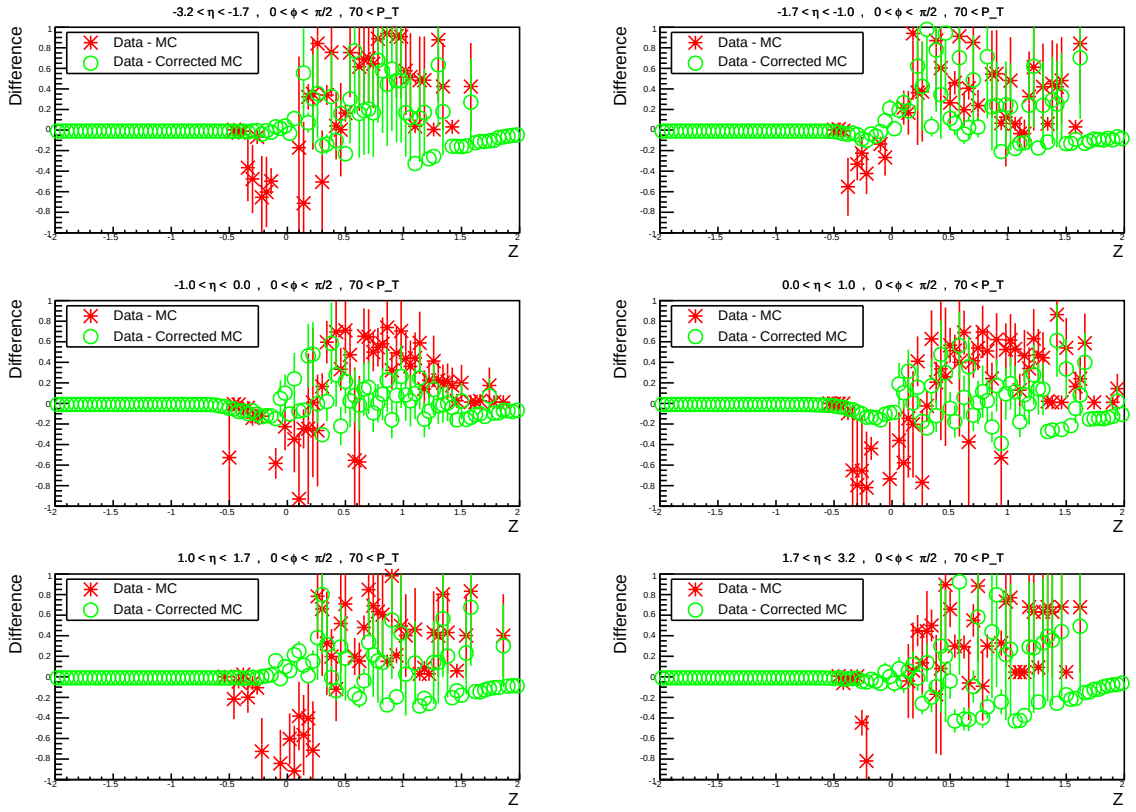

Figure B.10: Comparison of the differences in the Z distributions between the data and the MC (red), and the data and the corrected MC (green) for 70 GeV $< P_T^{jet}$ and $0 < \phi < \frac{\pi}{2}$.

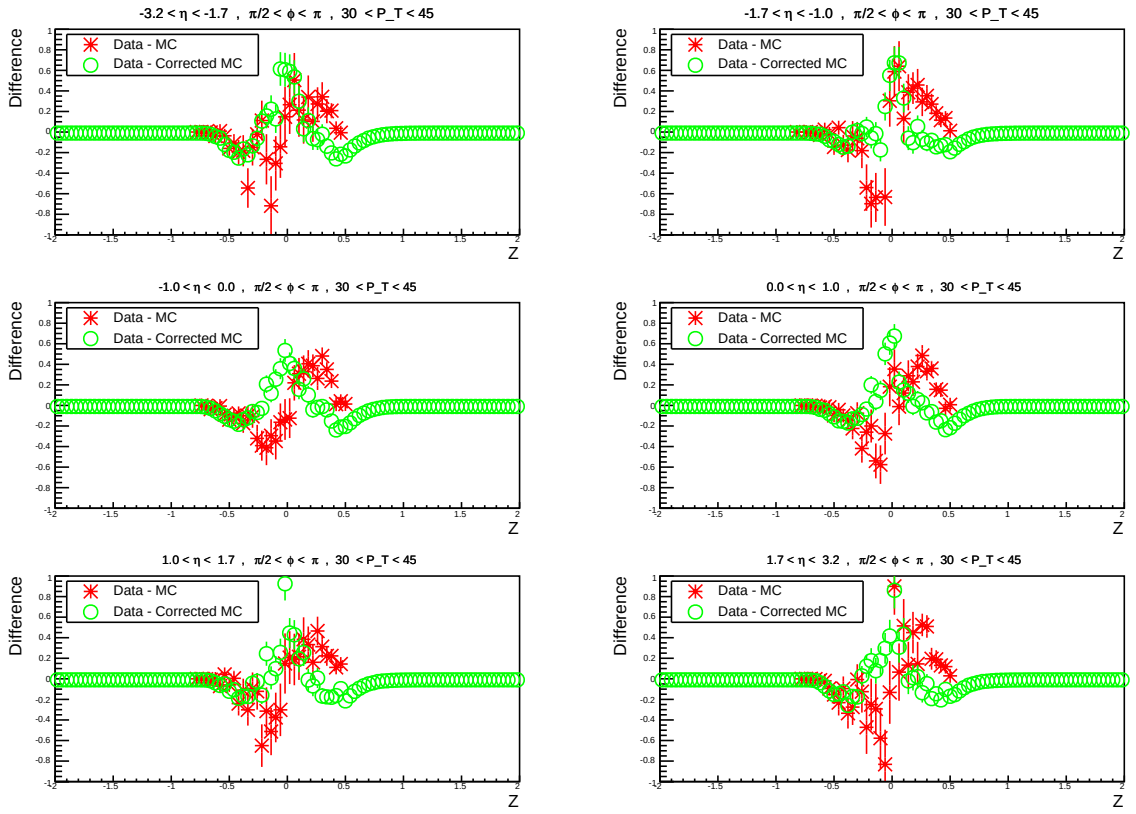

Figure B.11: Comparison of the differences in the Z distributions between the data and the MC (red), and the data and the corrected MC (green) for 30 GeV$< P_T^{jet} <$ 45 GeV and $\frac{\pi}{2} < \phi < \pi$.

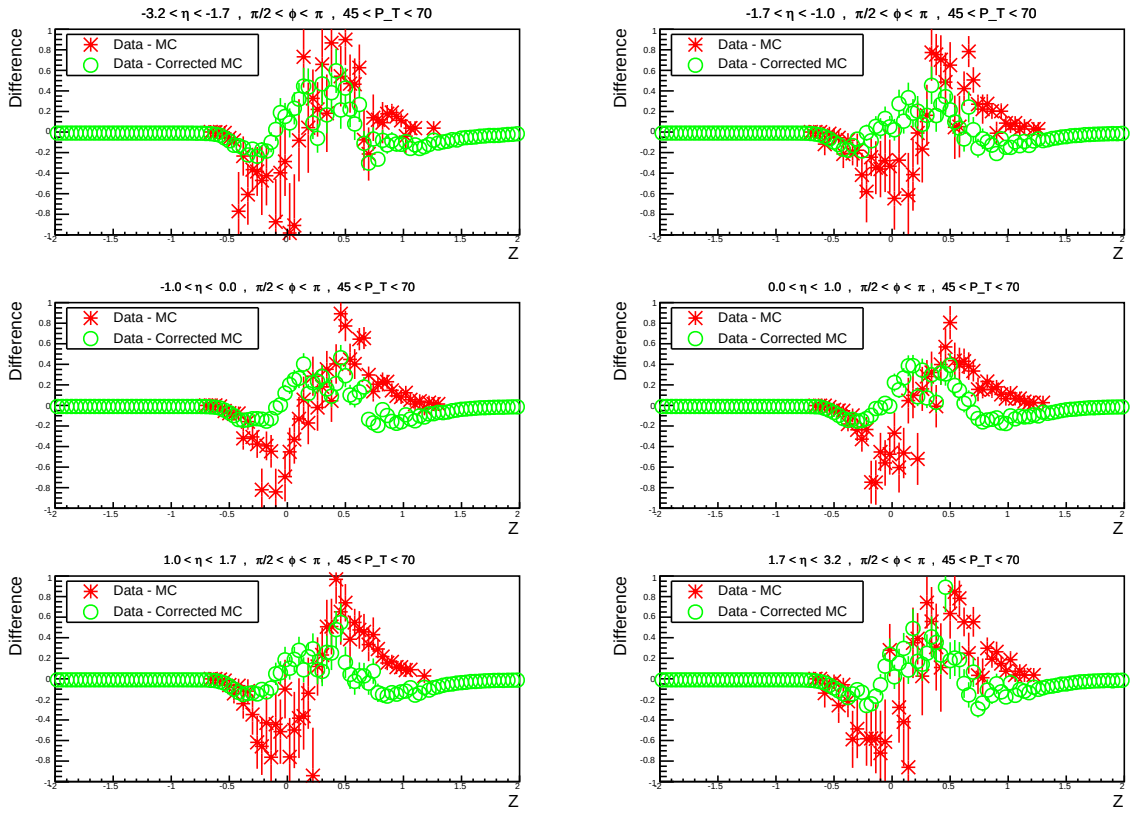

Figure B.12: Comparison of the differences in the Z distributions between the data and the MC (red), and the data and the corrected MC (green) for 45 GeV $< P_T^{jet} <$ 70 GeV and $\frac{\pi}{2} < \phi < \pi$.

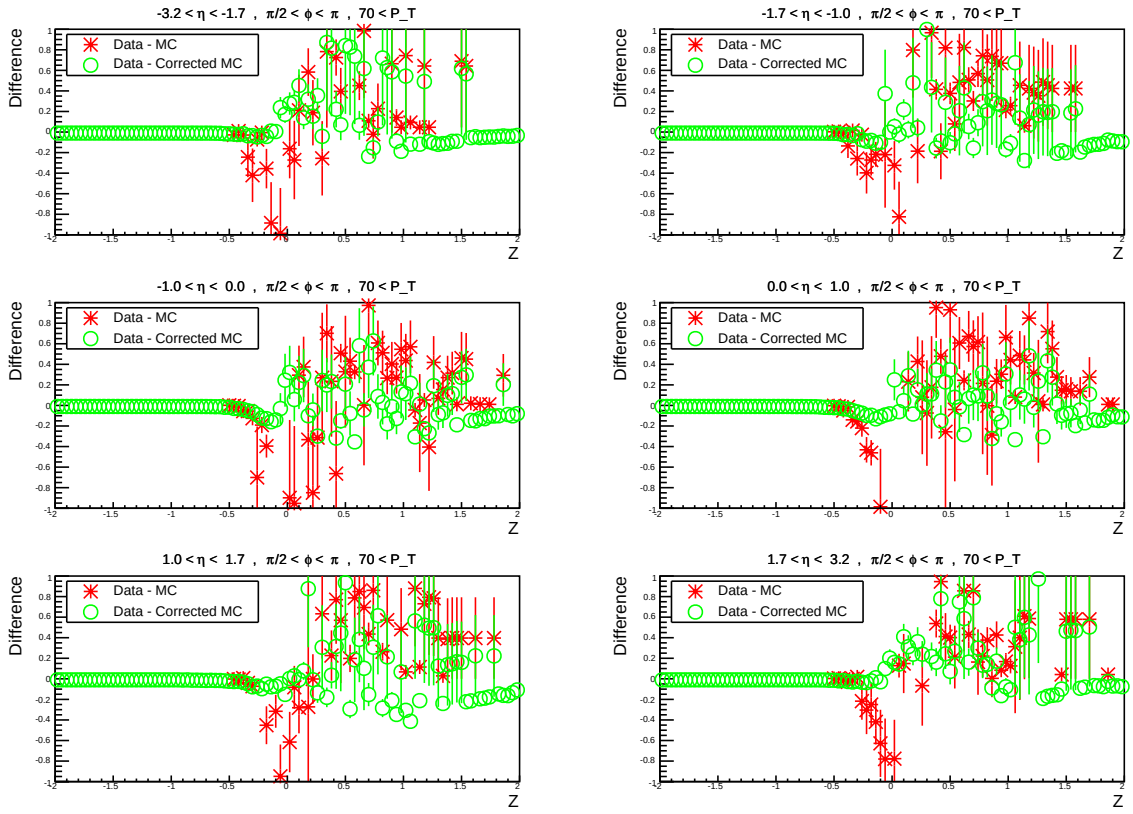

Figure B.13: Comparison of the differences in the Z distributions between the data and the MC (red), and the data and the corrected MC (green) for 70 GeV $< P_T^{jet}$ and $\frac{\pi}{2} < \phi < \pi$.

Bibliography

[1] Lorraine Courneyea. Accounting for jet response induced MET backgrounds to new physics at the ATLAS experiment at CERNs LHC.

[2] Georges Aad et al. Observation of a new particle in the search for the Standard Model Higgs boson with the ATLAS detector at the LHC. *Phys.Lett.*, B716:1–29, 2012.

[3] Serguei Chatrchyan et al. Observation of a new boson at a mass of 125 GeV with the CMS experiment at the LHC. *Phys.Lett.*, B716:30–61, 2012.

[4] D. J. Griffiths. *Introduction to Elementary Particles*. John Wiley and Sons Inc., 2008.

[5] M. E. Peskin D.V. Schroeder. *An Introduction to Quantum Field Theory*. Westview Press, 1995.

[6] A.D. Martin, W.J. Stirling, R.S. Thorne, and G. Watt. Parton distributions for the LHC. *Eur.Phys.J.*, C63:189–285, 2009.

[7] Georges Aad et al. Measurement of the inclusive isolated prompt photon cross section in pp collisions at $\sqrt{s} = 7$ TeV with the ATLAS detector using 4.6 fb-1. 2013. arXiv hep-ex 1311.1440.

[8] G. Aad et al. Measurement of the inclusive isolated prompt photon cross section in pp collisions at $\sqrt{s} = 7$ TeV with the ATLAS detector. *Phys.Rev.*, D83:052005, 2011.

[9] S. Catani, M. Fontannaz, J.P. Guillet, and E. Pilon. Cross-section of isolated prompt photons in hadron hadron collisions. *JHEP*, 0205:028, 2002.

[10] The ATLAS Collaboration. Jet energy resolution in proton-proton collisions at $\sqrt{s} = 7$ tev recorded in 2010 with the atlas detector. *Eur. Phys. J. C*, 73(arXiv:1210.6210. CERN-PH-EP-2012-191):2306. 26 p, Oct 2012.

[11] G. Cowan. A survey of unfolding methods for particle physics. *Conf.Proc.*, C0203181:248–257, 2002.

[12] S.M. Riad. The deconvolution problem: An overview. *Proceedings of the IEEE*, 74(1):82–85, 1986.

[13] Georgios Choudalakis. Unfolding in atlas. Technical Report ATL-PHYS-PROC-2011-029, CERN, Geneva, Apr 2011.

[14] G. D'Agostini. A multidimensional unfolding method based on bayes' theorem. *Nuclear Instruments and Methods in Physics Research Section A: Accelerators, Spectrometers, Detectors and Associated Equipment*, 362(23):487 – 498, 1995.

[15] J. Beringer et al. Review of Particle Physics (RPP). *Phys.Rev.*, D86:010001, 2012.

[16] *ATLAS detector and physics performance: Technical Design Report, 1.* Technical Design Report ATLAS. CERN, Geneva, 1999. Electronic version not available.

[17] *ATLAS detector and physics performance: Technical Design Report, 2.* Technical Design Report ATLAS. CERN, Geneva, 1999. Electronic version not available.

[18] ATLAS inner detector: Technical design report. Vol. 1. 1997.

[19] G. Aad et al. The ATLAS Experiment at the CERN Large Hadron Collider. *JINST*, 3:S08003, 2008.

[20] M.S. Alam et al. ATLAS pixel detector: Technical design report. 1998.

[21] A. Abdesselam, T. Akimoto, P.P. Allport, J. Alonso, B. Anderson, et al. The barrel modules of the ATLAS semiconductor tracker. *Nucl.Instrum.Meth.*, A568:642–671, 2006.

[22] A. Abdesselam et al. The ATLAS semiconductor tracker end-cap module. *Nucl.Instrum.Meth.*, A575:353–389, 2007.

[23] E. Abat et al. The ATLAS Transition Radiation Tracker (TRT) proportional drift tube: Design and performance. *JINST*, 3:P02013, 2008.

[24] *ATLAS liquid-argon calorimeter: Technical Design Report*. Technical Design Report ATLAS. CERN, Geneva, 1996.

[25] *ATLAS tile calorimeter: Technical Design Report*. Technical Design Report ATLAS. CERN, Geneva, 1996.

[26] *ATLAS muon spectrometer: Technical Design Report*. Technical Design Report ATLAS. CERN, Geneva, 1997.

[27] A Polini. Performance and Operation of the ATLAS Resistive Plate Chambers Detector in 2011. Technical Report ATL-MUON-PROC-2012-003, CERN, Geneva, May 2012.

[28] D Adams, D Barberis, C P Bee, R Hawkings, S Jarp, R Jones, D Malon, L Poggioli, G Poulard, D Quarrie, and T Wenaus. The atlas computing model. Technical

Report ATL-SOFT-2004-007. ATL-COM-SOFT-2004-009. CERN-ATL-COM-SOFT-2004-009. CERN-LHCC-2004-037-G-085, CERN, Geneva, Dec 2004.

[29] Rene Brun and Fons Rademakers. ROOT - AN Object Oriented Data Analysis Framework. *Nucl. Inst. and Meth. in Phys. Res.*, A 389:81–86, 1996.

[30] Expected photon performance in the atlas experiment. Technical Report ATL-PHYS-PUB-2011-007, CERN, Geneva, Apr 2011.

[31] W Lampl, S Laplace, D Lelas, P Loch, H Ma, S Menke, S Rajagopalan, D Rousseau, S Snyder, and G Unal. Calorimeter clustering algorithms: Description and performance. Technical Report ATL-LARG-PUB-2008-002. ATL-COM-LARG-2008-003, CERN, Geneva, Apr 2008.

[32] Matteo Cacciari, Gavin P Salam, and Gregory Soyez. The anti-kt jet clustering algorithm. *Journal of High Energy Physics*, 2008(04):063, 2008.

[33] Performance of jet algorithms in the atlas experiment. Technical Report ATL-PHYS-INT-2010-129, CERN, Geneva, Dec 2010.

[34] Tim Adye. Unfolding algorithms and tests using RooUnfold. arXiv hep-ex 1105.1160.

[35] N. D. Gagunashvili. Comparison of weighted and unweighted histograms. *preprint*, 2006. arXiv physics.data-a 0605123.

[36] W. Press, S. Teukolsky, W. Vetterling, and B. Flannery. *Numerical Recipes in C*. Cambridge University Press, 1992.